Universität Hamburg

Universität Hamburg

Institut für physikalische Chemie

Dissertation

zur Erlangung des Grades

Doktor der Naturwissenschaften

(Dr. rer. nat.)

CdSe/CdS nanoparticles with controlled fluorescence lifetimes for multiplexing in biomedical applications

vorgelegt von

Sebastian Graf

Oktober 2023

Die vorliegende Arbeit wurde in der Zeit von Februar 2019 bis Oktober 2023 in der Arbeitsgruppe von Prof. Dr. Horst Weller am Institut für Physikalische Chemie der Universität Hamburg angefertigt.

Contents

Abbreviations

AIBN - azobis(isobutyronitrile)

BSA V - bovine serum albumin fraction V

CB - conduction band

DETA - diethylenetriamine

DBCO - dibenzocyclooctyne

DLS - dynamic light scattering

EDC - 1-ethyl-83-(3-dimethylaminopropyl)carbodiimide

EtOH - ethanol

EpCAM - epithelial cell adhesion molecule

FLIM - fluorescence lifetime imaging microscopy

FITC - fluorescein iso-thiocyanate

GS-QD - giant shell quantum dot

MWCO - molecular weight cutoff

NC - nanocrystal

NHS - n-hydroxysuccinimide

OA - oleic acid

OAm - oleylamine

ODE - octadecene

PB - polybutadiene

PB-b-PEG - polybutadiene - polyethylene glycole co-block polymer

PBS - phosphate buffered saline solution

PEG - polyethylene glycole

QD - quantum dot

QD@antibody - quantum dots coupled with antibodies

QD@EpCAM - quantum dots coupled to anti-EpCAM antibodies

QD@WGA - quantum dots coupled to wheat germ agglutinin

QY - quantum yield

R6G - rhodamine 6G

ROI - region of interest

RT - room temperature

SILAR - successive ion layer adsorption and reaction method

THF - tetrahydrofuran

TCSPC - time-correlated single photon counting

UV-Vis - ultraviolet-visible light spectroscopy

VB - valence band

WGA - wheat germ agglutinin

1 Abstract

The study of ever more challenging systems in bioimaging requires an increase of information content of the available measurement techniques. In case of fluorescence based techniques, e.g. confocal microscopy, this is limited by the amount of fluorophores that can be used simultaneously. In a state of the art experiment, based on spectral multiplexing, the amount of fluorophores is restricted by their spectral overlap, which usually leads to three to five maximum fluorophores. An elegant solution to overcome this limit, is achieved by exploiting fluorescence decay kinetics, in addition to fluorescence emission. CdSe/CdS core-shell quantum dots with big shells (GS-QD) have proven to be an useful model system for this approach, as the increase of shell size has only a negligible influence on the fluorescence emission spectrum, while the fluorescence lifetime changes dramatically with shell size. Thus, this system allows for the synthesis of various GS-QDs with similar emission colours, but strongly varied fluorescence lifetimes, which can be exploited using fluorescence lifetime imaging microscopy (FLIM). Furthermore, the GS-QDs could be stabilized in water and be made bio-compatible by the encapsulation within a polybutadiene-polyethylene glycol co-block polymer (PB-b-PEO). The size of the final encapsulated QD can be varied by changing the amount of polymer added during the encapsulation. Additionally, using polymer with functional end groups, chemical functionality can be introduced, allowing the conjugation of antibodies or other proteins to further modify the GS-QDs. This allows for the use of the QDs as e.g. cell stains. In this work, the use of such GS-QD as potential multiplexing agent in fluorescence microscopy was studied. Mixtures of these QDs were prepared and their fluorescence decay characteristics studied using two different models to extract the mixture composition from it. Both, linear fit of the mean lifetime, as well as the superposition model were studied, using simulated data and measurements of QD mixture samples. These models are prevalently used in literature, but no comparison between the models, regarding their respective precision and resolution has been made to date. It was found, that the superposition model is strictly superior in the analysis of two QD mixtures. Furthermore, three component mixtures were studied, where the use of the linear model is not possible anymore. Here, the superposition

model still showed promising results, though sample compositions were identified, where the use of the model yields erroneous results. To overcome these problems, two different approaches were applied. Firstly, post-synthetic modification of the used quantum dots (QDs) by ligand exchanges and secondly, the modification of the superposition model by introducing time gates. In the former case, a marked improvement of the fluorescence quantum yield (QY) of the QDs was observed, but no improvement of their fluorescence decay behaviour could be obtained. Nor did the modification of the model markedly improve the results for the problematic sample compositions. Additionally, the use of the GS-QDs as cell stains was investigated. Cell toxicity, unspecific cell uptake and staining of different cell components were studied. The QDs were markedly less toxic than a comparable concentration of free Cd salts, due to the encapsulation in the PB-b-PEG shell. Additionally, only a negligible amount of unspecific uptake was observed. A specific binding affinity for different cell organelles was imparted upon the QDs by conjugating antibodies or wheat germ agglutinin (WGA) respectively. Two different conjugation reactions, azide click chemistry and coupling by 1-ethyl-3-(3-dimethylaminopropyl)carbodiimide (EDC) and n-hydroxysuccinimide (NHS) were studied. Three different cell organelles were used as targets: the cell membrane, early endosomes and the cytoskeleton. For the cell membrane, two different binding strategies were applied. Firstly, the highly specific EpCAM receptor was targeted by introduction of a respective antibody and secondly, WGA was used as a relative unspecific binding motif. For the early endosomes and the cytoskeleton, a primary - secondary antibody approach was investigated, where the secondary antibodies were conjugated to the GS-QDs. While the latter approaches did not work, most likely since the created encapsulated GS-QDs were too big to diffuse into the inner cell compartments, the former approach yielded GS-QDs with a strong affinity to the cell membrane, regardless of the conjugation method or protein used. The use of the GS-QDs as fluorescence stains in ex vivo microscopy applications could therefore be successfully shown. By applying a superposition model for the analysis of a microscopy image, a multiplexing approach of hitherto unreached trinary complexity per fluorescence colour can be achieved. This work also showed a proof-of-principle approach on how to impart a desired specific cell affinity to the QDs. Thus, this work could show a solution on how to overcome present limits in spectral multiplexing as well as presenting a suitable particle system to use in such a capacity.

2 Zusammenfassung

Die Untersuchung von immer anspruchsvolleren Systemen in der biologischen Bildgebung erfordert eine Steigerung des Informationsgehalts der verfügbaren Messverfahren. Im Falle fluoreszenzbasierter Techniken, z. B. der konfokalen Mikroskopie, ist dieser durch die Anzahl der gleichzeitig verwendbaren Fluorophore begrenzt. Diese Anzahl ist durch den spektralen Überlapp der Fluorophore begrenzt. Die führt in der Regel zu maximal drei bis fünf Fluorophoren pro Experiment. Eine elegante Lösung zur Überwindung dieser Beschränkung ist die Ausnutzung der Fluoreszenzskinetik zusätzlich zur Fluoreszenzemission. CdSe/CdS-Kern-Schale-Quantenpunkte mit großen Schalen (GS-QD) haben sich als nützliches Modellsystem für diesen Ansatz erwiesen, da die Zunahme der Schalengröße nur einen vernachlässigbaren Einfluss auf das Fluoreszenzemissionsspektrum hat, während sich die Fluoreszenzlebensdauer mit der Schalengröße drastisch ändert. Somit ermöglicht dieses System die Synthese verschiedener GS-QDs mit ähnlichen Emissionsfarben, aber stark variierenden Fluoreszenzlebensdauern, die mit Hilfe der Fluoreszenzlebensdauer-Imaging-Mikroskopie (FLIM) ausgewertet werden können. Darüber hinaus konnten die GS-QDs in Wasser stabilisiert und durch die Verkapselung in einem Polybutadien-Polyethylenglykol-Co-Blockpolymer (PB-b-PEO) biokompatibel gemacht werden. Die Größe der endgültigen eingekapselten QD kann durch Änderung der Menge des während der Verkapselung zugesetzten Polymers variiert werden. Durch die Verwendung von Polymeren mit funktionellen Endgruppen können außerdem die Konjugation von Antikörpern oder anderen Proteinen zur weiteren Modifizierung der GS-QDs realisiert werden. Dies ermöglicht die Verwendung der QDs z. B. als Zellfärbemittel. In dieser Arbeit wurde die Verwendung solcher GS-QD als potenzielles Multiplexing-System in der Fluoreszenzmikroskopie untersucht. Es wurden Mischungen dieser QDs hergestellt und ihre Fluoreszenzabklingcharakteristiken untersucht, wobei zwei verschiedene Modelle verwendet wurden, um daraus die Zusammensetzung der Mischung zu extrahieren. Sowohl die Auswertung des Modells der mittleren Lebensdauer, welche linear vom Mischungsanteil abhängt, als auch das Superpositionsmodell wurden anhand von simulierten Daten und Messungen von QD-Mischproben untersucht. Diese Modelle wer-

den in der Literatur häufig verwendet, doch wurde bisher kein Vergleich zwischen den Modellen hinsichtlich ihrer jeweiligen Präzision und Auflösung vorgenommen. Es wurde festgestellt, dass das Superpositionsmodell bei der Analyse von zwei QD-Mischungen eindeutig überlegen ist. Darüber hinaus wurden Drei-Komponenten-Mischungen untersucht, bei denen die Verwendung des linearen Modells nicht mehr möglich ist. Hier zeigte das Superpositionsmodell immer noch vielversprechende Ergebnisse, obwohl Probenzusammensetzungen identifiziert wurden, bei denen die Anwendung des Modells zu fehlerhaften Ergebnissen führt. Um diese Probleme zu überwinden, wurden zwei verschiedene Ansätze angewandt. Erstens die postsynthetische Modifizierung der verwendeten Quantenpunkte (QDs) durch Ligandenaustausch und zweitens die Modifizierung des Superpositionsmodells durch Einführung von Zeitfenstern. Im ersten Fall wurde eine deutliche Verbesserung der Fluoreszenz-Quantenausbeute (QY) der QDs beobachtet, jedoch konnte keine Verbesserung der Fluoreszenzkinetik erzielt werden. Auch die Modifikation des Modells führte nicht zu einer deutlichen Verbesserung der Ergebnisse für die problematischen Probenzusammensetzungen. Zusätzlich wurde die Verwendung der GS-QDs als Zellfärbemittel untersucht. Dabei wurden die Zelltoxizität, die unspezifische Zellaufnahme und die Anfärbung verschiedener Zellbestandteile untersucht. Die QDs waren deutlich weniger toxisch als eine vergleichbare Konzentration freier Cd-Salze, was auf die Verkapselung in der PB-b-PEG-Hülle zurückzuführen ist. Außerdem wurde nur eine vernachlässigbare Menge an unspezifischer Aufnahme beobachtet. Eine spezifische Bindungsaffinität für verschiedene Zellorganellen wurde den QDs durch Konjugation von Antikörpern bzw. Weizenkeimagglutinin (WGA) verliehen. Zwei verschiedene Konjugationsreaktionen, die Azid-Click-Chemie und die Kopplung mit 1-Ethyl-3-(3-dimethylaminopropyl)carbodiimid (EDC) und n-Hydroxysuccinimid (NHS) wurden untersucht. Drei verschiedene Zellorganellen wurden als Ziele verwendet: die Zellmembran, frühe Endosomen und das Zytoskelett. Für die Zellmembran wurden zwei verschiedene Bindungsstrategien angewandt. Zum einen wurde der hochspezifische EpCAM-Rezeptor durch Einführung eines entsprechenden Antikörpers ins Visier genommen, zum anderen wurde WGA als relativ unspezifisches Bindungsmotiv verwendet. Für die frühen Endosomen und das Zytoskelett wurde ein primär-sekundärer Antikörperansatz untersucht, bei dem die sekundären Antikörper mit den GS-QDs konjugiert wurden. Die letztgenannten Ansätze nicht funktionierten, wahrscheinlich weil die erzeugten verkapselten GS-QDs zu groß waren, um in die inneren Zellkompartimente zu diffundieren. Dahingegen führte der erste Ansatz zu GS-QDs mit einer starken Affinität zur Zellmembran, unabhängig von der Kon-

jugationsmethode oder dem verwendeten Protein und ermöglicht so die Nutzung der GS-QDs als Zellfärbemittel. Die Verwendung der GS-QDs als Fluoreszenzfarbstoffe in Ex-vivo-Mikroskopieanwendungen konnte daher erfolgreich gezeigt werden. Durch die Anwendung eines Superpositionsmodells für die Analyse eines Mikroskopiebildes konnte ein Fluoreszenzlebensdauermultiplexing-Ansatz von bisher unerreichter trinärer Komplexität pro Fluoreszenzfarbe erreicht werden. Diese Arbeit zeigte auch einen Proof-of-Principle-Ansatz, wie den QDs eine gewünschte spezifische Zellaffinität verliehen werden kann und sie somit als Zellfärbemittel genutzt werden können. Somit konnte diese Arbeit eine Lösung zur Überwindung der derzeitigen Grenzen beim spektralen Multiplexing aufzeigen und ein geeignetes Partikelsystem für eine solche Funktion präsentieren.

3 Theory

3.1 Synthesis of quantum dots

The synthesis of quantum dots (QDs), and most nanocrystals (NCs) in chemistry, is done via a bottom-up approach, from the atom towards nanocrystals. The synthesis is based on three typical components. Firstly, precursors, the source of the atoms for the nucleation and growth of the nanoparticles. Secondly, ligands, which stabilize the NCs in solution, saturate dangling bonds on the NC surface and play a critical role in shape and size control. Thirdly, the solvent.[1, 2, 3] The interplay of these three components, in addition to general reaction parameters like temperature and time, determine the size and shape of the final NCs.

To ensure a good homogeneity of size, it is important to take note of the LaMer model, which describes the nucleation and growth of NCs. The nucleation and growth mechanism can be separated into three phases,[4, 5, 6] schematically shown in Figure 3.1. In the first phase, the concentration of the monomers, the building blocks of the NCs, increases, e.g. by thermal decomposition of the precursor or by chemical reaction. After a critical nucleation concentration has been reached, the second phase, the nucleation phase, begins. Herein the monomers are rapidly consumed by nucleation. This will reduce the monomer concentration below the nucleation concentration, which marks the start of the final phase, the growth phase. The available nuclei grow by consuming monomer, but no new nuclei can form. The growth on the already formed nuclei is energetically favored over formation of new nuclei, due to the high energy cost involved with creating the nucleus surface. This can be expressed using the Gibbs free energy, as seen in Equation 3.1.

$$\Delta G = -\frac{4}{3}\pi r^3 |\Delta G_V| + 4\pi r^2 \gamma \tag{3.1}$$

where r is the radius of the nucleus, $|\Delta G_V|$ is the difference in Gibbs free energy per unit volume of the new nucleus compared to the smaller size and γ is the surface energy per unit area. The first term describes the energy gain by the bond formation inside the nucleus. The second term describes the unfavorable energy
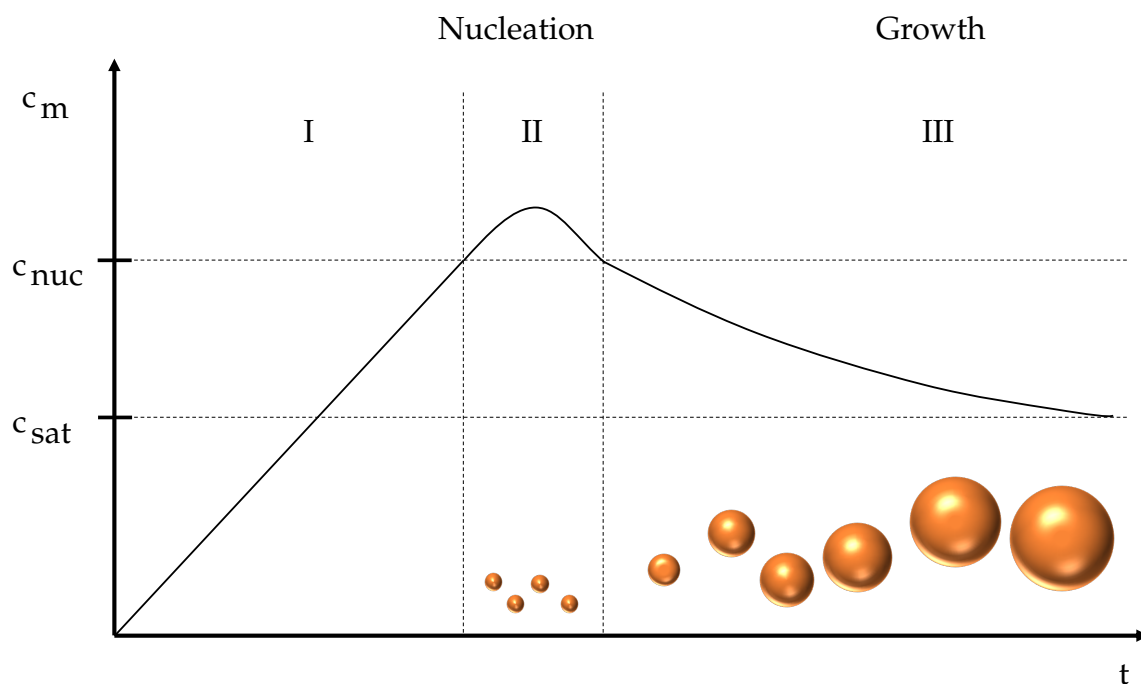
Figure 3.1: A scheme of the nucleation and growth of NCs after LaMer. Three distinct phases can be observed. During the first phase the monomer concentration, c_m increases steadily, e.g. due to thermal decomposition. After reaching the nucleation concentration, c_{nuc}, the monomer is rapidly consumed to form the first stable nuclei. After the monomer concentration falls again below the nucleation concentration, no new nuclei are formed, but already existing nuclei can grow further until the saturation concentration, c_{sat}, is reached.

increase by the formation of the surface. The nucleation is therefore governed by these two competing energies, the volume energy and the surface energy.

A graphical representation of Equation 3.1 can be seen in Figure 3.2. The critical radius, r_c, can be seen as the radius at the maximum of the curve, describing the minimal size for a nucleus to be stable. Beginning with this size, growth of the nucleus is favored over dissolution.[7]
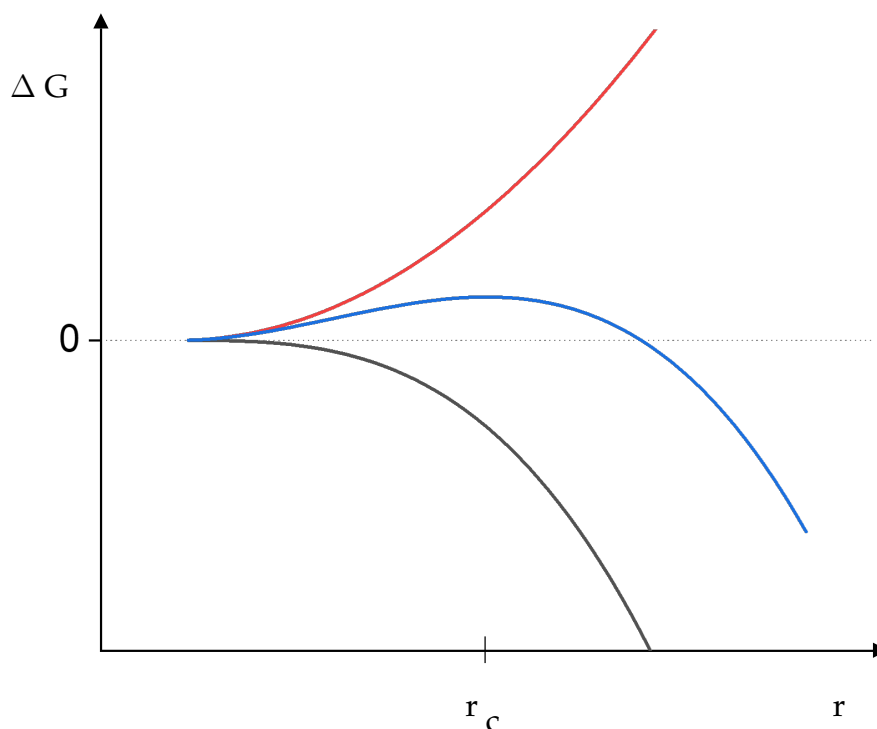

Figure 3.2: Scheme of the free Gibbs free energy of nucleation and growth as predicted by the LaMer model. In red the surface energy is depicted, in black the volume energy and in blue the combined curve can be seen. The critical radius for the nuclei can be derived from the maximum of that curve.

The LaMer model yields the clues needed for a monodisperse size distribution of a synthesized NC batch. The nucleation phase needs to be short, so that all nuclei are formed at the same time. These can then grow at a homogeneous rate. Thus, a long formation step of nuclei is avoided, where the oldest nuclei have had a long time to grow compared to the youngest formed nuclei. This so called "burst nucleation" is the idea behind synthesis methods like the "hot injection".[8, 9] The seeded growth method, used for the formation of core-shell materials like CdSe/CdS QDs, exploits these findings as well. Fully formed NCs

of CdSe are provided as "nuclei" and the CdS monomer concentration is kept below the critical nucleation concentration to avoid homogeneous nucleation. Only the heterogeneous growth of the CdS shell therefore remains possible. It is important to keep the reaction conditions mild, otherwise the formation of a composite material, instead of a separated core and shell, might be possible.[10, 11] A separation of the two materials, e.g. due to immiscibility, can lead to one side of the NC being of a different composition than the other, the formation of so called "Janus-like" NCs.[12, 13] A scheme of different possible particle compositions is shown in Figure 3.3.

Janus-like   **Core-Shell**   **Composite**
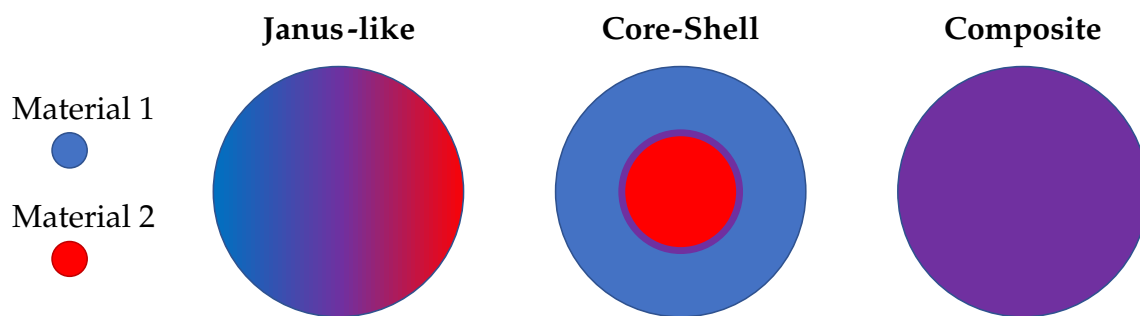
Material 1

Material 2

Figure 3.3: A scheme of different possible NC compositions. Depending on temperature, miscibility of the used materials, ligands and other factors it is possible to finely control and change the composition of synthesized NCs. Core-shell materials are usually obtained in a two-step process, the synthesis of the cores and a following shelling step.

3.2 Ligands

Ligands perform a crucial role for NCs in suspension. They are chiefly responsible for the solubility of the NCs, stabilize them against aggregation via steric or electronic repulsion and saturate dangling bonds and trap states on the surface of the NCs.[3, 14, 15] If chosen wisely, they can also be used to influence shape of the NCs during synthesis, e.g. by saturating specific facettes of the crystals, allowing for growth only on the unsaturated facettes. Thus, anisotropic shapes can be synthesized.[16, 17] Ligands can be broadly characterized using their bonding behaviour to the NC in three classes: X-, L- and Z-type ligands. Z-type ligands bind as Lewis acids, by accepting two electrons from a surface anion. L-type ligands bind as Lewis bases, by donating two electron to a surface cation. X-type ligands are forming covalent bonds with the surface atoms.[18, 19] A scheme of their bonding behaviour can be seen in Figure 3.4.

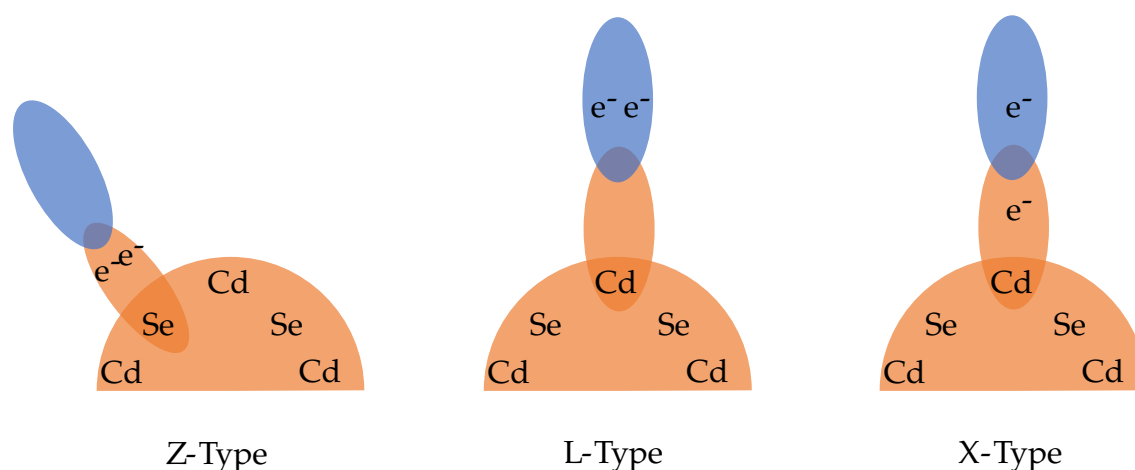Most isotropic synthesis methods for NCs only employ a single ligand. This

Figure 3.4: Scheme of the different ligand types. The Z-type and L-type ligands bind as neutral Lewis acids and bases respectively. For the X-type ligands a covalent bond is formed. For QDs , anionic ligands, such as Cl^- are often considered X-type.

can lead to undersaturated surfaces, since each ligand has prefered binding sites, depending on the crystal structure of the NC surface and its bonding behaviour.[20, 2, 21] Consequently, gaps in the ligand coverage can be assumed for most single ligands, as no ligand will saturate all NC crystal facettes equally well. A mixture of ligands, usually of different types, can therefore be employed to improve the surface saturation of NCs, which can improve properties, e.g. quantum yield or reduce blinking behaviour.[22, 23, 24] The QDs used in this work are not initially stable in aqueous solution due to their native ligands, oleic acid, used in the synthesis. Additionally, due to the cadmium, they are toxic to most cells.[25, 26, 27] Two problems which needed to be overcome to use these particles in biomedical applications. One elegant solution to both of these problems is to exchange the native ligands with a polymer ligand shell, based on polyethyleneglycole (PEG). It imparts water solubility while also preventing Cd from leaching out from the QDs. Additionally, the PEG shell exhibits a "stealth" effect, preventing the unspecific aggregation of proteins on the QD surface. This strongly reduces the formation of a protein corona, which is known to drastically increase unspecific cell uptake.[28, 29] Hence, the as-prepared particles are expected to only show a significant uptake or significant adhesion to targets, if a binding motif is incorporated into the ligand shell, which is an important property of any cell stain. A scheme of how such a ligand exchange and phase transfer can be done is shown in Figure 3.5. In an optional first step, the native ligand is exchanged by a hydrophobic polymer with a suitable anchor group, e.g. polybutadiene with a terminal diethylenetriamin group (PB-DETA). The addition of this polymer will in-

crease the density of the final ligand shell. The NCs are then transferred into a amphilic solvent and a PB-b-PEG co-block polymer is added. The PB blocks of the blockpolymer will intercalate with the PB-DETA due to hydrophobic interactions. Even without those, the NCs with their native ligands will prefer the hydrophobic environment of the micelles formed by the blockpolymer. Addition of a radical initiator will then result in a emulsion polymerisation within each micelle by crosslinking the alkene groups present in the PB. Through addition of styrene and divinylbenzol (DVB) a further increase in the thickness and stability of the inner hydrophobic shell can be achieved. The outer PEG shell confers all the advantages known from that polymer for e.g. biological applications.[30, 31, 32]
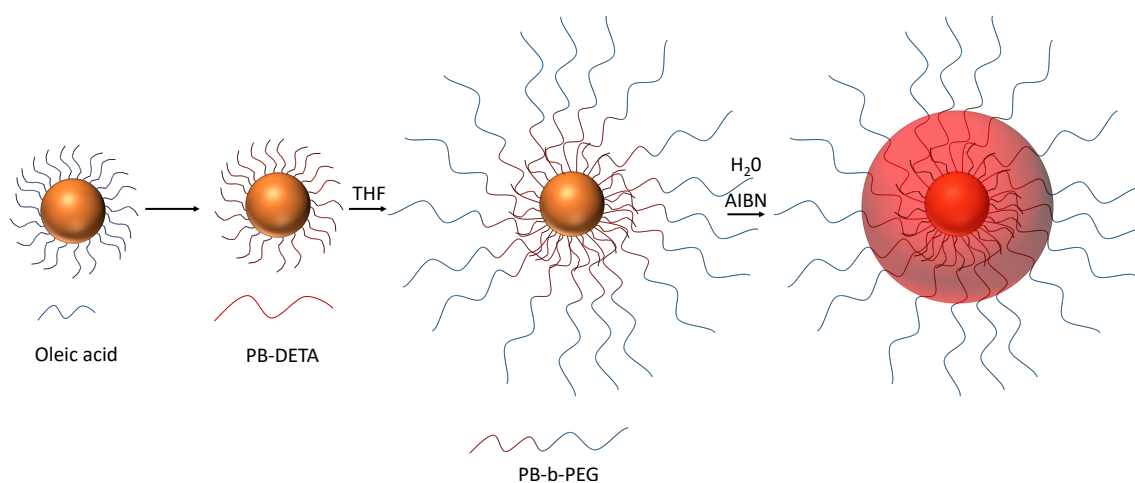

Figure 3.5: A scheme of the phase transfer to water and polymer encapsulation of NCs. The native ligand of the NCs, usually oleic acid in case of QDs, is exchanged by a small PB ligand. This can intercalate with the PB-b-PEO added in the next step, while the QDs are transfered to an amphilic solvent, such as tetrahydrofuran (THF). The such prepared NCs can then be transfered to water while the PB blocks are crosslinked through radical emulsion polymerisation initiated by a radical initiator, such as azobis(isobutyronitrile) (AIBN).

3.3 Properties of QDs

3.3.1 Bandstructure

The electronic bandstructure of semiconductor QDs can be described using a linear combination of atomic orbitals (LCAO) approach. In this bottom up description, when going from single atom to nanocrystal, the addition of atoms leads to formation of molecular orbitals in a linear combination. For each molecular orbital, a low energy binding orbital and a high energy anti-binding orbital are

formed. With increasing number of atoms, the energy states of these orbitals become closer and closer until a quasi continuous state density is reached. The binding orbitals form the fully filled valence band, while the empty anti-binding orbitals form the conduction band, with distinct energy gap between these two bands. A schematic description is shown in Figure 3.6.[33]
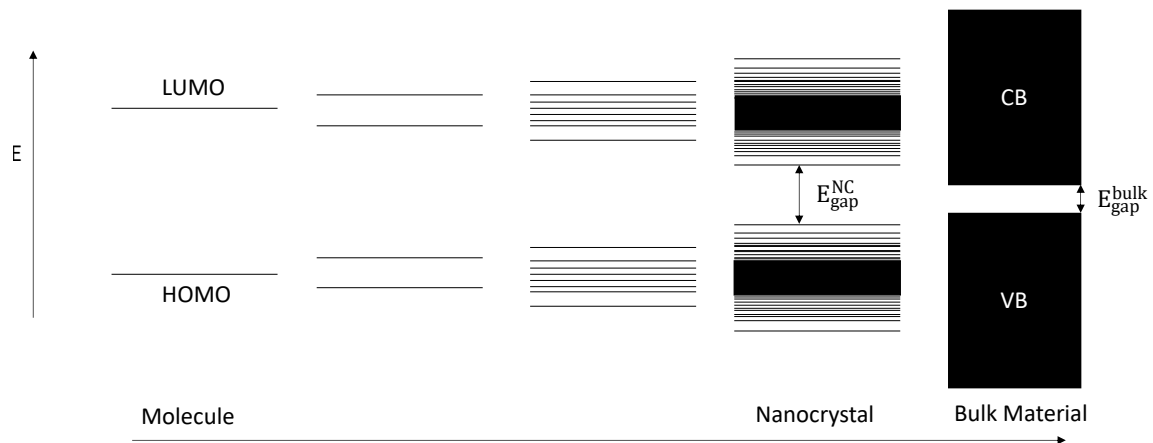

Figure 3.6: A scheme of the energetic bandstructure for semiconductors, from molecule over nanocrystal to bulk material. As the number of atoms increases, the number of states increases until a quasi-continuous band of states is formed. A distinct gap between the states of the lowest unoccupied molecule orbital (LUMO) and the highest occupied molecule orbital (HOMO) will always be maintained. When the states have formed a continuous band the unoccupied states are called the conduction band, whereas the occupied states are named valence band. The bandgap energy of nanocrystals is bigger than for the bulk material but slowly approaches bulk values with increasing size of the NC.

3.3.2 Type I - Type II band structures

The growth of a shell material around a QD core can have many different advantages, e.g. increase of quantum yield, reduction of trap sites, reduced blinking and more.[10, 34, 23] This introduction of at least one more element into the QD also changes the band structure of the system. This can lead to a straddled band-structure, type I, or a staggered band structure, type II. In the former, electron and holes formed during excitation of the material are located in the core of the material, leading to high recombination rates and therefore typically high QYs of these types of QDs. In the latter case, the electron is located mostly in the shell of the material, whereas the hole is again confined to the core. This separation of the charge carriers leads to typically lower QY but can boost performance in

catalysis or photovoltaic applications.[35, 36, 37] In the case of only a slight or even no setoff of one of the bands, typically the conduction band, a quasi-type II structure is created, where the holes are located in the core, but the electrons are delocalized over the whole material. A scheme of the bandstructures can be seen in Figure 3.7
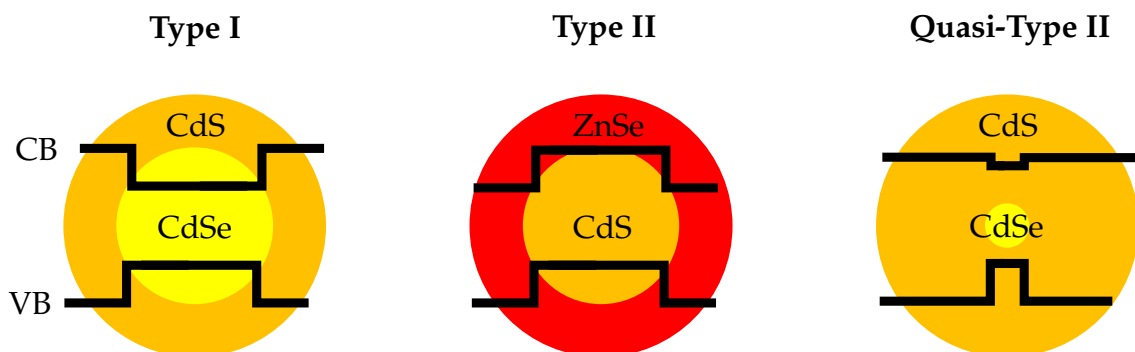

Figure 3.7: A scheme of the different electronic bandstructures of core-shell NCs. In a type I structure the electron and holes are both localized in the same material, usually in the core, leading to high recombination efficiencies. In type II structures, the electron and holes are separated due to the staggered bandstructure. In a quasi-type II structure, the offset of one of the bands, usually the conduction band, is negligible. This leads to a localization of the holes in one material, while the electrons are delocalized over the whole NC.

3.4 Fluorescence

Fluorescence is the emission of light by a material after excitation by light. In this process, a photon excites an electron from the ground state of the valence band into the conduction band (CB). An electron-hole pair, an exciton, is formed thereby. After non-emissive relaxation back to the ground state of the conduction band, a photon is emitted as the electron returns to the valence band (VB). The energy loss due to non-emissive relaxation processes leads to a red-shift of the fluorescence photon compared to the initial excitation photon and is called Stokes' shift.[38] A scheme of this process can be seen in Figure 3.8. Typical radii of excitons are in the range of a few nanometer. Therefore, in nanocrystals of smaller size than the exciton, the exciton is strongly confined. This leads to an additional energy barrier, the confinement energy, which leads to an increase of the band energy and therefore a blue-shift of fluorescence colour. Even when the size of the nanocrystal is bigger than the exciton radius, a weak confinement can be observed leading to a smaller blue shift. The exciton is unconstrained only in a

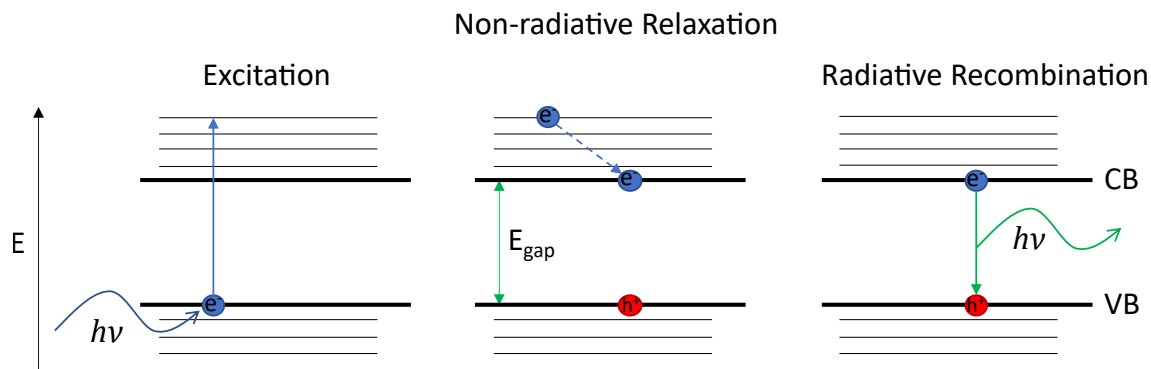crystal several times larger than the exciton radius. Then, the bulk material band gap is exhibited.[39]

Figure 3.8: A scheme of the fluorescence process. It can be divided into three steps: the excitation of an electron by a photon and the formation of an exciton, the non-radiative relaxation to the ground state of the CB, and the radiative recombination. Due to the energy loss during the non-radiative relaxation a red-shift of the emitted light can be observed.

A notable characterization of this process is done using the quantum yield (QY), seen in Equation 3.2, which describes the efficiency of the fluorescence process and is defined as the number of emitted photons over the number of adsorbed photons. As such its values range from 1, every excitation photon leads to a fluorescence photon, to 0, a non-fluorescent material.[40]

$$QY = \frac{n_{em}}{n_{abs}} \tag{3.2}$$

where n_{em} is the number of emitted photons and n_{abs} is the number of absorbed photons. For small concentrations of fluorophores their fluorescence intensity scales linearly. The proportionality constant is given by their QY and the amount of absorbed light, as shown in 3.3.

$$I_F = k\,c = QY\,I_{abs} \tag{3.3}$$

where I_F is the fluorescence intensity, k a proportionality constant, c the concentration of the fluorophore, QY the quantum yield and I_{abs} the amount of absorbed light. Generally, fluorophore concentrations with absorbances ≤ 0.05 show a linear relationship between fluorophore concentration and fluorescence intensity. For higher concentrations, effects like re-absorption of emitted photons by the fluorophore and scattering lead to a non-linear behaviour.[40] By applying Lambert-Beer's law[40] to describe the amount of absorbed light, as shown in Equation 3.4, the Equation 3.5 results from Equation 3.3.

$$A = \epsilon\,c\,d = -log(\frac{I_0}{I_{trans}}) \rightarrow I_{abs} = I_0 - I_{trans} = I_0 \cdot (1 - 10^{-A}) \tag{3.4}$$

where A is the absorbance, ϵ the extiction coefficient, c the concentration of the analyte, d the length of the lightpath through the analyte, I_0 the intensity of incoming light, I_{abs} the intensity of absorbed light and I_{trans} the intensity of transmitted light.

$$I_F = QY \cdot I_0 \cdot (1 - 10^{-\epsilon\,c\,d}) \tag{3.5}$$

Equation 3.5 can then be simplified by a first order Taylor approximation of the last term to result in Equation 3.6 (only for small values of $\epsilon\,c\,d$.

$$I_F = QY \cdot I_0 \cdot 2.3\,\epsilon\,c\,d = QY \cdot k \cdot c;\; k = 2.3 \cdot \epsilon \cdot d \cdot I_0 \tag{3.6}$$

where k is a proportionality constant given by the measurement setup and the extinction coefficient of the QDs.

3.5 Fluorescence lifetime

Emission of a photon by an excited fluorescent state is a spontaneous process, similar to radioactive decay. As such, no predictions for the decay time of a single fluorophore can be made, but a statistical description of the fluorescence decay by way of an exponential decay can be made. The fluorescence lifetime τ obtained by this description, as shown in Equation 3.7, is similar to the radioactive half-life time. It is the time needed for the fluorescence to decay by the factor of $\frac{1}{e}$.

$$I(t) = I_0\,e^{\frac{-t}{\tau}} \tag{3.7}$$

where I(t) is the fluorescence intensity at time t, I_0 is the initial fluorescence intensity and τ is the fluorescence lifetime. The fluorescence lifetime can also be described as the inverse of the fluorescence decay rate k and as such is sensitive to the radiative (rad) and non-radiative (non-rad) relaxation pathways, as shown in Equation 3.8 and described in greater detail later.

$$\tau = \frac{1}{k} = \frac{1}{k_{rad} + k_{non-rad}} \tag{3.8}$$

In case of fluorescent molecules, the fluorescence decay can usually be described by a mono-exponential behaviour. For QDs, oftentimes a bi- or triexponential decay can be observed, due to e.g. trap states at the QD surface or other

processes competing with the radiative relaxation, as can be seen in Figure 3.9 (a) and (b) respectively.[41, 42, 43] This leads to Equation 3.9 as a more general way to describe the fluorescence decay curve.
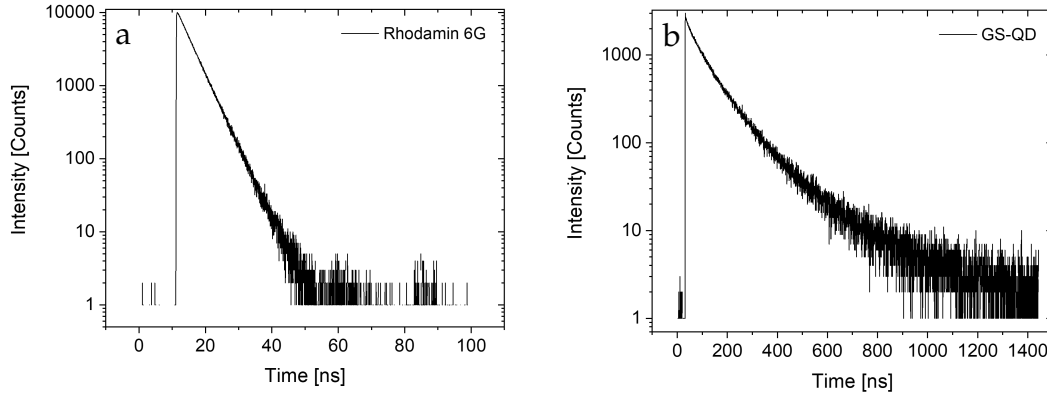

Figure 3.9: Fluorescence decays of Rhodamin6G (a) and GS-QD (b). A mono-exponential decay can be observed for the rhodamine 6G (R6G), whereas the QDs exhibit a multi-exponential decay behaviour. The QD decay agrees very well with a bi-exponential decay.

$$I(t) = A_1 \, e^{\frac{-t}{\tau_1}} + A_2 \, e^{\frac{-t}{\tau_2}} \left(+A_3 \, e^{\frac{-t}{\tau_2}} + \cdots \right) \tag{3.9}$$

where A_1, A_2 and so on are the respective amplitudes of the respective decay pathways and τ_1, τ_2, etc... the respective lifetimes.

For the description of such multi-exponential curves, the mean lifetime has found use. It can be defined using amplitude or intensity weighting, as described below.[38, 43]

$$\tau_{Amp} = \frac{\sum A_i \tau_i}{\sum A_i} \tag{3.10}$$

$$\tau_{Int} = \frac{\sum A_i \tau_i^2}{\sum A_i \tau_i} \tag{3.11}$$

In this work, the intensity weighted mean lifetime is used, unless denoted otherwise. The total intensity of a fluorescence decay can be described as the integral of Equation 3.9 and leads to the following equation.

$$I = \int_0^\infty A_1 \, e^{\frac{-t}{\tau_1}} + A_2 \, e^{\frac{-t}{\tau_2}} + \cdots dt = A_1 \, \tau_1 + A_2 \, \tau_2 + \cdots = \tau_{Amp} \cdot \sum A_i \tag{3.12}$$

3.5.1 Fluorescence quenching

When the fluorescence intensity of a fluorophore is reduced by addition of another chemical, this chemical is called quencher. Interactions between this quencher and the fluorophore lead to non-radiative relaxation of the excited state, resulting in the observed loss of fluorescence. These interactions can be separated in to two groups, dynamic and static.

In case of static quenching, these interactions persist for far longer than the excited state and the formed quencher-fluorophore complex is non-fluorescent. Therefore, fluorescence intensity decreases, but no change of fluorescence lifetime can be observed with static quenching.[40] The fluorescence can then be described using the Stern-Vollmer equation, seen in Equation 3.13.

$$1 + K_S[Q] = \frac{F_0}{F} \tag{3.13}$$

where F_0 is the fluorescence intensity without quencher, F the fluorescence intensity with quencher, K_S is the rate constant of the quenching and $[Q]$ the quencher concentration.

In the case of dynamic quenching, the interactions proceed within the timeframe of the fluorescence lifetime. Usually, these constitute a charge transport from the excited fluorophore state to the quencher. A quenching only occurs if an excited fluorophore interacts with a quencher molecule. This leads to a decrease of fluorescence intensity, similiar to static quenching, but additionally an impact on the fluorescence lifetime can be observed. The Stern-Vollmer equation is expanded to the form shown in Equation 3.14 and the fluorescence lifetime changes as seen in Equation 3.15 due to the addition of an additional relaxation term by the quencher interaction. The fluorescence lifetime therefore is always reduced by dynamic quenching.[40]

$$1 + K_Q\tau_0[Q] = \frac{F_0}{F} \tag{3.14}$$

where F_0 is the fluorescence intensity without quencher, F the fluorescence intensity with quencher, K_Q is the rate constant of the quenching, τ_0 is the fluorescence lifetime of the unquenched system and $[Q]$ the quencher concentration.

$$\tau_0 = \frac{1}{k_{rad} + k_{non-rad}} \rightarrow \tau = \frac{1}{k_{rad} + k_{non-rad} + k_Q[Q]} \tag{3.15}$$

where k_{rad} and $k_{non-rad}$ are the rate constants of radiative and non-radiative relaxation respectively.

The effects of quenching can be visualized using the Stern-Vollmer plot, ex-

emplary shown in Figure 3.10. The inverse relative fluorescence intensity and inverse relative lifetime in presence of the quencher are plotted against the quencher concentration. In case of static quenching, the inverse relative fluorescence intensity will increase, while the fluorescence lifetime is unchanged. Whereas for dynamic quenching the change in fluorescence intensity is matched by a similar change in fluorescence lifetime.
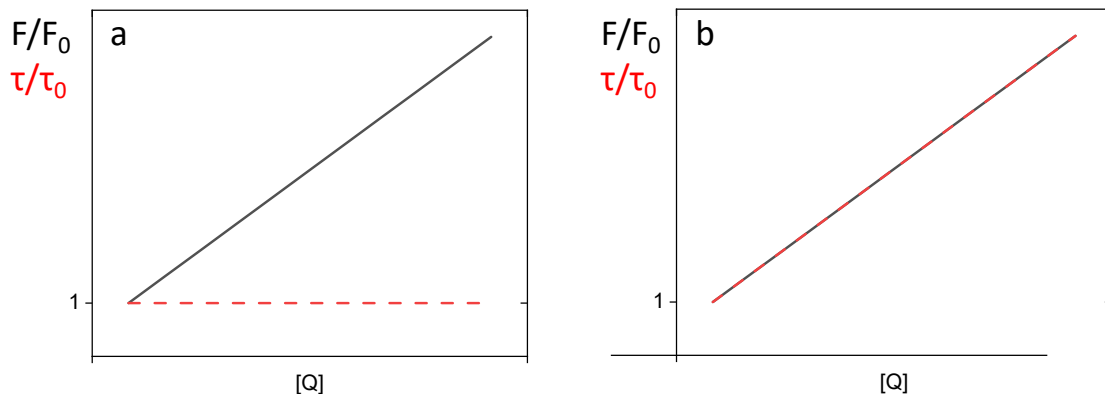

Figure 3.10: Stern-Vollmer plot of static quenching (a) and dynamic quenching (b). In the first case, only the fluorescence intensity is changed, the fluorescence lifetime stays constant. In the latter case both, the fluorescence intensity and lifetime have changed.

3.6 Multiplexing in biomedical applications

Multiplexing is defined as the simultaneous detection of multiple analytes or multiple detection parameters per analyte. It is a technique used to adress problems or questions, where a single analyte or paramter doesn't provide enough information. Such problems might be interaction of proteins or biomolecules in a cell, detection of specific cells within a mixture of different cells or detection of toxins in complex chemical environments.[44, 45, 46] One of the simplest imaginable multiplexing experiment is the use of multiple fluorescent stains with different emission colours, where distinction of the analytes is done via the different emission spectra. Depending on the sophistication of the experimental setup and question, the relevant multiplex signal might be a simple mixture of colour. For example, a red and green analyte creating a yellow pixel in mixture. Thereby it might be possible to distinguish between cancerous cells and normal cells in a complex tissue, if the cancer cells express two specific types of receptors on their cell membrane, whereas healthy cells express only one. A deeper analysis of the

emission spectrum of each pixel and comparison to the base emission spectra of the analytes can be done, as well, as shown in Figure 3.11.[47] The latter could yield a precise quantification of the mixture composition instead of qualitative assessment of mixture.
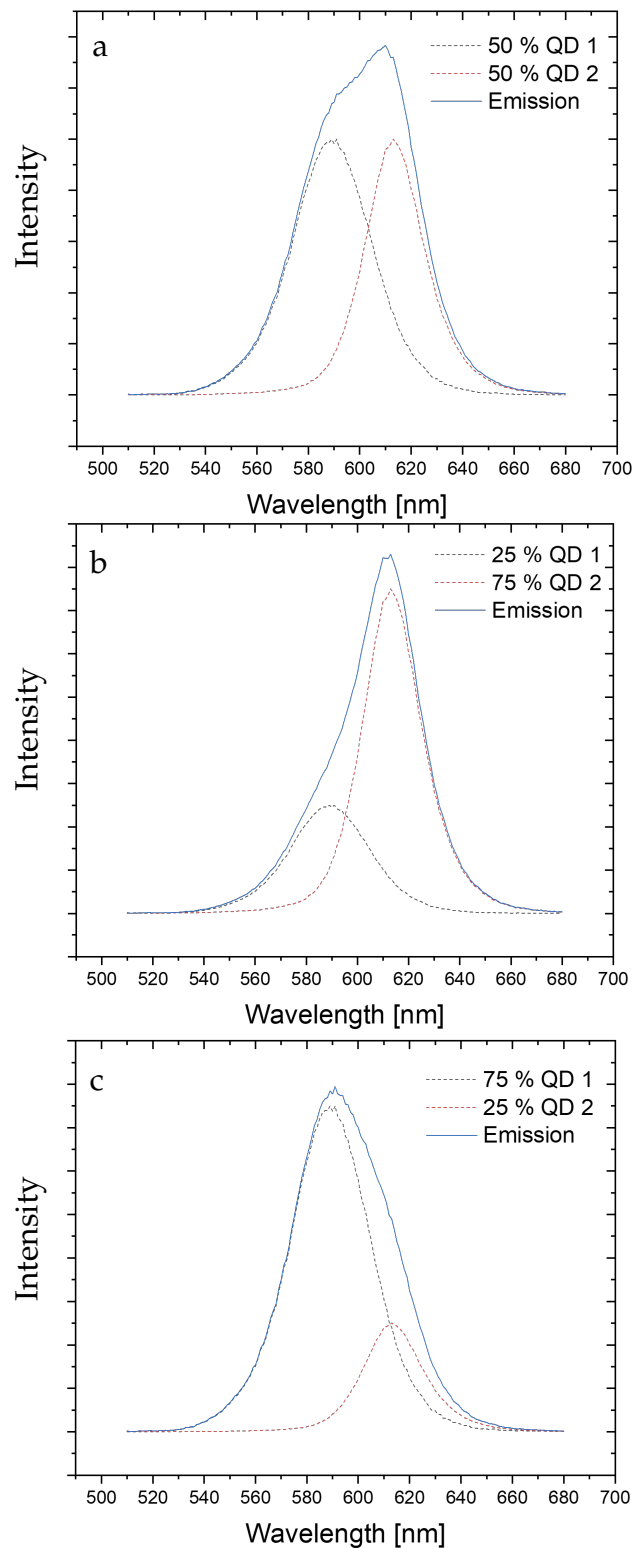
Figure 3.11: Scheme of reconstruction of the mixture composition by applying a superposition of the base curves (dotted black and red line respectively) to the emission of the mixture (blue line).

Using fluorescence emission alone for multiplexing is limited by several factors, such as the noise induced by the measurement setup or background caused by e.g. autofluorescence of cells and tissues. Especially the latter is a problem for using fluorophores with only slightly different emission maxima, since even small amounts of background signal can complicate the calculation of the mixture composition immensely.[48, 49, 50] Using fluorescence lifetime for multiplexing has the big advantage, that nearly all organic fluorophores and proteins have fast fluorescence lifetimes in the range of 1 - 5 ns,[41, 51], much shorter than most QDs, also seen in Figures 3.9 and 3.12. This allows for an easy separation of background and signal.
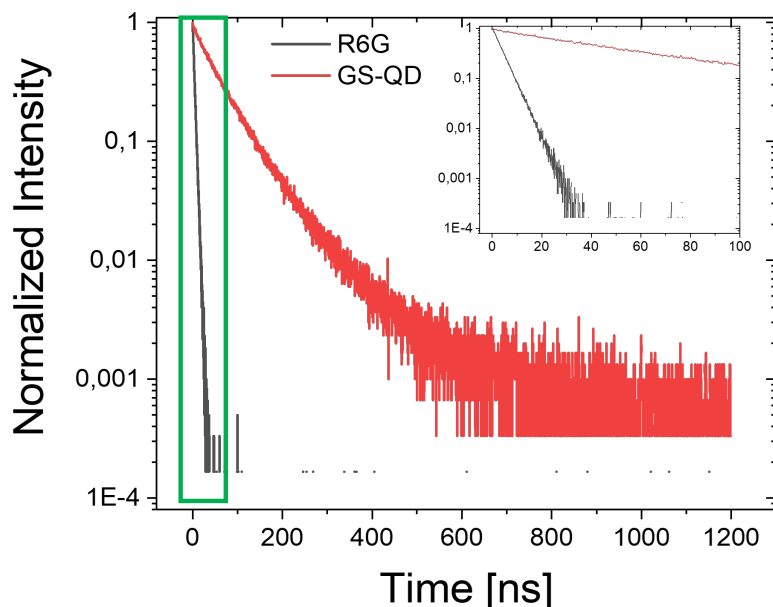
Figure 3.12: Fluorescence decay curves of R6G and GS-QD. The inset is a zoom on the region marked by the green rectangle. Clearly, the fluorescence lifetime of the R6G is much smaller, $\approx$ one and a half orders of magnitude, than of the GS-QD.

Two main approaches are usually applied for fluorescence lifetime multiplexing:

Firstly, the mean fluorescence lifetime is evaluated. It is linear dependent on the mixture fraction of the fluorophores[52] as shown in Figure 3.13.

It can simply be determined using an arbitary complex (usually three or more) exponential decay to fit the mixed fluorescence decay curve. The mean lifetime can then be calculated using Equation 3.10 or 3.11. The mixture fractions can be calculated using Equation 3.16.
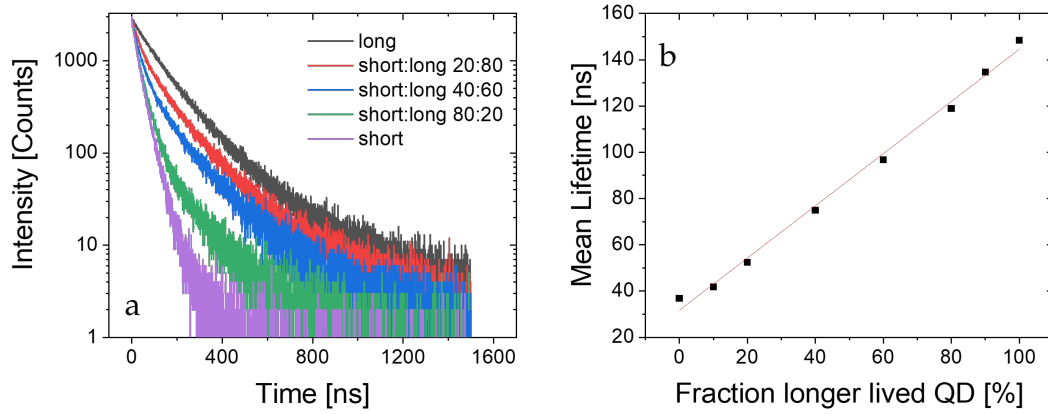
Figure 3.13: Fluorescence decay curves (a) and average lifetimes (b) of a simple two component GS-QD mixture. As can be seen in (b) the average lifetime is linearly dependent on fraction composition.

$$\nu_l = \frac{\tau_{mean} - \tau_s}{\tau_l - \tau_s} \tag{3.16}$$

where ν_l is the mixture fraction of the longer lived component, and τ_{mean}, τ_s and τ_l the mean lifetime of the mixture and the lifetime of the shorter-lived and longer-lived fluorophore respectively.

Secondly, the fluorescence decay curves of a mixture can be fitted by a superposition of the underlying fluorescence decays, as shown in Equation 3.17.[53, 54, 55]

$$I(t) = \sum A_i\, e^{\frac{-t}{\tau_i}} \tag{3.17}$$

where I(t) is the intensity at each time point, A_i the amplitude of the i-th fluorophore component and τ_i the respective lifetime. Since the QDs used in this work have shown decays which can generally be well described using bi-exponential decays, a more specific form can thus be written:

$$I(t) = f_1 \cdot \left(A_1\, e^{\frac{-t}{\tau_1}} + A_2\, e^{\frac{-t}{\tau_2}}\right) + f_2 \cdot \left(A_3\, e^{\frac{-t}{\tau_3}} + A_4\, e^{\frac{-t}{\tau_4}}\right) + f_3 \cdot \ldots;$$
$$\sum f_i = 1 \tag{3.18}$$

where the f_1, f_2, f_3 or f_i are the respective intensity fractions of the corresponding QD batch. Additionally, the mixture fractions sum to 100 %.

$$c = \sum \nu_i = 1 \tag{3.19}$$

where ν_i are the respective fractional concentrations. Combining Equation 3.19, Equation 3.6 and using the fractional intensities from Equation 3.18 and Equation 3.12, the fractional concentrations for a two QD mixture can be given by the following relationships:

$$
\begin{aligned}
I_1 / I_2 &= \frac{f_1 \cdot (A_1\, \tau_1 + A_2\, \tau_2)}{f_2 \cdot (A_3\, \tau_3 + A_4\, \tau_4)} = \frac{QY_1\, I_0\, k\, \nu_1}{QY_2\, I_0\, k\, \nu_2} \\
&\to \nu_2 = \frac{1}{\frac{f_1 \cdot (A_1\, \tau_1 + A_2\, \tau_2) QY_2}{f_2 \cdot (A_3\, \tau_3 + A_4\, \tau_4) QY_1} + 1} \\
\nu_1 &= 1 - \nu_2
\end{aligned}
\tag{3.20}
$$

3.7 Coupling strategies

Attachment of specific molecules or molecular moieties of interest to antibodies or other biomolecules is a long studied work and various so called bioconjugation strategies have been developed already. The demands on such a reaction are manifold, e.g. high yield, mild reaction conditions, biocompatibility, and high specificity.[51, 56, 57, 58, 59, 60] In this work, two different standard bioconjugations have been explored for coupling QDs to antibodies. Aim of these conjugations was to introduce a specific binding property to the QDs, allowing their use as specific biolabels.

3.7.1 EDC-NHS coupling

1-ethyl-3-(3-dimethylaminopropyle)-n-hydroxysuccinimide (EDC-NHS) coupling is a specific reaction pathway to couple carboxylic acid groups to nucleophiles, usually amine moieties, resulting in a final amide bond. Using the EDC, the carboxylic acid groups are activated, usually at slightly acidic pH of 4.5 - 6. The highly reactive species is then stabilized by esterization with the NHS to prevent side reactions, especially when using water as solvent. The final conjugation step is usually performed at slightly basic pH of 7.5 - 9, as shown in Figure 3.14.[61, 62]

The reaction usually shows high yields as well as being easy and fast to perform. Main disadvantage of this coupling strategy is its low specificity, since any amine group or indeed any nucleophile can react with the NHS-ester moiety. For proteins, especially larger ones such as antibodies, no regioselectivity can be guaranteed, as any of the many available nucleophilic sidechains may react. This may also lead to loss of function, if any of the sidechains are important for the function of the coupled protein participated in the coupling reaction.[57]
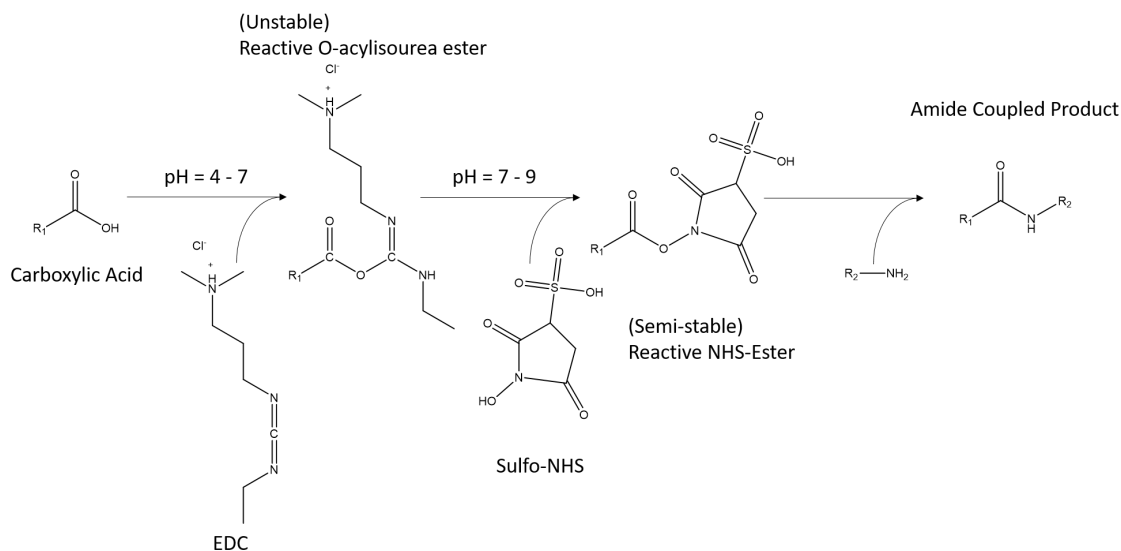
Figure 3.14: Reaction scheme of the EDC-NHS coupling. In a first step, usually at slightly acidic pH, the carboxylic function is activated by addition of EDC. The highly reactive intermediate is stabilized by addition of sulfo-NHS at slightly basic or neutral pH, yielding a NHS-ester. This intermediate is more stable against reaction with water, preventing the unwanted back reaction to the carboxylic acid. The NHS-ester readily reacts with amines, leading to the formation of the final, stable amide bond and completing the coupling reaction.

3.7.2 Azide click chemistry

This copper free click reaction is based on a ring-opening of a dibenzocyclooctyne moiety with azides. Due to the high ring stress, no copper catalyst is needed, as would usually be the case with this click reaction.[51, 63, 64] This reaction is known for high yields and has the advantage of full bio-orthogonality, meaning no reaction groups are involved which can be found in natural biomolecules. This in turn is also its biggest disadvantage, as such groups have to be introduced into the biomolecule to allow for the reaction to take place, making further reaction steps necessary. A reaction scheme is shown in Figure 3.15.

Using antibodies and applying reductive amination to incorporate a dibenzocyclooctine (DBCO) function, a regio-specific coupling is possible, contrary to EDC-NHS coupling, where the reaction takes place at random parts of the antibody. In a preliminary step, the antibody is functionalized using reductive amination. First, the glycol sugar moieties, mostly found in the F_C region of the antibodies, are oxidized to reactive aldehydes. These can then be aminated in a second step by the $DBCO-NH_2$ via the amine group. The alkine bond of the octyl ring stays unchanged during this process. Afterwards, unreacted aldehy-
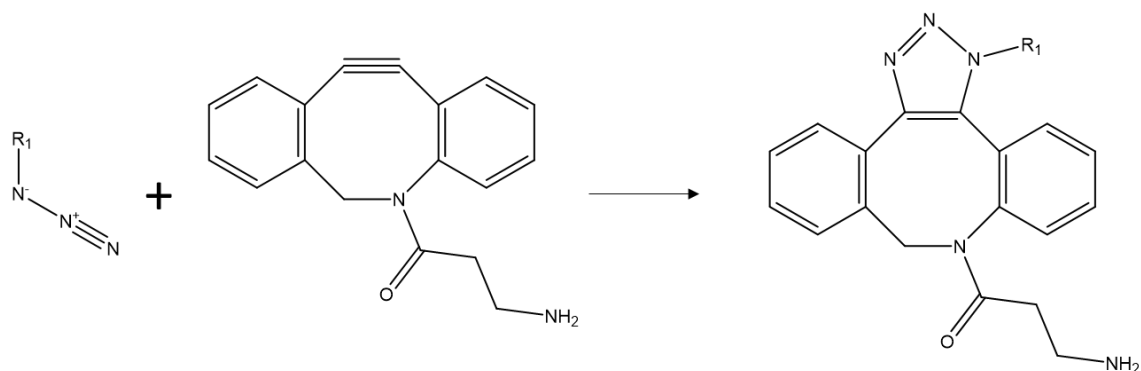
Figure 3.15: Azides react readily with the alkine function of the octyl ring due to the ring strain on the bond. Therefore, no catalyst is needed, as is usually the case for an azide-alkine reaction. During the reaction, a 1,2,3-triazol is formed. The reaction is highly specific, with high yields and resistant against most other chemical functions or impurities during the reaction.

des are reduced back to their native diol form by a mild reducing agent. The sugar chains in antibodies are usually added in post-translational glycolisation steps. The glycosylation sites for these are mostly located in the F_C region, hence a regio-selectivity is imparted by the reductive amination. This method avoids the antigen-binding sites generally found in the light chains of an antibody, thus preserving a high reactivity of the antibodies.[65] A full reaction scheme is shown in Figure 3.16.

a)

Antigenbindingsite

Lightchain

Fc region

Glycolated polysaccharide chains

Heavychain

b)

c)
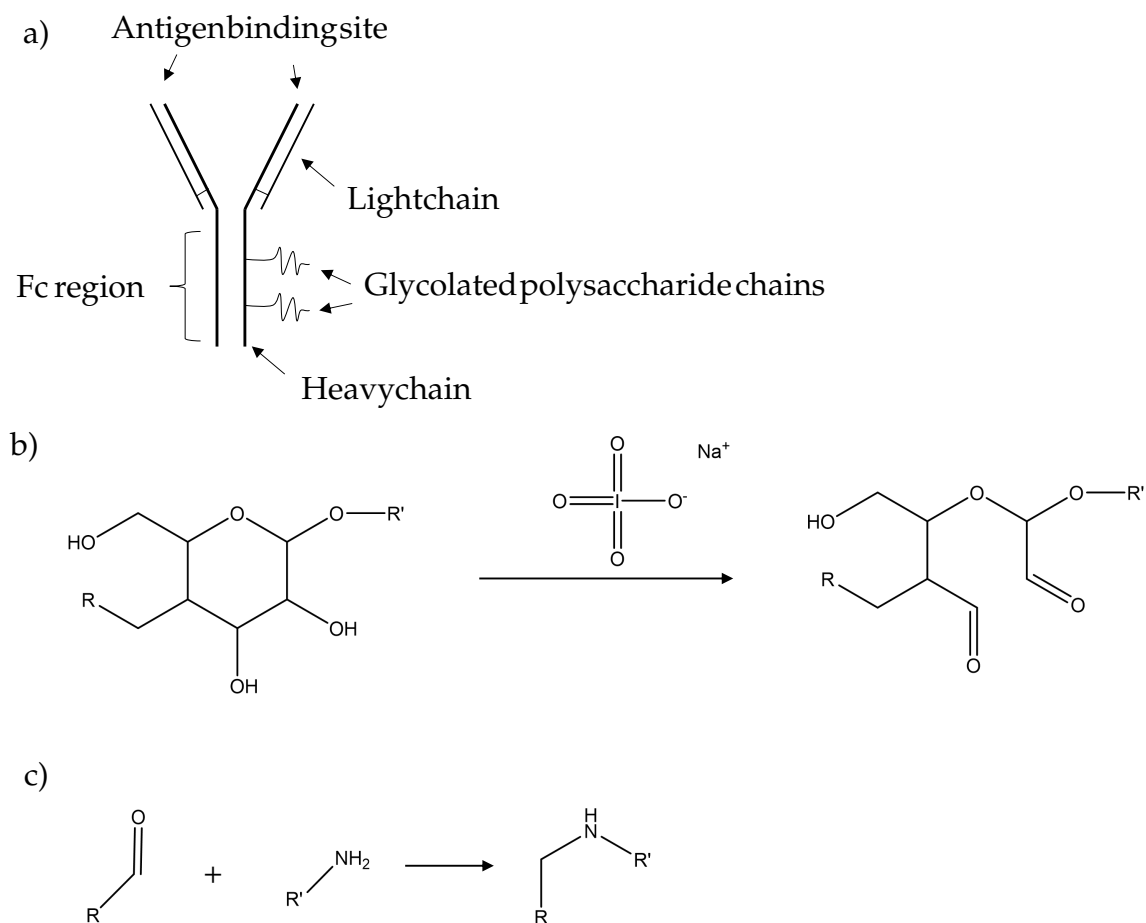
Figure 3.16: Scheme of the functionalization of the antibody with DBCO-amine by reductive amination. (a) shows the general layout of an antibody, (b) the activation of a glycol in the polysaccharide chain using a possible internal mannose residue and (c) shows the reductive amination of the activated aldehyde.

4 Materials and Methods

4.1 Chemicals

Octadecene (90%) (ODE), toluene, n-Hexane, ethanol, acetone, isopropanol, chloroform, azobis(isobutyronitrile) (AIBN), VA-044, 1-ethyl-3-(3-dimethylaminopropyle) (EDC), sulfo-n-hydroxysuccinimide (sulfo-NHS), dibenzocyclooctine-amine (DBCO-Amine) were purchased from Merck. Sodium periodate, sodium cyanoborohydride, Dulbecco's modified eagle medium (DMEM), streptomycine, peniciline, glycin, saponin, bovine serum albumin fraction V (BSA V), resazurin (sodium salt), Triton X-100 solution and phosphate buffered saline solution (PBS) were procured from ThermoFisher. Fetal bovine serum (FBS) was bought from VWR Chemicals. Rabbit anti-EEA1 (MA5-14794), mouse anti-EpCAM (14-9326-82) and mouse anti-LAMP1 (MA1-164) primary antibodies were purchased from ThermoFisher. Mouse anti-Tubulin primary antibodies (T8328) were ordered from Sigma Aldrich. Goat anti-mouse (15343906) and goat anti-rabbit (15450834) secondary antibodies were procured from Fisher Scientific. Ultrapure water purified by a Purelab Flex system (Elga) was used for all experiments (R $\geq$ 18.2 MΩ resistance).

4.2 QD synthesis

The synthesis is based on the GS-QD synthesis developed by Chen et al.[66] Briefly, CdSe cores with sizes of 3-4 nm were synthesized, washed to remove residues and then redispersed in ODE. CdS shells were then grown using the successive ion layer adsorption and reaction (SILAR) method until a total QD diameter of 12 - 15 nm was reached.

4.3 QD phase transfer to water

The QDs were precipitated in their native organic solvent by addition of ethanol ($\approx$ 1:1) to remove excess ligands. The precipitate was redissolved in THF con-

taining a 2000 times excess of the PB-b-PEO polymer (M = 15000 g/mol, M(PB) $\approx$ 5000 g/mol). If needed, vigorous shaking or a short time of ultrasonification was applied to redissolve the QDs. Then a radical initiator (AIBN) was added, in $\frac{1}{3}$ excess compared to the C-C double bonds present in the PB-PEO. The solution was filtrated (PTFE, 0.22 μm) and then quickly transfered to water using a Nemesys fluidics system (Cetoni GmbH, Germany). During transfer, every 1.6 mL of THF solution were mixed with 14.4 mL of water. The solution was then heated to 80 °C for at least 8 hours to initiate and complete the radical emulsion polymerisation. The resulting QDs, encapsulated with a PB-b-PEO polymer shell (QD@PB-PEO), were purified using a glycerol density gradient[67] to remove empty micelles and micelles with more than one QD per micelle.

4.4 Fluorescence lifetime measurements

The TCSPC experiments were performed using a Fluotime300 by Picoquant (Berlin, Germany). QDs were excited at 450 nm, lifetime was determined at their respective emission maximum. A SuperK Fianium (NKT Photonics, Denmark) white laser source with a LLTF Contrast monochromator (NKT Photonics, Denmark) was used for excitation. Samples were usually excited at 450 nm.

4.5 Simulation of QD mixtures

For the simulated curves fluorescence decay curves of real samples were taken. Base curves were extracted from pure QD samples by applying bi-exponential fits to their fluorescence decay. Noise was generated by subtraction of these base curves from the measurements. Such decay curves and the corresponding noise can be seen in figure 4.1.

4.6 EDC-NHS coupling

QDs@PB-PEO with carboxylic endgroups were used for the EDC-NHS coupling of antibodies. The desired amount of QDs was diluted 1:1 with PBS buffer. Then, 10 eq. EDC and 20 eq. sulfo-NHS were added and the solution stirred for 15 min at room temperature (RT). Unreacted reactants were removed via a centrifugation filter membrane (Vivaspin, 100000 molecular weight cutoff (MWCO)) for 5 - 10 min, 6000 g, RT. Afterwards, 30 eq. of antibodies were added and the reaction stirred for at least 2 hours at room temperature. The solution was purified and
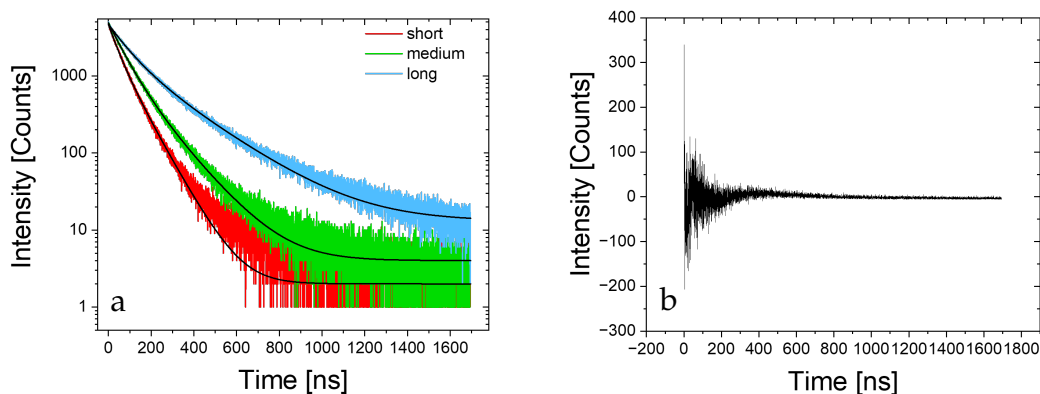
Figure 4.1: Measured decay curves of three different QD batches, short lived QDs, medium long lived QDs and long lived QDs, and their respective fitted decay curves, shown in black, (a), as well as the extracted noise, (b). Note that due to the logarithmic scale the deviations of the fit in the tail section of the curves look to be more significant, than they actually are.

washed by three cycles of centrifugation with a centrifugation filter membrane and redispersing in PBS.

4.7 Reductive amination of antibodies - conjugation of DBCO

DBCO-amine was introduced into the IgG antibodies (M $\approx$ 150000 g/mol) via reductive amination. Firstly, the sodium azide commonly used as an additive for IgG antibodies was removed by centrifugation with an Amicon 0.5 mL ultra centrifugal filter (50000 MWCO) (8 min, 16000 g, RT). The solution was washed and redispersed in 500 ν L PBS for three times. Then, glycolysated side chains present in the antibodies were activated by addition of 550 eq. of sodium periodate for 30 min, at RT in the dark. The activated antibody solution was then washed three times using a centrifugal filter again. Then, 1000 eq. of DBCO-amine were added for 4 hours at rt. Unreacted oxidized carbohydrates were then reduced by addition of 500 eq. sodium cyanoborohydride. The such functionalized antibodies (IgG@DBCO) were then purified using a PD-10 desalting G25 column and the fractions analyzed using UV-Vis spectroscopy. Fractions containing antibodies were combined and concentrated using a centrifugal filter.

4.8 Azide coupling

QDs@PB-PEO containing azide endgroups were used for the azide coupling of antibodies. QDs were stirred with 30 eq. of IgG@DBCO overnight at RT. For purification and removal of unreacted antibodies, the QDs were precipitated via three cycles of centrifugation (30000 g, 8 °C, 1 hour) and the supernatant discarded. The QDs were then redispersed in water.

4.9 QD exposition to live cells

HeLa and MFC-7 cells were grown in DMEM supplemented with 10 % FBS and 5 % peniciline and streptomycine mixture. QD incubation was performed in IBIDI 15x-Slide 8 wells, with 50000 cells per well. The QDs (typically 1 - 10 nM) were incubated sequentially each at 37 °C for 8 to 12 hours and the cells were washed three times before the next incubation. For the microscope measurements the cells were fixed with 4 % paraformaldehyde solution and resuspended in sterile PBS buffer. The lysosomal and nucleus stainings were applied as advised by the manufacturer. No toxicity of the QDs at the used concentrations was observed during incubation period.

4.10 Staining of fixed cells with QDs

Cells were grown as described above. After seeding in an IBIDI 15x-Slide 8 wells (50000 cells per well), the cells were fixed with 4 % paraformaldehyde solution. The cells were then permeabilized with either a solution of glycin and saponin (150 mg and 15 mg respectively, in 30 mL PBS buffer) for 5 min at 37 °C or by applying 0.1 % Triton100X solution for 30 minutes at 37 °C. The cells were then blocked with a solution of BSA fraction V (280 mg, in 14 mL of permeabilization solution made by glycin and saponin) for 25 minutes at 37 °C. Primary and secondary antibodies were applied as advised by the manufacturer. QDs with antibodies conjugated to them were incubated at 5 - 10 nM for 1 hour at 37 °C. If needed, nucleus staining were then performed as advised by the manufacturer.

4.11 Cell viability assays

The cell viability assays were performed in 96 cell culture well plates by TH.Geyer. For HeLa cells, 7500 cells were seeded per well. For MFC-7 cells, 10000 cells per

well were seeded. 0.1 mL of DMEM, containing 10 % FBS and 0.5 % of strepto-mycine and penicillin each, were applied per well. After the exposure, the cells were washed twice with PBS and a 0.02 mg/mL resazurin solution was added. This was incubated for 4 h at 37 °C in a 5 % CO_2 atmosphere. The fluorescence of the resazurin, at 590 nm, was evaluated using a TECAN infinite M200, with an excitation wavelength of 560 nm. Viability was determined as a fraction of fluorescence intensity compared to a control well.

4.12 Dotblots

Nitrocellulose membranes were used for the dotblots. First, primary antibody was dropcasted onto the membrane and marked on the membrane (1-5 μL, dilution as advised by the manufacturer). After drying, the membrane was blocked for 1 hour at room temperature with blocking solution, as described above. Then, the membranes were incubated with the QD conjugated to secondary antibodies overnight(c(QD) $\approx$ 1 - 3 nM). The membranes were then washed with water and illuminated with a UV flash light.

4.13 Confocal microscope measurements

Confocal microscope images were taken using an Olympus FV1000 microscope. QDs were excited using a 405 nm laser, lysosomal stains (fluoresceinisothiocyanate) using a 488 nm and nucleus stain (syto deep red) using a 633 nm laser. Images were taken using either a 40x or a 60x oil objective.

4.14 Fluorescence lifetime imaging

FLIM measurements were performed using the same microscope as above. A Picoquant Sepia picosecond diode laser with 405 nm wavelength was used as a pulsed laser source. The pulse frequency of 1 MHz was applied by an external arbitary waveform generator, a DG1022 by Rigol. Excitation light was filtered out using a 430 nm longpass filter. Each pixel was scanned for 40 s per scan and typical images were taken over several minutes. Measurement data was fitted using a self-written script in Python including the lmfit package[68].

4.15 Acknowledgement

5 Results and Discussion

5.1 Optical properties of giant-shell quantum dots

Giant-shell quantum dots (GS-QDs), CdSe QDs with CdS shells of > 10 mono-layers of CdS, have shown very useful properties with regards to fluorescence lifetime multiplexing, like strong absorption, suppressed blinking and long fluorescence lifetimes.[66, 69, 70]. As usual with QDs, upon growth of the CdS shell, a red-shift of absorption and emission spectra is observed. This red-shift levels out with increasing size[69, 70], making the final emission colour only dependent on core size. Therefore, GS-QDs of similar core sizes have similar emission colours. The same does not hold true for fluorescence lifetimes though. There, an increase in shell size will lead to an increase in fluorescence lifetime. Thus, this property allows for an easy preparation of samples with similar emission colours but completely different fluorescence lifetimes. This unique property to this fluorescent system makes GS-QDs extremely useful for lifetime multiplexing applications. An example of emission spectra and average fluorescence lifetimes are shown in Figure 5.1.
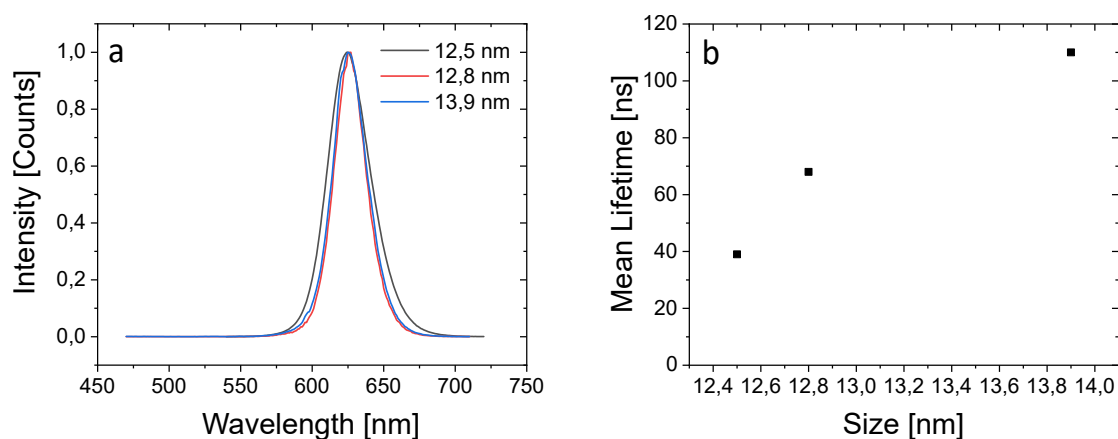
Figure 5.1: GS-QD fluorescence emission spectra (a) and lifetime (b) with respect to their size. It can be clearly seen, that increase of size has only a negligible effect on the emission colour, but increases the fluorescence lifetime drastically.

5.2 Properties of QDs encapsulated with a PB-b-PEO ligand shell

As described above, the encapsulation of the QDs in the PB-PEO ligand shell has various advantages, while preserving the desired optical properties of the QDs. The influence of the encapsulation on the properties of the QDs, such as fluorescence lifetime and colour, can be seen in the following figures.
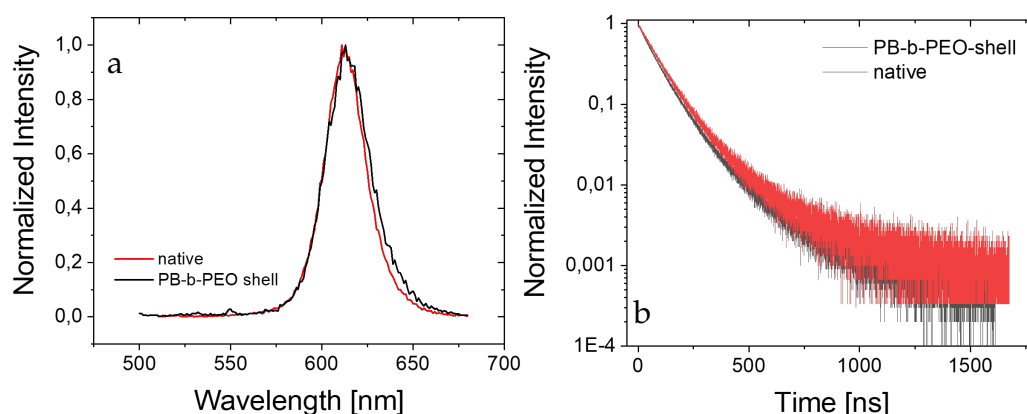
Figure 5.2: Normalized fluorescence emission (a) and decay (b) of QDs in their native media before the encapsulation and in water afterwards. Only marginal changes of the fluorescence properties can be observed.

As can be seen in Figure 5.2, the fluorescence properties are only slightly changed. By changing the amount of polymer excess during the encapsulation, the number of QDs per polymer micelle and consequently the final size can be finely tuned, as shown in Figure 5.3. With decreasing polymer excess, a higher number of QDs will be encapsulated within each polymer micelle, leading to a bigger size of each micelle.

A batch of mostly singly encapsulated QDs can be produced by utilizing very high excess of polymer (>1200) and purification by density gradient centrifugation. A TEM image of such a sample and the counted QDs per micelle are shown in Figure 5.4.
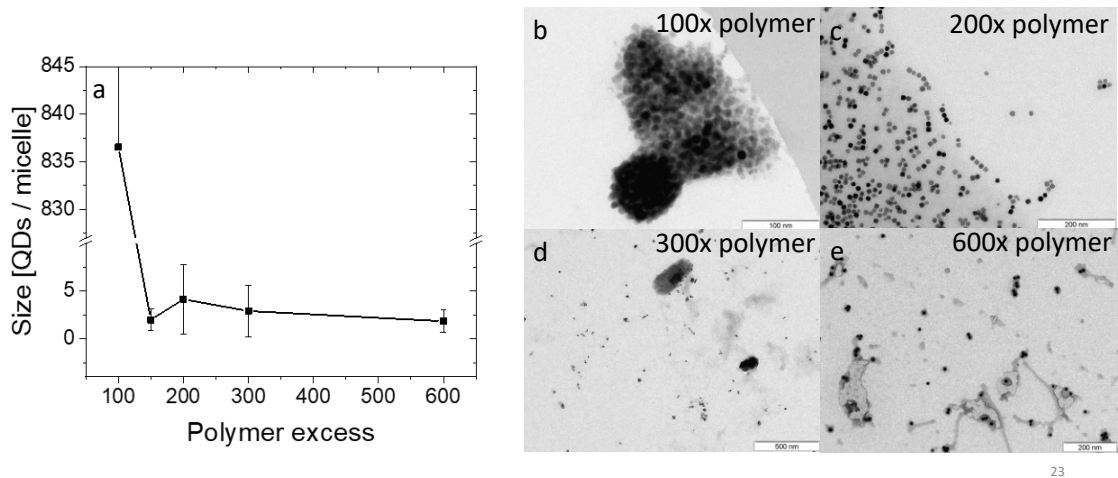
Figure 5.3: Number of QDs per polymer micelle (a) and respective TEM images of the encapsulated QDs (b-e). Clearly, the number and standard deviation of QDs per micelle decreases with increase of polymer excess during encapsulation.
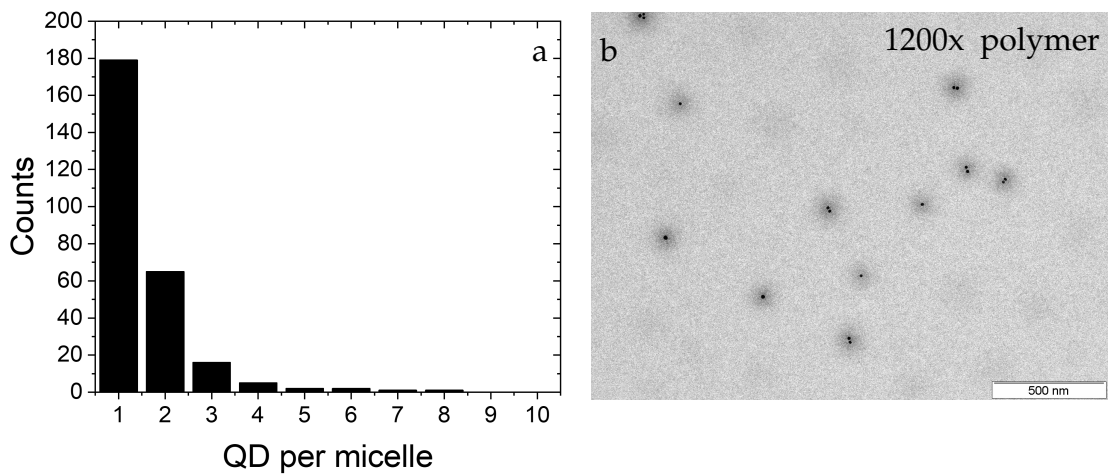
Figure 5.4: QD per micelle (a) and typical TEM image of a 1200x polymer excess QD sample after purification. QDs were counted, with roughly 66 % being singly encapsulated.

The polymer shell also stabilizes the particles in various media, as can be seen in Figure 5.5. There, QDs were incubated for 48 hours in DMEM cell medium, bovine albumin serum, phosphate buffer (PBS) as well as the blocking and permeabilization solutions used during fixation of cells. No aggregation could be observed nor an effect on fluorescence lifetime. As expected, the encapsulation in the PB-b-PEO-shell protects the QDs from the influence of the enclosing medium.
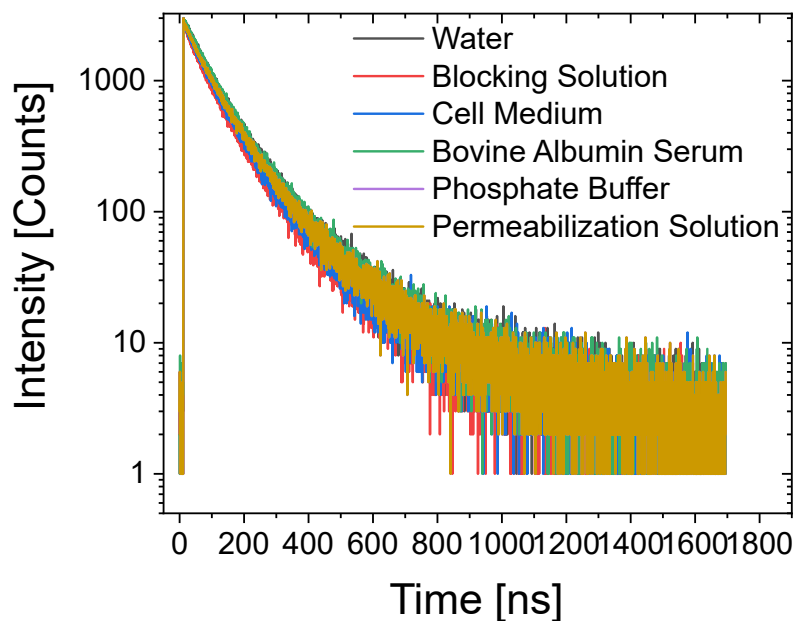
Figure 5.5: Fluorescence decay curve of QDs after incubation for 48 h in water and various biologically relevant media. Evidently, the fluorescence decay is not changed by any of the media.

The PB-b-PEO polymer shell therefore is quite suitable to preserve the optical properties of the QDs as well as stabilizing them in water and biologically relevant media.

5.3 Lifetime analysis of 2-QD mixtures

Various applications in bio-imaging benefit greatly from having precise information on whether mixed signals of fluorescent markers are present in each imaged pixel as well as the mixture fraction, if possible, as described above already. Two methods have been established for the use of lifetime analysis: Determination of mean lifetime and superposition of base fluorescence decays.[52, 53, 54, 55] This work strove to determine the precision and possible limiting factors of these

models. To this end, both models were applied to a number of simulated as well as measured fluorescence decay data.

5.3.1 Simulation of 2-QD mixtures

Simulated data was used to characterize the models for their precision in determining mixture composition. The base curves shown in Figure 4.1 were used to create simulated mixed decay curves. By applying the above described superposition model, the composition fractions of each of the QD batches were then calculated to be as shown in Figure 5.6.
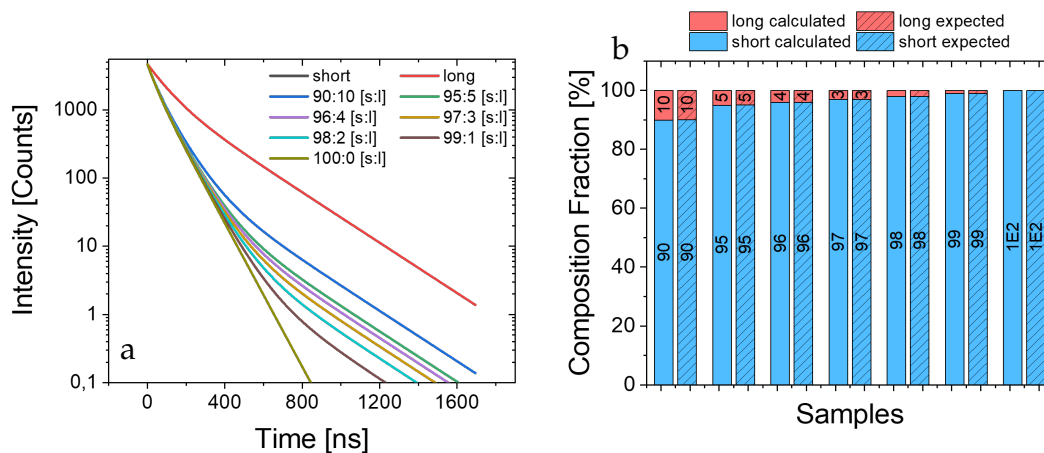

Figure 5.6: Simulated decay curves with no additional noise (a) and the respective calculated composition fractions using the superposition model (b) are shown. A selection of decays close to the extreme of a pure sample was chosen, as well as being close to each other in composition fraction. The decay curves matched the model perfectly, as no noise was applied. Therefore, the calculated compositions fractions match completely.

As expected, the calculated and expected fractions match perfectly, as no noise is introduced to the decay curves. Similarly, the results obtained by the mean lifetime model are shown in Figure 5.7.

Again, a perfect match between data and model result was obtained. The calculation of the fractions is straightforward, as the models are simply being applied to a perfect decay curve, without any interfering factors. The precision of the models is heavily dependent on the extraction of the fitted curve. With increasing noise, this becomes more difficult and errors in the calculation result. With the extracted noise, only a small error is expected, as demonstrated in Figure 5.8 and Figure 5.9.
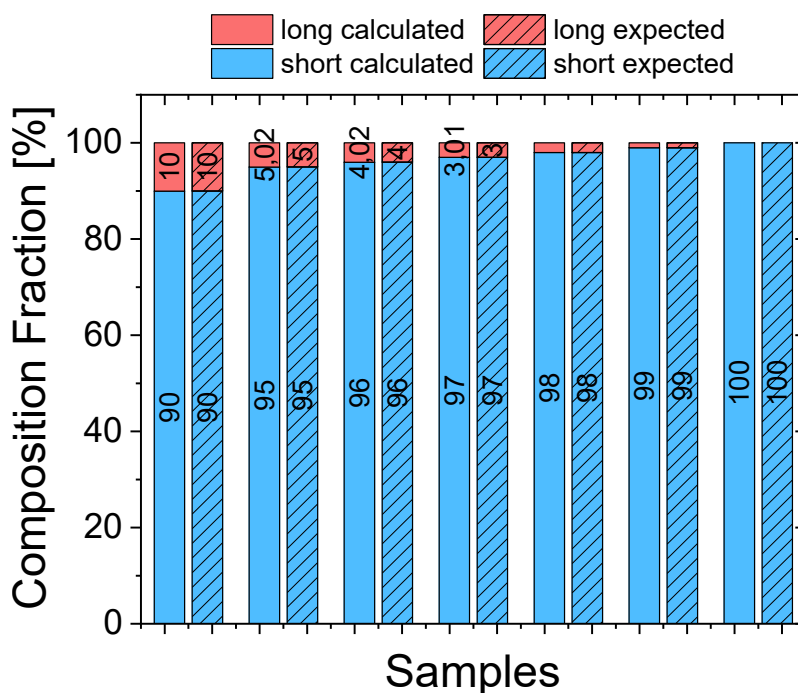
Figure 5.7: Calculated composition fraction of the curves shown in Figure 5.6 (a) using the linear model. As no noise was applied, the calculated compositions fractions match perfectly.
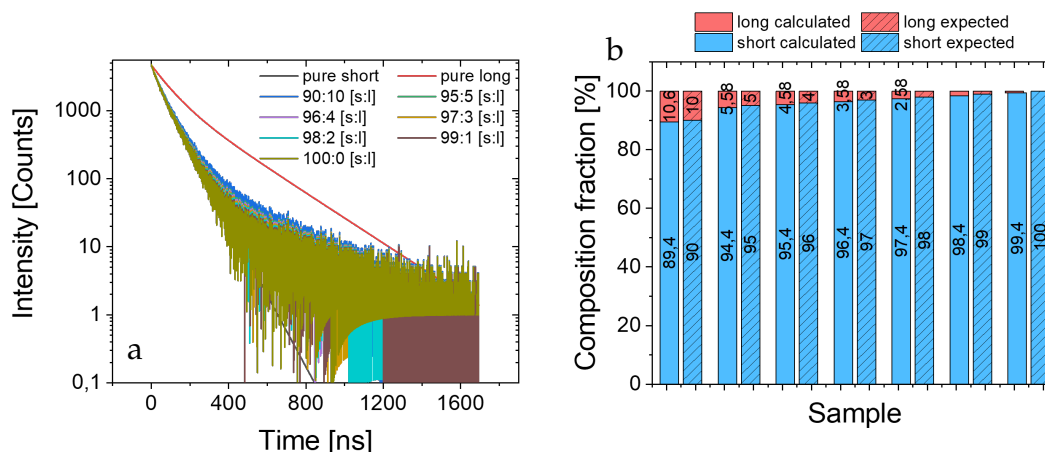

Figure 5.8: Simulated decay curves with a normal level of noise (a) and the respective calculated composition fractions (b) are shown. Due to the introduced noise, error arise in the calculated composition fractions. An error of approximately 0.5 percentage points can be observed compared to the decays with no additional noise. Still, this precision is good enough to distinguish e.g. between a 96:4 from a 98:2 mix.
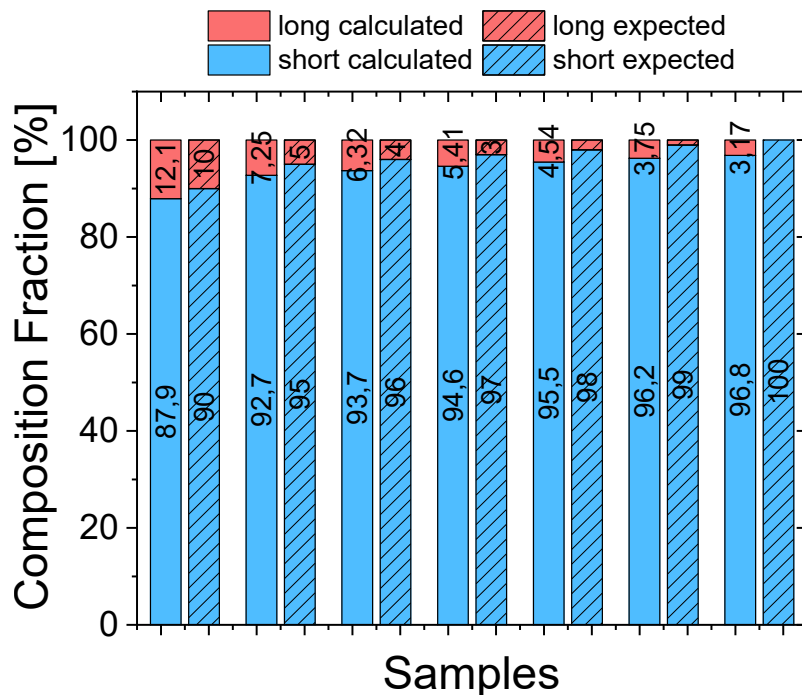
Figure 5.9: Calculated composition fraction of the curves shown in Figure 5.8 (a) using the linear model. The errors introduced by the noise are approximately four to six times as big as for the superposition model.

The linear model is easy to apply and use on samples, with calculations and results that can easily be verified by hand. Clearly though, from the results shown in figures 5.8 and 5.9, the superposition model allows for a better precision in the mixture fraction determination, than the linear model. The error in the mixture fraction is approximately four to six times smaller in the superposition model than the linear model. It is therefore always to be preferred, when the higher precision outweighs the slightly more complex usage of the superposition model.

Note that the introduced error in calculation is constant per sample, due to the way the simulated data was constructed. It scales linearly with the amount of noise added, as shown in Figure 5.10 (b). These errors lead to an overestimation of the long-lived QD fraction. Still, even with unreasonably high amounts of noise, a qualitative assertion of mixture remains possible for the superposition model. This model therefore seems suitable even for samples with high levels of background, e.g. while using organic fluorescence dyes in samples with high amounts of autofluorescence.

The results seen in Figure 5.10 reinforce the conclusion drawn earlier. The superposition model seems to be superior in the quality of the mixture fraction determination, being increasingly better, the noisier the measurement data is.
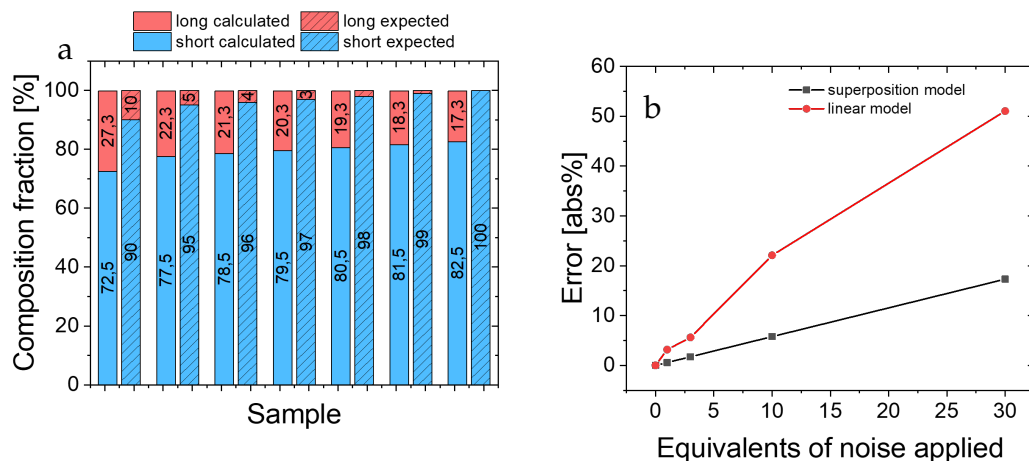
Figure 5.10: Calculated composition fractions with 30x noise using the superposition model (a) and increase of error with increasing noise for both models (b). Note that at 30x noise applied, the signal to noise ratio is ≈ 1.5:1 at best. While an error of approximately 17 percentage points is observed for the superposition model, this still allows the distinction between e.g. a pure sample and a 50:50 mixture. The error of the linear model is roughly three times bigger at this point, making it impracticable to use for such noisy samples.

5.3.2 Analysis of fluorescence lifetime of 2-QD mixtures

The limits determined by the simulations were similarly tested by measurements of real mixtures of QD batches with varying fluorescence lifetimes. Three QD samples with respective average lifetimes of 53.18 ns, 64.66 ns and 67.53 ns were used, subsequently called [s], [m] and [l]. The average lifetimes of different mixture compositions of these three samples were determined, the results of which can be seen in Figure 5.11.

It is clearly apparent, that with decreasing $\Delta\tau$, the ideal linear relationship of average lifetime to mixture fraction is lost. For the [s] + [l] mixture, with a $\Delta\tau$ of 14.35 ns, approximately 27 % of the smaller lifetime, the linear relationship still holds true, whereas for the [s]+[m] and [m]+[l] mixtures, with $\Delta\tau <= 11.48$ ns, approximately 22 %, the deviation from the ideal is already significant. As the simulations allow precise determinations of mixture fraction for even smaller $\Delta\tau$, the limits shown here result from the measurement instrumentation. From this, a temporal resolution can be defined, where a good mixture deconvolution with this model is possible. For the measurement setup used here it is $\Delta\tau >$ 27 %. Below this limit, the mixture can only be evaluated qualitatively, where pure samples still can be distinguished from e.g. 50/50 mixtures but no precise determination of the mixture fractions is possible.
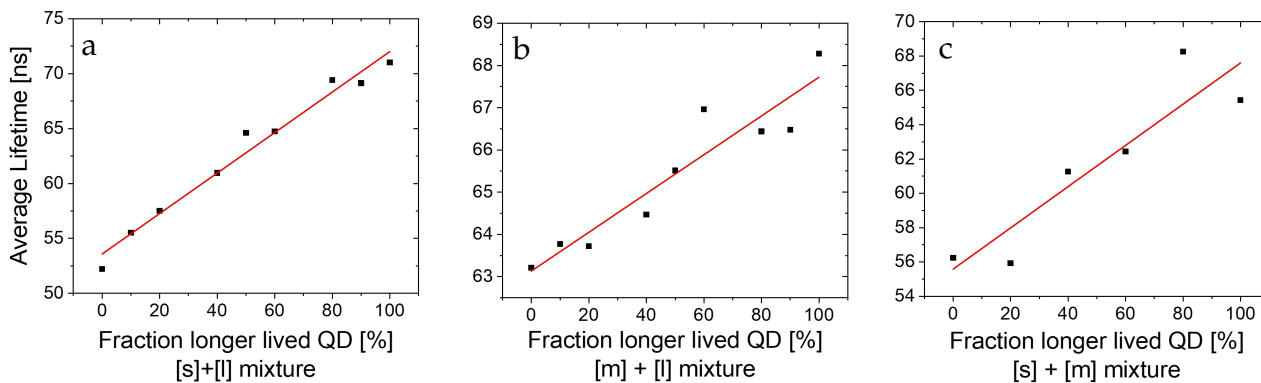
Figure 5.11: Average lifetimes of the three different mixtures between [s], [m] and [l]. Linear fits of these are shown with the red line. Only a slight deviation from this fit can be seen for the [s] + [l] mixture, shown in (a). The linear relationship for the [m]+[l] mixture, seen in (b), is still in good agreement, though a larger deviation from the linear behaviour can be observed. For the [s]+[m] mixture, the deviation from the linear behaviour is even more pronounced.

As expected from the results seen in the previous chapter, this limit can be overcome by using the superposition model to describe the samples, as can be seen in Figure 5.12 and Figure 8.1 (appendix). Here, the [s]+[m] mixture can still be predicted, with only minor deviations from the expected results. This model is therefore well suited to determine precise mixture fractions even for samples with only minor differences in their fluorescence decay behaviour.
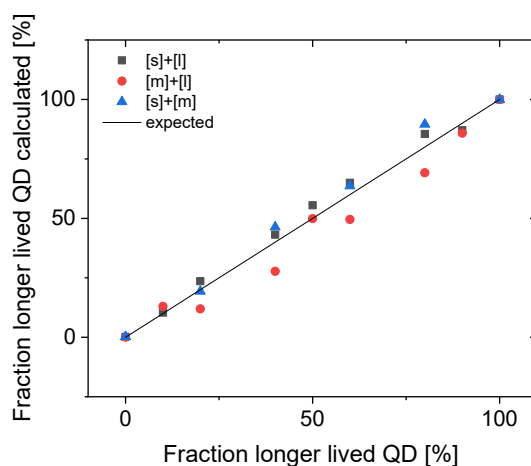
Figure 5.12: Calculated mixture composition for the [s] + [l], [m] + [l] and [s] + [m] mixtures by applying the superposition model. The results are generally in good agreement with the prepared samples. For the [m] + [l] mixture a slight underestimation of the longer lived component can be seen in the region of 20 - 40 % and 60 - 80 % mixture composition.

5.4 Lifetime analysis of 3-QD mixtures

Increasing the complexity of the mixture to three components brings several problems with it. While the model of a superposition still holds, a simple evaluation of the mean lifetime does not yield a single but several possible mixtures, as seen in Figure 5.13.
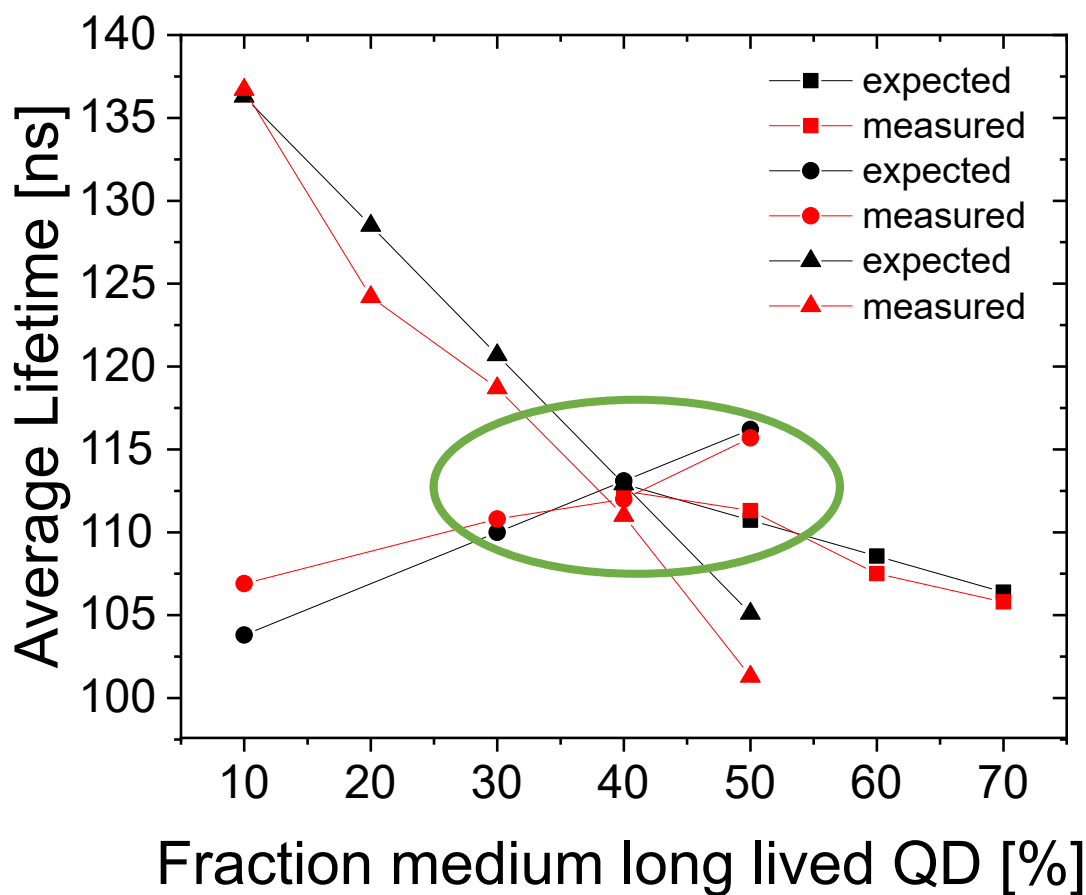

Figure 5.13: Average lifetime of three different three QD mixtures (triangle, rectangle and sphere respectively). The expected lifetimes, as predicted by a linear model, similar to the two QD mixtures, are shown in black, the measured lifetimes in red. A good agreement can be seen. The precise compositions can be seen in the Tables 8.1, 8.3 and 8.2. Clearly, all lifetime curves cross at approximately 112 ns mean lifetime, although the three samples differ strongly in their composition at this point (marked with the green ellipse).

Using the same equations, as for the two component mixtures (Equations 3.17 - 3.20), and expanding for three components the following relationships can be found:

$$\nu_2 = \frac{1}{1 + \frac{f_1 \cdot (A_1 \ \tau_1 + A_2 \ \tau_2)QY_2}{f_2 \cdot (A_3 \ \tau_3 + A_4 \ \tau_4)QY_1} + \frac{f_3 \cdot (A_5 \ \tau_5 + A_6 \ \tau_6)QY_2}{f_2 \cdot (A_3 \ \tau_3 + A_4 \ \tau_4)QY_3}}$$

$$\nu_1 = \frac{f_1 \cdot (A_1 \ \tau_1 + A_2 \ \tau_2)QY_2}{f_2 \cdot (A_3 \ \tau_3 + A_4 \ \tau_4)QY_1} \cdot \nu_2 \qquad (5.1)$$

$$\nu_3 = 1 - \nu_1 - \nu_2$$

Another advantage of the superposition model is, that over-fitting of a mixture by applying a more complex model leads only to minor errors in the results, if any at all. It is therefore possible to simply apply the more complex case of an e.g. three QD mixture model to the case of a two QD mixture, as long as the correct decay curves are included in the model. Due to the nature of the fits, components that are not needed are simply neglected in the calculations. Such results are shown in Figures 5.14 and 5.15, where a three QD mixture model was used to calculate the composition fractions of pure and two QD mixtures respectively.

The application of a three QD mixture model, based on short lived, medium long lived and long lived QDs on the pure samples of the respective QDs matches with the expected results. No significant errors are incurred by applying the over-complex model on the samples.

Similarly, for the two QD mixture of short lived and long lived QDs, applying the three QD mixture model leads to well matching results. In four samples, a slight error is introduced, as a small component of medium long lived QDs is predicted by the model. This erroneous medium component comes at the expense of the long lived component, which actually reduces the average error of the composition fraction. The errors in the calculation of the mixture fraction are 2.9 ± 2.2 percentage points for the samples shown in Figure 5.15 (a), whereas in (b) the error is only 2.1 ± 2.0 percentage points. This effect will not hold true for all kinds of samples. However, the composition fraction can be determined within ≤ 5 percentage points, even when using an over-complex model.
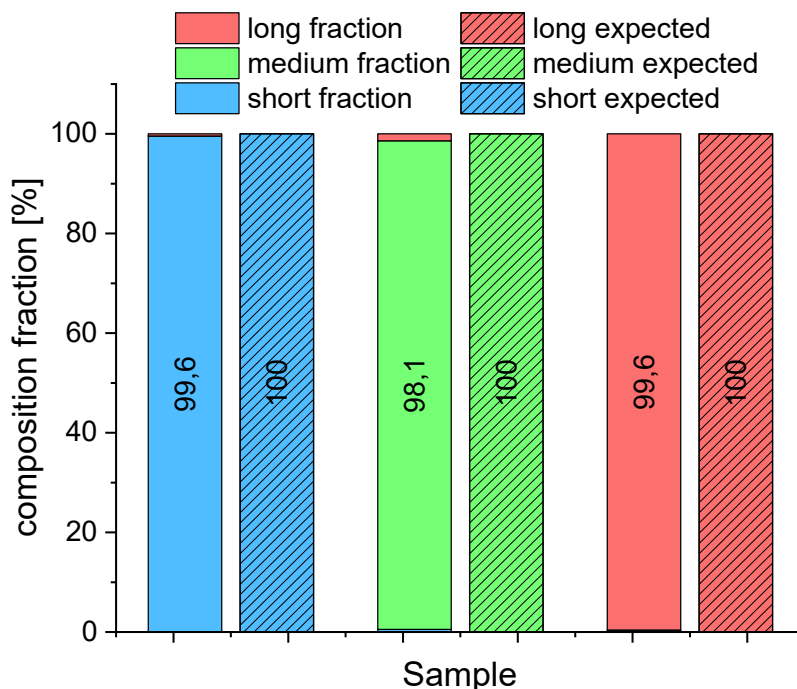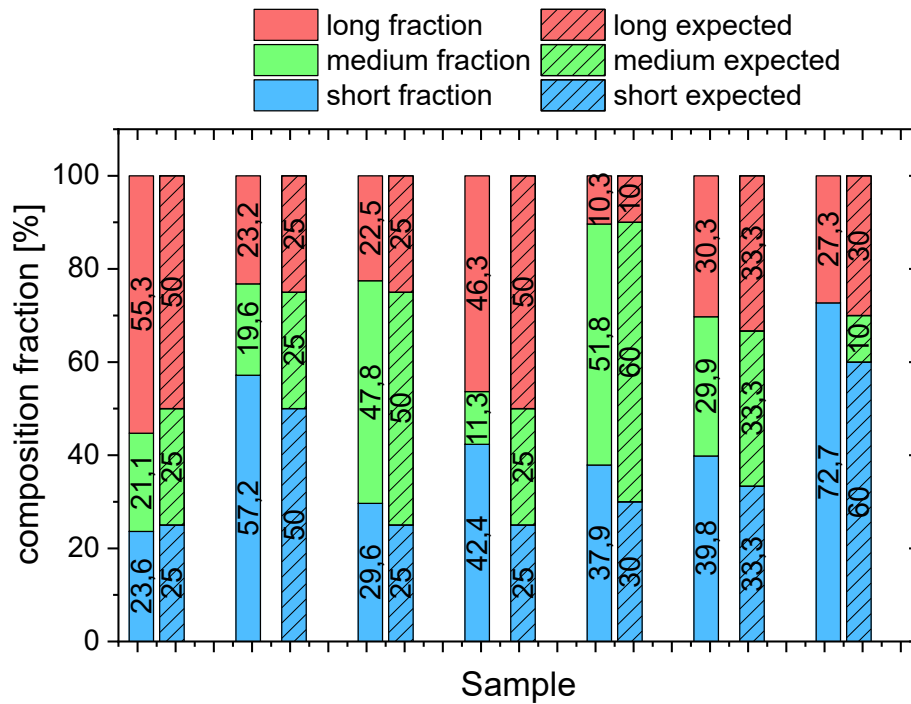
Figure 5.14: Compositions of different QD mixtures containing three different QD batches as calculated by a superposition model. The model included the superposition of a short lived, medium long lived and long lived QD sample. The samples were pure QD batches of these respectively. The left bar of each pair is the determined composition fraction in absolute % using the superposition model explained above. The right, hatched bar shows the expected composition fraction. The expected and calculated fractions match well. Only in the case of the medium long lived sample a small overestimation of the short lived fraction was predicted by the model.
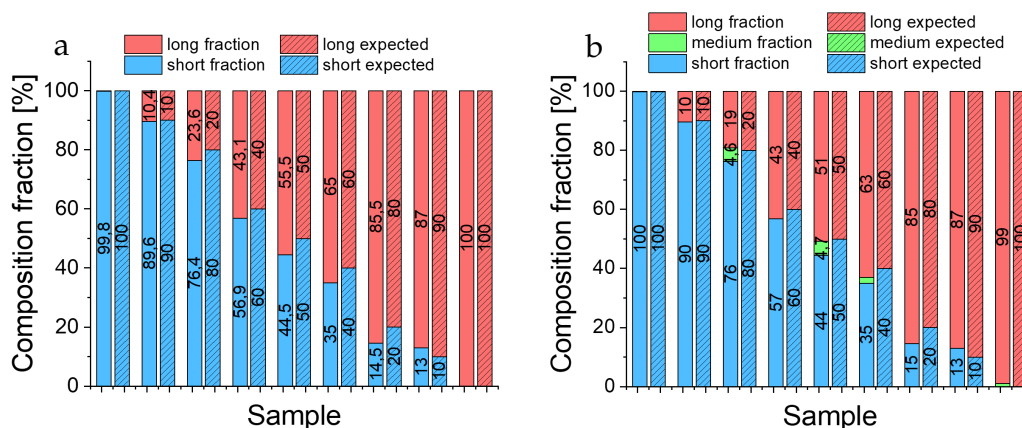
Figure 5.15: Calculated composition fractions of the samples [s]+[l] discussed above by applying a superposition model with 2 curves ([s] & [l]) (a) and 3 curves ([s], [m] & [l]) (b). The results are well matched in both cases. In (b), a slight amount of [l] is sometimes mistakenly attributed to signal from [m].

Figure 5.16: Compositions of different QD mixtures containing three different QD batches as calculated by a superposition model. The left bar of each pair is the determined composition fraction in absolute % using the superposition model explained above. The right, hatched bar shows the expected composition fraction. While the results generally match well, the medium long lived fraction seems to be systematically underestimated, while the short lived fraction is being overestimated. This leads to the complete disappearance of the medium long lived fraction in the final sample, where already only a small fraction is contained. The relative error of fraction composition for the long lived fraction is generally within 5 %.

As can be seen from the above figures, the superposition model does work in most cases and reliable fractions can be calculated using it. However, in the rightmost sample seen in Figure 5.16, the model fails to ascertain the correct fractions. Instead the medium long lived component is substituted by a larger fraction of shorter lived components, resulting in a calculated binary mixture instead of the true trinary one. This problem can be traced back to the numerical back calculation of the component fractions. Every possible solution can be described as a local minimum of the deviation of the fit from the actual measurements. The algorithms used in this approach try to find the global minimum, resulting in the best fitting curve to the data. This minimum does correspond to the true mixture in most cases, but does not necessarily do so.[40] Additional errors are incurred due to noise in the data set and the complex, more than mono-exponential, descriptions of the base curves. Two different strategies were applied to circumvent the aforementioned problems. First, the changing the fluorescence decay behaviour of the QDs to be mono-exponential, using post-synthetic modifications. Secondly, constraints on the number of possible solutions can be applied, hopefully removing any fit minima with a lower deviation from the data than the physically true solution. This was done by studying the most long living components of the decay curves and extrapolating back to the initial amplitudes.

5.4.1 Post-synthetic modification of QDs - optimization of fluorescence lifetime

The surface of the QDs might still contain unsaturated bonds, which might be saturated by addition of more ligands of different binding types. Thereby, the relaxation pathways of these unsaturated bonds or traps are quenched, so that only the radiative relaxation process remains. While syntheses for QDs with mono-exponential decay behaviour do exist, this highly useful optical behaviour is usually shown only at temperatures far away from room temperature[71] or for highly specific fluorescence emission peaks[8, 72]. To the best of the authors knowledge, no GS-QDs with such properties were described yet. Therefore, post-synthetic methods to influence the fluorescence decay behaviour were studied, based on the work of Houtepen et al.[19] Oleylamine (OAm) (Z-type) and cadmiumchloride (X-type) were studied as these additional ligands. Since $CdCl_2$ is not directly soluble in organic solvents, it was solved with 9 equivalents OAm in toluene, as suggested in the inspiring work. Nonetheless, the resulting solution is only colloidal stable at elevated temperatures. The influence of number of ligands and time of the ligand addition is shown in Figure 5.17. It can clearly be

seen, that short reaction times and high amounts of additional ligands lead to the best improvements of QY of the samples.
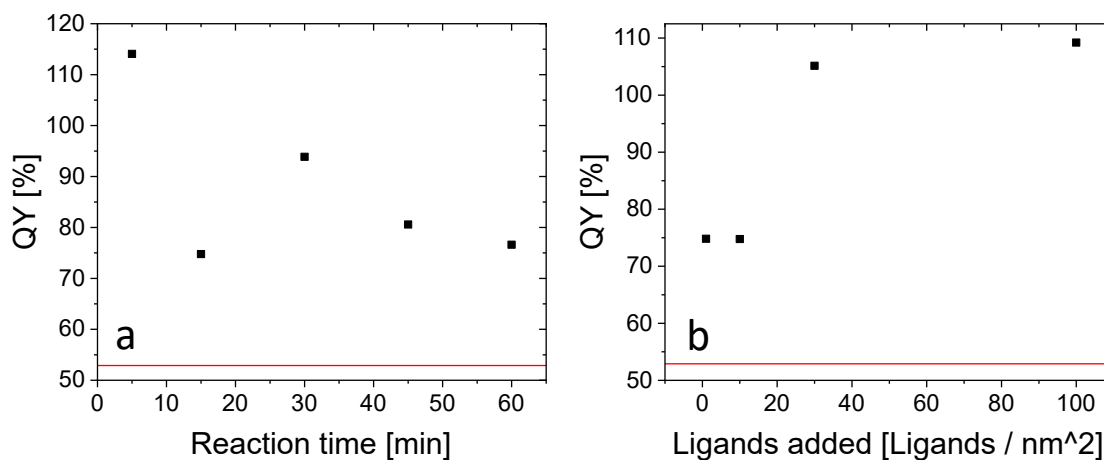

Figure 5.17: Influence of the number of added ligands (a) and reaction time (b) on the QY of GS-QDs. For (a), 30 min of reaction time was applied. For (b), 30 ligands/nm^2 were added. The ligand addition was performed at 95 °C. The QYs were determined relative to R6G in ethanol. Values above 100 % arise from overestimating the QY of the R6G solution used as for the relative QY determination. Its QY was assumed to be 95 %. The QY is increasing with added ligand amount, while it decreased with increasing reaction time. The QY of the QD before ligand addition is given by the red line.

The results of the fluorescence lifetime measurements, shown in Figure 5.18, are quite contrary to the results of the QY measurements. Unexpectedly, no significant change of the fluorescence decay could be observed.

It can be concluded, that this approach is unsuited to improve the reliability of the fluorescence lifetime superposition models. Nonetheless, the QY could be improved from roughly 50 % to almost unity, a remarkable improvement of optical performance.
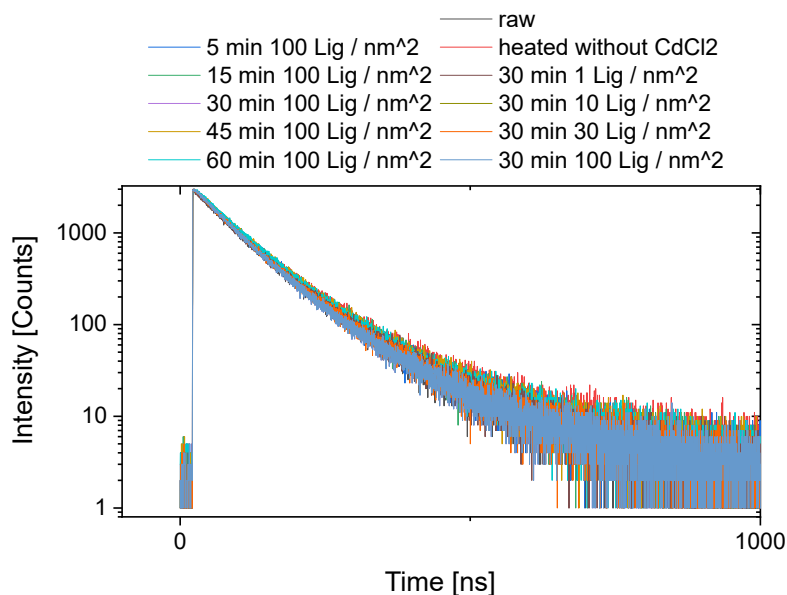
Figure 5.18: Fluorescence lifetime decay curves of the samples shown in Figure 5.17. No influence on the fluorescence decay can be seen.

5.4.2 Constraints on fit solutions - Timegating

In FLIM applications, time gates are readily used, where only data before or after specific times is evaluated. This allows e.g. to remove autofluorescence in an image by choosing a time point after which it has relaxed (almost) fully.[73, 74, 50, 75] Similarly, for the evaluation of the mixture components, a time point can be chosen, where most components have relaxed. As the base curves of the fluorescence decays are known, the theoretical fraction of initial intensity can be determined. This will yield an estimation for the amplitude of the longest living component of all the fluorescence decays. A scheme of this can be seen in Figure 5.19.

As the ratios of the amplitudes within one base decay curve are assumed to be constant, the amplitude of the longest living component also yields the amplitude of the respective shorter lived component and therefore the whole intensity fraction for that base curve. It can then be substracted from the measured decay curve, resulting in a decay curve that consists of only two remaining base curves, which can either be evaluated by repeating the process or by one of the methods shown above. This whole process is depicted in Figure 5.20.
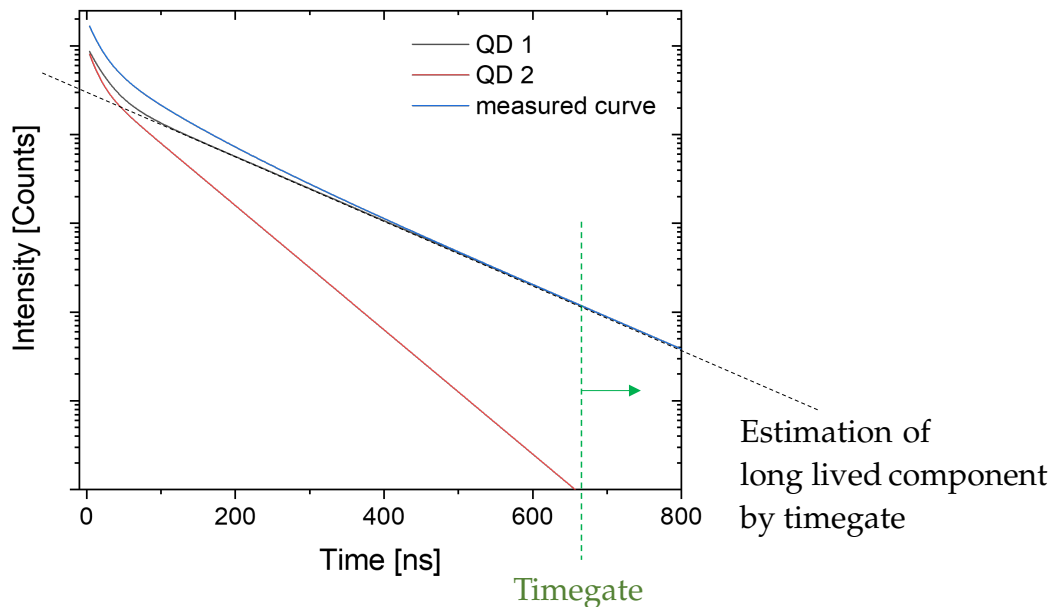
Figure 5.19: Scheme of the proposed use for time-gating to simplify the fit. A measured curve (blue) and the respective two QD decay curves, which constitute it (red and black respectively) are shown. Since the base curves are known, a time region can be chosen, where only the long lived component of one of the QDs has signal remaining, marked here in green. From this, an estimate of the amplitude for the long lived component of QD 1 can be made. It is also possible to gain the short lived component of QD 1 by the known ratio of the initial amplitudes. Thus, the QD 1 decay curve can be estimated in its entirety and, by removing it from the measured curve, only the decay of QD 2 remains. In practice, this model is complicated by noise and dark counts introduced during the measurement, as well as stronger overlap between the long lived components of the used QDs.

$$I = f_1\left(A_1\, e^{t/\tau_1} + A_2\, e^{t/\tau_2}\right) + f_2\left(A_3\, e^{t/\tau_3} + A_4\, e^{t/\tau_4}\right) + \; ...$$

repeat (if needed)

Extract: $f_1 \cdot A_2$

f_1, A_1, A_2 is now known

Substract the long lived component
from the inital curve
$$\left(f_1\left(A_1\, e^{t/\tau_1} + A_2\, e^{t/\tau_2}\right)\right)$$

Evaluate by
e.g. superposition model
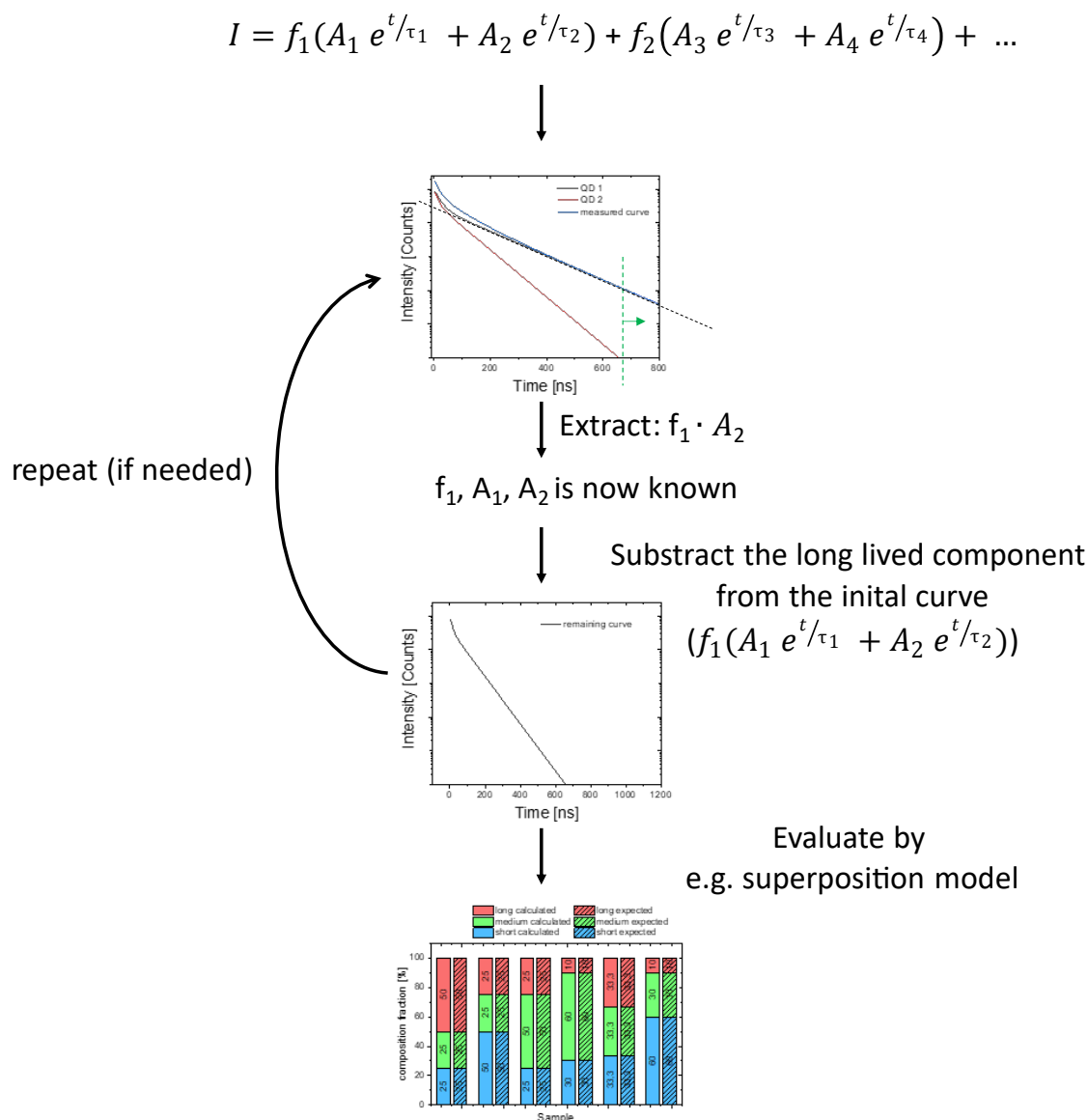
Figure 5.20: Overview of the use of time gates to constrain possible fit solutions. The superposition model is used to estimate a good time point for evaluation of the longest living component. From that point, the amplitude of that component is extrapolated back to the initial amplitude. This yields the intensity fraction for the respective base curve in the superposition model. Next, the curve can be substracted from the observed decay and the process either repeated to yield the next longest living component in the decay or immediately evaluated using a different method.

To ensure that a time point was chosen, where only the longest living component still contributes in a significant margin, three conditions were applied. These are based on the theoretical expected signal *A(t)* at a given time *t*, where the signal strength is given by:

$$A(t) = e^{\left(\frac{-t}{\tau}\right)} \cdot 100 \ [\%] \tag{5.2}$$

where τ is the fluorescence lifetime of a given component of the fluorescence decay, as determined by e.g. bi-exponential fit. The three conditions for a good time point for a time gate are:

Firstly, that the expected remaining signal of the longest living component makes up >90 % of the expected signal. Secondly, that the expected remaining signal strength of the longest expected decay component is > 2 %. Thirdly, that, if the first can not be satisfied, that it is weakened, until both conditions can be satisfied or the first condition was weakened for 30 iterations. Each time, the first condition is changed to be only 95 % of the formerly required value, so from >90 % to >85.5 %, to 81.225 % et cetera. With 30 iterations, this leads to a final value of >32.3 % for the first condition. This method was evaluated using the simulated data used in Figures 5.6 and 5.8 again. The resulting composition fractions are shown in Figure 5.21.
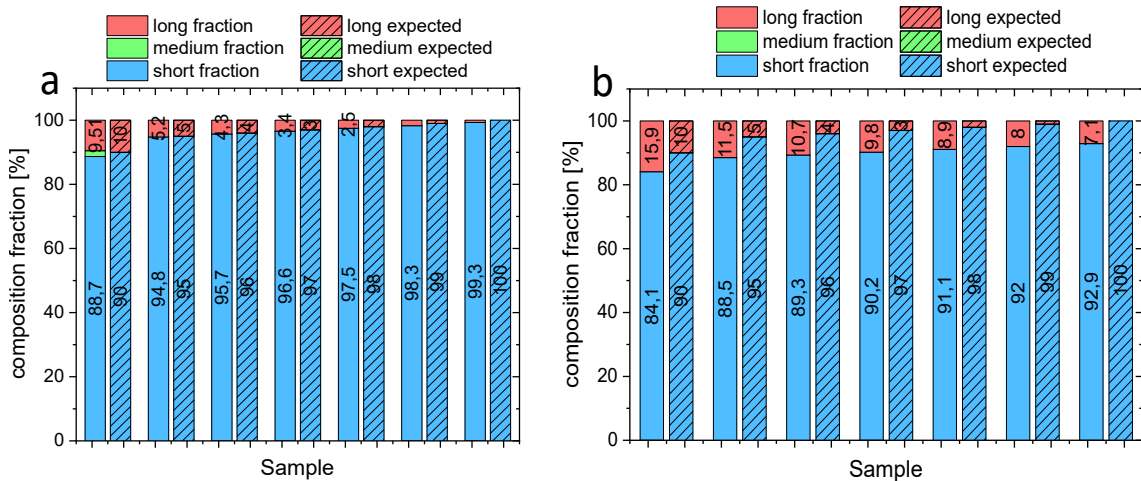
Figure 5.21: Calculated and expected compositions fractions of the simulated data using the superposition model with the addition of timegates can be seen in Figures 5.6 and 5.8. (a) shows the results for the simulations without any noise applied, whereas (b) shows the results for the data with one equivalent of noise applied. The results for (a) are in good agreement with the simulated data, whereas for (b) an over-estimation of the long lived component is noticeable.

Without any noise applied to the decay curve, the fit results and the data are
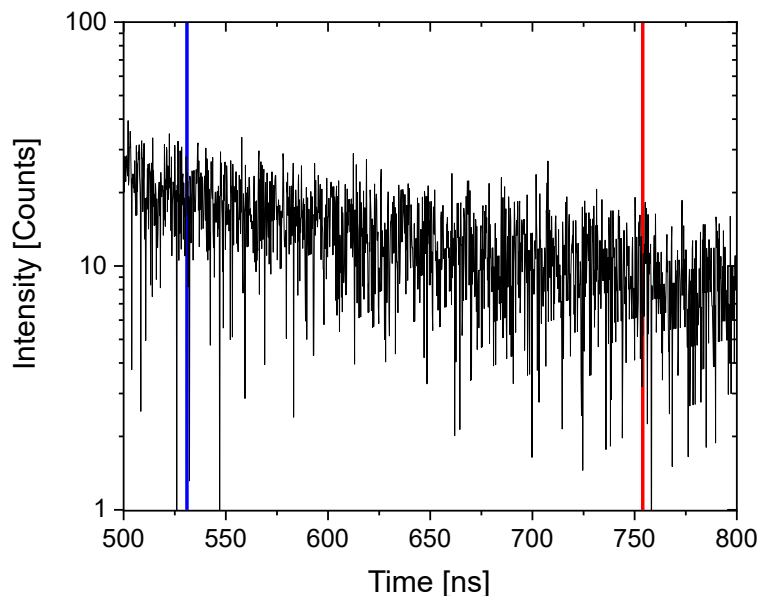
Figure 5.22: Section of the fluorescence decay curve for the 97:3 sample shown in 5.21. The blue line denotes the found time gate for the 2-QD model ($\approx$ 541 ns). The signal count at this point is about 24 counts. The red line shows the corresponding time gate for the overcomplex 3-QD model ($\approx$ 754 ns). The found intensity there is only about 6 counts.

in good agreement, as expected. However, for 5.21 (b), a significant overestimation of the long component is noticeable. This overestimation is a result of the extrapolation at a time point, where the signal is dominated by the noise, as seen in Figure 5.22. There, the time gates found for the 2-QD and the 3-QD model are shown. The intensity in the latter case has diminished by such a degree, that even a slight absolute error in the found amplitude, introduced through the noise, will have a significant relative error in the determination of the initial amplitude of the long lived component. Here, a deviation by one count in the 2-QD model will lead to a 5 % error, whereas in the 3-QD model, the error will already be 16 %. Therefore, the calculated amplitude of the long component becomes much too high or too low. Thus, no over-complex model should be applied to a mixture, if possible, to avoid having to choose a later time point for the time gate and potentially increasing the error during the determination of the amplitude of the longest living component. This is a big disadvantage of this method, compared to the superposition model without any constraints, where an over-complex fitting model will introduce only minor errors, if any.

The samples evaluated in Figure 5.16 have been reevaluated using this method, shown in Figure 5.23
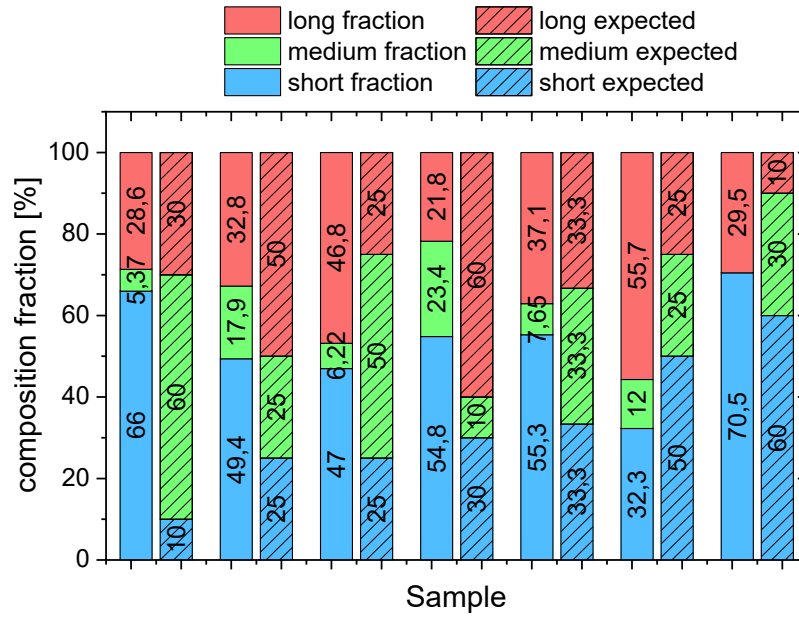
Figure 5.23: Calculated mixture fractions using the superposition model in conjunction with time gates. The same samples as in Figure 5.16 were evaluated. However, the introduction of the time gates does not seem to improve the performance of the model.

Clearly, the usage of the time gate does not improve the overall performance of the model in predicting the correct mixture fractions. In some samples, it does lead to an improvement of the estimation of the long lived component, but overall a decrease of estimation precision is observable. Therefore, using time gates does not alleviate the problems of the superposition model in the case of 3 QD mixtures.

5.5 Coupling of antibodies to QDs

5.5.1 Characterization of the antibody conjugations

It is possible to determine the amount of DBCO moieties introduced into the antibodies after the reductive amination using UV-Vis spectroscopy. The concentration of the antibodies can be determined using the absorbance at 280 nm, while the DBCO has a distinctive absorption at 307 nm. The DBCO/antibody can then be calculated using Equation 5.3.[76]

$$\frac{c_{DBCO}}{c_{antibody}} = \frac{\frac{A_{DBCO}}{\epsilon_{DBCO}}}{\frac{A_{antibody}}{\epsilon_{antibody}}} \tag{5.3}$$

where c_{DBCO} and $c_{antibody}$ are the concentrations of DBCO and the antibody respectively, A_{DBCO} and $A_{antibody}$ the corresponding absorbances and ϵ_{DBCO} and $\epsilon_{antibody}$ the extinction coefficients. ϵ_{DBCO} and $\epsilon_{antibody}$ are assumed to be 12000 respectively 204000 L mol^{-1} cm^{-1}.[76] Anti-mouse@DBCO and anti-rabbit@DBCO secondary IgG antibodies prepared by the above described methods were characterized and the amount of DBCO/antibody were found to be 4.2 and 5.7 respectively. The corresponding spectra can be seen in Figure 5.24.
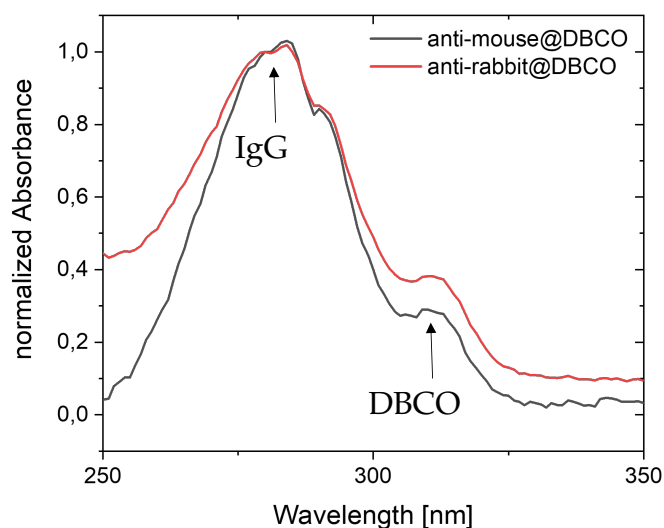
Figure 5.24: UV-Vis spectra of the antimouse@DBCO and antirabbit@DBCO secondary antibodies used for the subsequent conjugation to QDs. The absorption at 280 nm can be attributed to the antibody, IgG, whereas the absorption peak at 307 nm results from the DBCO. The amount of coupled DBCO/antibody was found to be slightly higher for the anti-rabbit IgG than for the anti-mouse IgG.

The antibodies were successfully conjugated to DBCO, making them suitable for the following bio-orthogonal azide click chemistry.

5.5.2 Characterization of QD binding sites

To study the amount of available binding sites on the QDs, these were conjugated to a commercially available Cy-5-DBCO conjugate. The number of Cy5/QD was evaluated using UV-Vis spectrometry, similar to the characterization of the DBCO/antibody. The absorbance spectra and calculated Cy5/QD of the such prepared QDs can be seen in Figure 5.25. Regardless of Cy5 excess, a very similar amount of 20.2 ± 2.1 Cy5/QD was bound to the QDs, suggesting this to be the available amount of binding sites per QD.
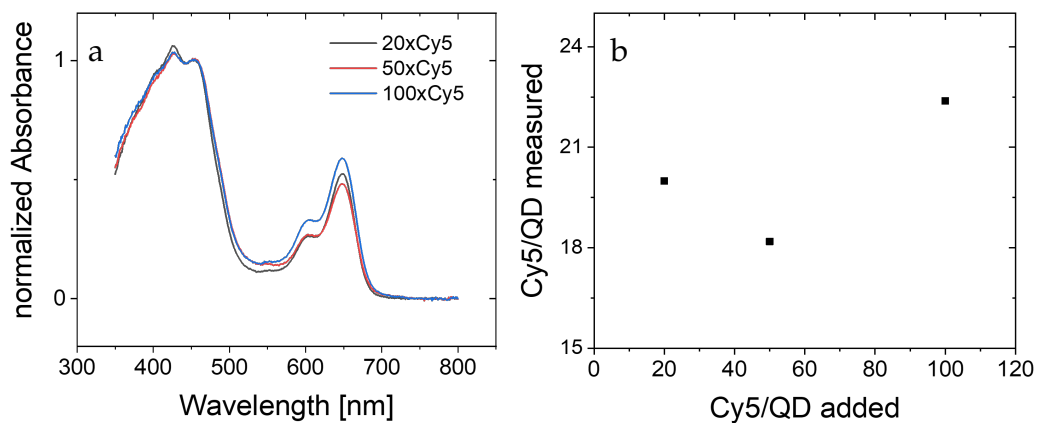
Figure 5.25: UV-Vis spectrum of QDs coupled to Cy5 (a) and calculated Cy5/QD (b). Different excesses of Cy5/QD were used during the azide coupling reaction. The UV-Vis spectra are normed to 450 nm (absorption of the QDs). Regardless of Cy5 excess, similar amounts of Cy5 were bound to the QDs, as clearly visible in (b).

5.5.3 Characterization of QD@antibodies

The number of antibodies conjugated per QD could be calculated using Equation 5.3 but using the absorbance at 450 nm for the QDs. To receive a useful absorbance for the conjugated antibodies, a baseline absorbance of QDs without antibodies was substracted from the QDs coupled with antibodies (QD@antibody) spectra, as shown in 5.26.
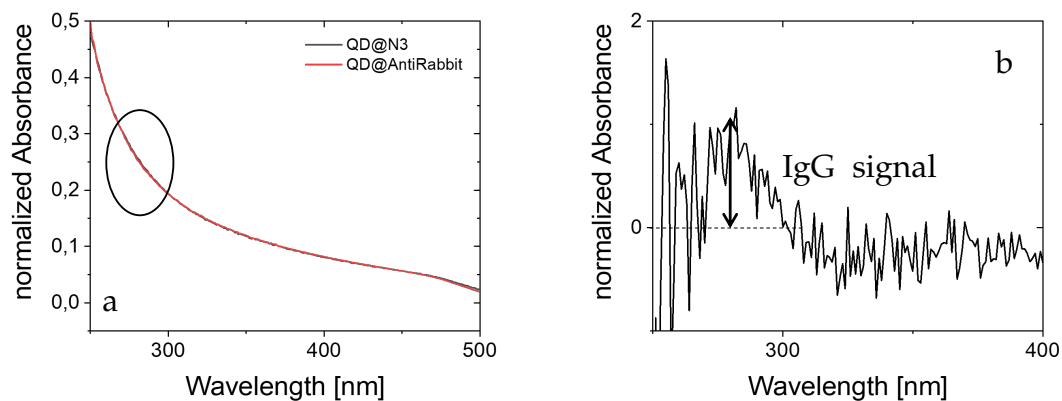
Figure 5.26: UV-Vis spectra of QDs before (@N3) and after (@AntiRabbit) coupling of antibodies (a) and substracted spectra (b). The region marked by the black ellipse is the region of interest for the antibody signal. This signal can be seen much better after substraction of the the two spectra, as depicted in (b). The QD@N3 spectrum was normed, to have the same absorbance at 450 nm as the QD@AntiRabbit sample.

For the azide coupled QD@antibodies, typically 5 - 7 antibodies could be coupled per QD, a yield of 20 - 30 % compared to the amount of antibody. The yields achieved by EDC/NHS were slightly lower with 1 - 3 antibodies/QD, approximately 3 - 10 % yield. It was not possible to perform this quantification for all samples, due to the small signal and a comparatively high amount of noise in the measurement as well as additional background caused by scattering. The latter indicates that the QD@antibody conjugates have a tendency to agglomerate with time. However, this was usually reversible by applying ultrasonification to the samples. An absorbance spectrum of a sample, where the quantification of AB/QD was not possible, is shown in the appendix (figure 8.2). A qualitative proof of successful AB conjugation to the QDs can be done using their hydrodynamic size. The QD@antibody conjugates will substantially increase in size, compared to the unconjugated samples. The hydrodynamic diameter of the samples before and after conjugation of antibodies can be seen in table 8.5 (appendix). A typical image of the z-average as determined by DLS can be seen in Figure 5.27.
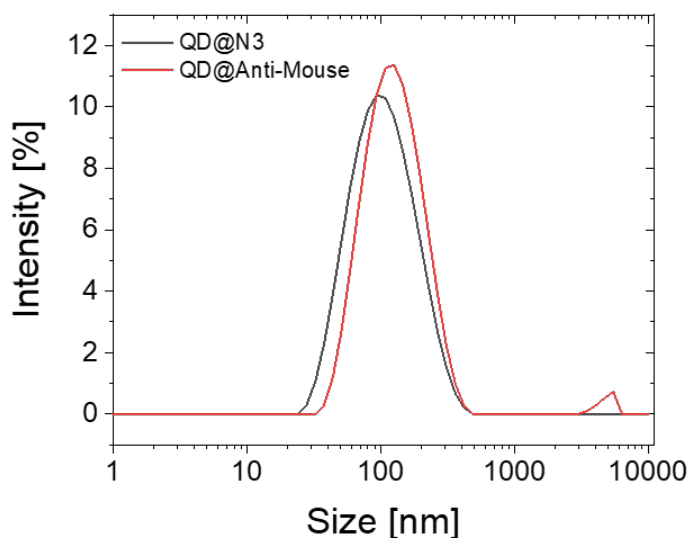
Figure 5.27: Z-Average of QD before coupling of antibody (QD@N3) and after coupling of an antibody (QD@Anti-Mouse). The size of the QD conjugates increases substantially with introduction of the antibody. The antibody functionalized QDs exhibit a slight tendency to aggregate. This was usually reversible by several minutes of ultrasonification.

The size of the conjugates generally increased by around 20 - 30 nm. This result is in good accordance with the size of an IgG antibody, which is roughly 18 nm in length.[77] This supports a successful coupling, even when the precise AB/QD amount could not be determined using UV-Vis spectroscopy.

5.6 Characterization of QD-cell interactions

5.6.1 QD toxicity

The toxicity of the QDs on the studied cell lines was determined using cell viability assays with 48 h QD exposure. QDs with a complete -OMe PB-b-PEO shell, with a shell prior to azide coupling (5 % N_3, 95 % -OMe (QD@N3)) and after coupling to IgG antibodies were tested. Similar surface functionalizations were used for the cell incubation experiments discussed below. The result of the assays can be seen in Figure 5.28.
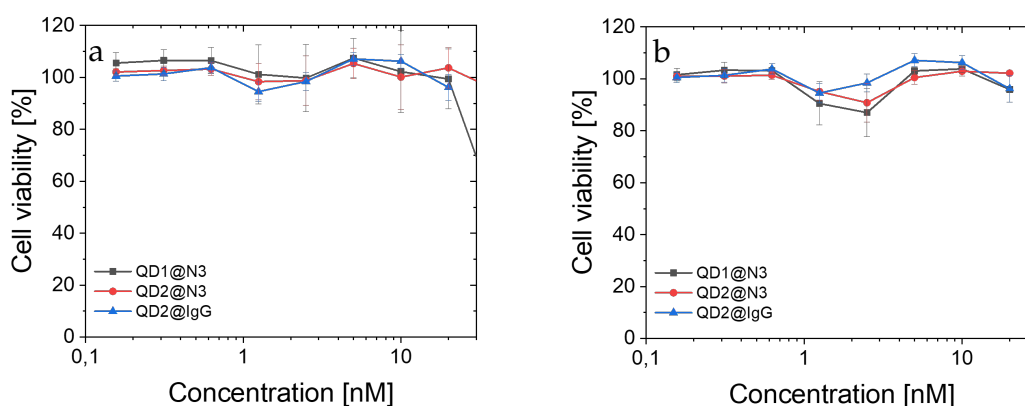

Figure 5.28: Results of the cell viability assays for HeLa cells (a) and MFC-7 cells (b) after 48 hours exposition. Regardless of functionalization, the cell viability for the MFC-7 cells is good for all tested concentrations. For HeLa cells, a significant loss of cell viability can be seen for QD concentrations greater than 10 nM.

For the MFC7 cells a good viability for all QD concentrations and functionalizations was observed. Contrary, for HeLa cells, a slight loss of cell viablity for 10 nM and a significant loss for 20 nM QD concentration was seen. They seem to be more vulnerable to cadmium leaching from the QDs. Nonetheless, since all of the exposure experiments performed during the thesis were typically conducted with lower QD concentration and less exposure time, a satisfactory cell viability for all experiments can be assumed. The cell viability was also tested against a cadmium salt, cadmium acetate. This allows for an estimation of how well the polymer ligand shell of the QDs improves the cell viability by preventing the release of Cd into the surrounding media. The corresponding Cd concentration of the QD was determined by using their size, shown in 8.4 in the appendix. For QD1, one QD equals approximately 9089 Cd atoms, whereas for QD2, one QD equals approximately 14125 Cd atoms.
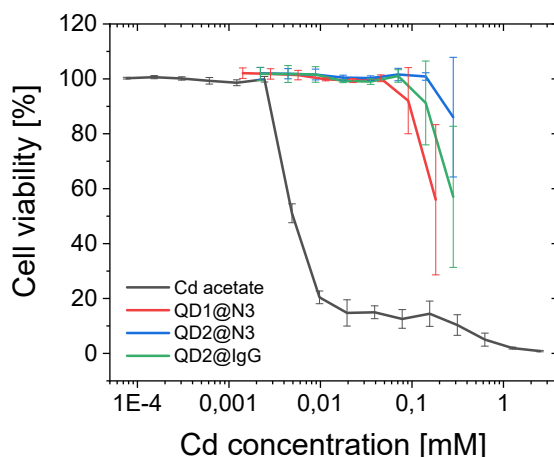
Figure 5.29: Cell viability of MFC-7 cells after 48 h exposure with cadmium acetate and QDs respectively. The viability is shown against the total Cd concentration. The encapsulation of the QDs with the PB-b-PEO ligand shell increases their cell viability compared to free Cd ions by more than one order of magnitude.

As can be clearly seen from Figure 5.29, the viability of the QDs compared to the free Cd ions of the Cd acetate is strongly increased. As expected, the PB-b-PEO ligand shell strongly decreases the toxicity of the QDs. This makes the QDs be useful and viable as fluorescence stains for biomedical purposes.

5.6.2 Unspecific cell uptake of QD

An important quality of all cell stains is a highly specific localisation, depending on the desired staining target. As such, an unspecific affinity to anything, that is not the aimed for target, is an undesired trait of such systems. The unspecific cell uptake of the QDs was studied by incubation with cells for up to 24 hours in cell medium. Due to the different coupling methods used for the later conjugation of proteins, three different surface compositions were tested. These were firstly, a completely passive shell with 100 % methoxy end groups (QD@OMe). Secondly, a shell including 5 % carboxylic end groups (QD@COOH) and thirdly a shell including 5 % azide end groups (QD@N3), with the rest being methoxy end groups. A low affinity of the QDs to the cells is expected, due to the PB-b-PEG shell. The cell uptake after the incubation was studied using confocal microscopy and at least 100 cells were used for quantified uptake. Typical images are shown in Figures 5.30, Figure 8.3 and Figure 8.4. The latter two can be found in the appendix. A quantified uptake can be seen in Figure 5.30 (b).
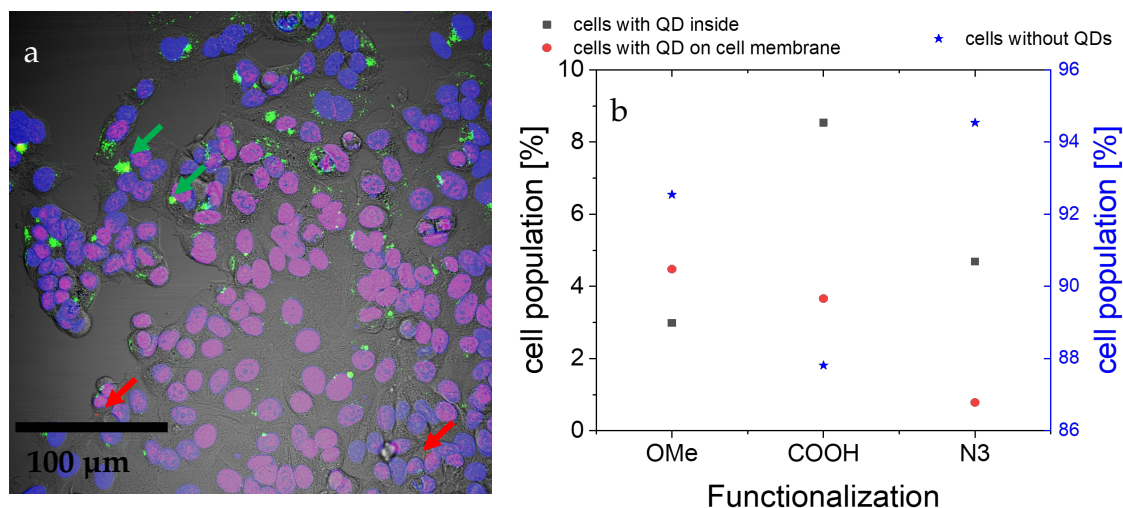
Figure 5.30: (a): Typical confocal image of MFC-7 cells exposed to 10 nM QDs (here: QD@N3) for 24 h. Nuclei are stained in blue (DAPI), lysosomes by FITC (green) and QDs are shown in red. Due to bleed through of the DAPI signal, the nuclei appear purple in colour. Mostly, no QD uptake can be seen. A very few QDs are being taken up by the cells and end up in the lysosomes, marked with green arrows. Another small population of QDs appears to be loosely bound to the cells, marked with red arrows. In rare cases, QDs can also be observed floating freely in the solution, even after multiple washing steps. This population will most likely arise from the loosely bound QDs separating from the cells after the washing steps. (b): Uptake of QDs by MFC-7 cells as determined using confocal microscopy. At least 70 cells were evaluated per QD batch. Percentage of cells without QD uptake are shown with blue stars and given by the right, blue y-axis. Percentage of cells with QDs inside or on the cell membrane is shown by the black squares and red spheres respectively and given by the left, black y-axis. Generally, the uptake of the QDs even after 24 hours exposure was low, in the region $<= 7$ %. Total uptake and cell adhesion for the QD@COOH was slightly higher with roughly 11 %.

As expected, only a small percentage of cells do show uptake of QDs, regardless of surface functionalization of the PB-PEO ligand shell. Most of the QDs, which are taken up into the cells, end up in the lysosomes by the process of endocytosis.[32, 58] A few of the QDs can be seen on the cell membranes, indicating that the endocytosis process is either unfavoured or slow. This is also supported by the free floating QDs, which can be seen even after the multiple washing steps during the preparation. These QDs most likely remained attached to the cell membranes during the washing steps but failed to be taken up fully into the cell. The cell uptake is slightly higher for the QD@COOH samples, than for the other two, as charges tend to increase cell uptake.[78]

5.7 Targeting of the cell membrane

5.7.1 QD@Anti-EpCAM & QD@WGA by EDC-NHS coupling

QDs conjugated via EDC-NHS coupling to WGA and anti-EpCAM (QD@WGA / QD@EpCAM) were prepared as described above and their ability to stain the cell membrane evaluated using confocal microscopy. QDs can only be used as fluorescence stains in biological applications, if a binding affinity to a specific target can be imparted upon them. For this purpose, QDs conjugated via EDC-NHS coupling to WGA and anti-EpCAM (QD@WGA / QD@EpCAM) were prepared as described above. Their ability to stain the cell membrane was evaluated using confocal microscopy. Both, the QD@EpCAM as well as the QD@WGA are expected to stain the cell membrane. In the case of the former, this is due to the specific interaction of the EpCAM receptor and the corresponding antibody. This receptor is abundantly found on the surface of MFC-7 cells. In the case of the QD@WGA, the affinity comes from the interaction of the WGA with any glycosylated membrane components.[79, 80] Typical microscopy images for cells stained by QD@WGA are presented in 5.31. A successful staining of the cell membrane can be seen.

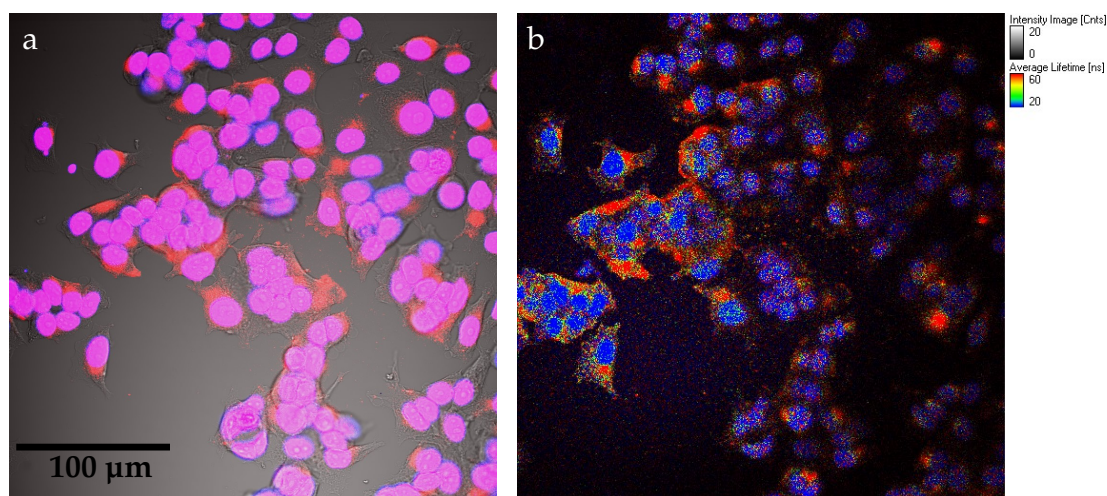The staining of MFC-7 cells by QD@Anti-EpCAM prepared by EDC-NHS coupling is shown in Figure 5.32.
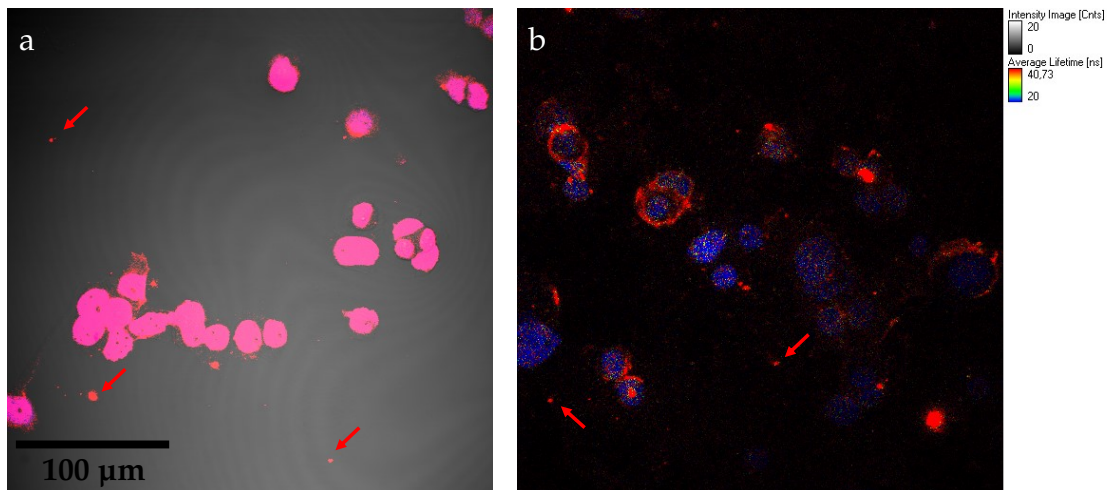
Figure 5.31: Staining of MFC-7 cells with QD@WGA (via EDC-NHS coupling).
(a) shows a typical confocal microscopy image. The transmissive
channel (gray) is overlaid with nucleus emission (blue, by DAPI)
and the QD emission (red). The nuclei are seen in purple, due to
bleed through of DAPI signal into the red channel. In (b) a typical
FLIM image can be seen, where short fluorescence lifetimes, e.g. by
the DAPI, are depicted in blue, and long fluorescence lifetimes are
coloured red. Clearly, the cells show a staining by the QD@WGA,
seen in both cases. Marked with red arrows, some free floating QDs
can be seen.
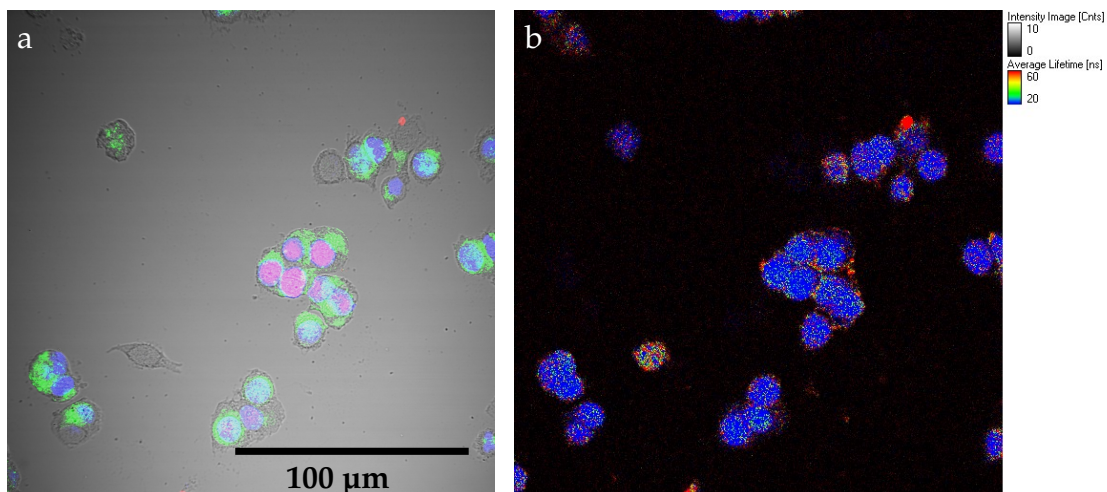
Figure 5.32: Staining of MFC-8 cells with QD@Anti-EpCAM (via EDC-NHS cou-
pling). Confocal microscopy image (a) and corresponding FLIM im-
age (b). Nuclei are stained with DAPI (blue). Lysosomes are stained
with FITC (green). The QD emission can be seen in red. Signal in-
tensity of the QDs was too low for an easy detection in the normal
confocal microsopy imaging. However, due to the longer imaging
time used for the FLIM measurement, the staining of the cells can be
seen in (b). The long lifetime of the QDs make it easy to distinguish
from the DAPI signal as well as autofluorescence.

Both coupling methods resulted in QDs, which show a clear staining of the cell membrane. The EDC-NHS coupling is therefore well suited for the modification of the above described QDs. The coupling of a relative unspecific protein as well as the highly specific binding of antibodies could be realized using this method. Additionally, as is evident from Figure 5.31 (b), the fluorescence lifetime of the resulting QD@protein conjugate is much longer than of the DAPI nucleus stain, resulting in an easy distinction of the two. This distinction between the two fluorophores can not be achieved using optical filters alone, as can be seen by the bleed-through of the DAPI signal into the QD channel.

5.7.2 QD@Anti-EpCAM & @WGA by azide click chemistry

Similar to the QD coupled with EDC-NHS coupling chemistry, EpCAM and WGA were also coupled using the azide click chemistry. This allows for a regio-selectivity in the binding site, contrary to the EDC-NHS coupling. This should result in a higher binding affinity of the QD@WGA and QD@Anti-EpCAM produced by this coupling strategy. The same cell staining experiments as for the EDC-NHS coupled were performed, with the results shown in Figures 5.33 and 5.34.

Figure 5.33: Staining of MFC-7 cells with QD@Anti-EpCAM (azide coupling). The left image shows a typical confocal microscopy image, the transmissive channel (gray) overlaid with the blue (emission by DAPI) and red fluorescent (emission by QDs) channels. The purple colour of the nuclei results from the bleed-through of DAPI emission into the red channel. The right image shows the corresponding FLIM measurements. Clearly, the signal of DAPI (short-lived, blue) and QDs (long-lived, red) can be easily distinguished in the FLIM images. The staining of the full membrane is also more easily apparent than on the left image.
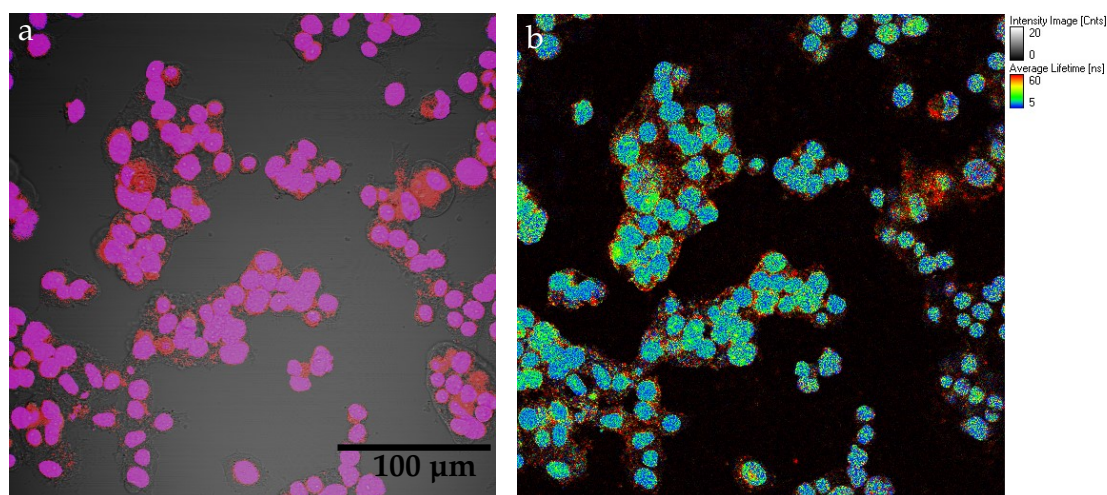
Figure 5.34: Staining of MFC-7 cells with QD@WGA (azide coupling). On the left, the confocal image can be seen, with the QDs shown in red. On the right, the corresponding fluorescence lifetime image is shown. Clearly an affinity of the QDs to the whole cell membrane can be seen. Note that bleed through of the signal of the DAPI dye into the red channel can be observed. It is used for staining the cell nucleus (blue) but due to the bleed through the nuclei appear purple. This aberration is less problematic in the FLIM image, where the DAPI can be seen as the short-lived (blue) signal.

Both QD@protein conjugates show a clear affinity to the membrane. The comparison of signal strength of different confocal images is slightly ambiguous, as small variations in e.g. microscopy slide height, volume of sample in the well or cell density can have a significant influence on measured intensity. Nonetheless, the higher signal intensity seen in Figures 5.33 and 5.34 compared to Figures 5.31 and 5.32 implies a higher remaining binding affinity by using the azide coupling. The results fit with the hypothesis described above, whereas the random orientation resulting from the EDC-NHS coupling as well as the the possible conjugation near the active site of the antibody will lead to a loss of binding affinity. This can be avoided by the regio-selective binding using the reductive amination of the glycolysated sites of the F_c region of the antibody, followed by azide coupling. Thus, an ordered orientation of the antibodies and a coupling reaction far away from the active site of the antibody is achieved and thus a high remaining binding affinity of the antibody results. The conjugation of proteins could be achieved by both coupling methods. As expected, the binding affinity seems to be higher for the samples prepared by azide coupling, than for the samples prepared by EDC-NHS coupling, showing the usefulness of applying a regio-selective conjugation method to QD-antibody conjugates.

5.8 Targeting of specific cell organelles by primary/secondary antibody approach

As targeting of the cell membrane has been realized, a further approach to target cell organelles within the cells was studied. Here, staining of fixed cells was studied, instead of live ones. This was done to avoid problems incurred by having to overcome the cell membrane.[81, 82, 83] After the fixation of the cells, the cell membrane can be permeabilized, allowing the QD@antibody conjugates to easily diffuse into the cell. The cell organelles in questions were marked by using primary antibodies, with the QDs coupled to the corresponding secondary antibody to result in a fluorescent stain, similar to many state of the art cell stains. The primary-secondary antibody approach is used to achieve a more specific staining and a higher signal intensity of the stain. It also allows for the staining of many different targets, by simply changing the primary antibody for one, with a different target. This makes it a very flexible way to stain targets.[84] Tubulin, a cytoskeleton protein[85, 86], and the EEA1 receptor, almost exclusively found on early endosomes[87, 88, 89], were chosen as staining targets. Binding affinity of the QDs conjugated with secondary antibodies was confirmed using dotblots. Due to a strong background signal on the nitrocellulose membranes used for the dotblots, the results were ambiguous. However, a drop of signal in the regions marked by non compatible antibodies (goat and mouse antibodies for anti-rabbit and goat and rabbit for anti-mouse) was observed, whereas no or only a slight increase of signal in the regions marked by the compatible antibodies was seen. The quality of the camera used for the images was insufficient, due to the strong background signal. Thus, the pictures taken of the dotblots, seen in figure 8.6 (appendix), do not resolve the aforementioned observations. Nonetheless, the reduction of signal strength in the non compatible regions and slight increase in the compatible region imply a specific binding affinity of the conjugated antibodies in accordance with the expectations. The figures 5.35 and 5.36 show the results of staining MFC-7 cells with QD@Anti-Rabbit and QD@Anti-Mouse after applying mouse anti-tubulin and rabbit anti-EEA1 primary antibodies respectively.
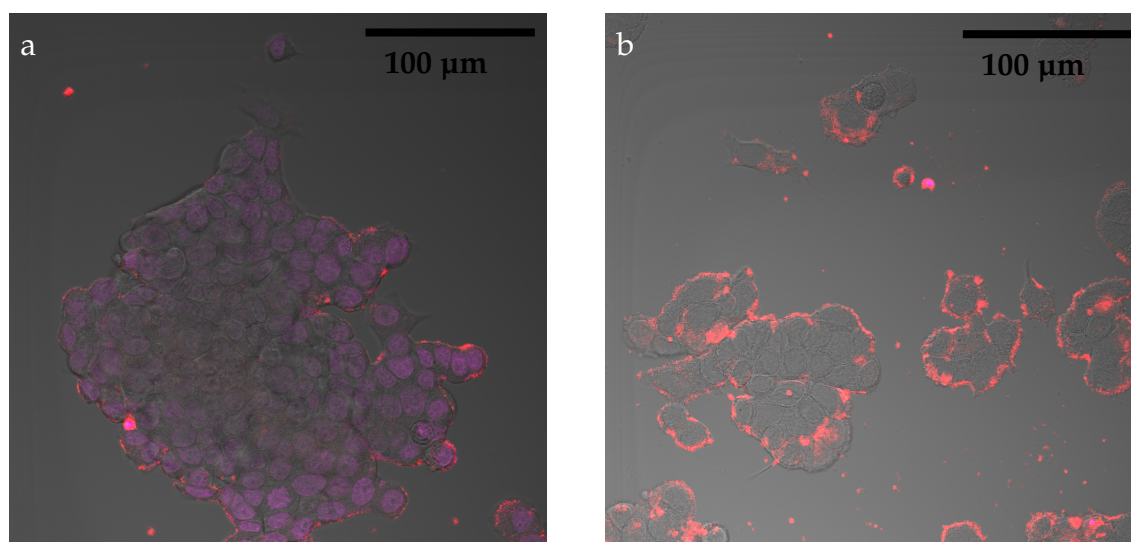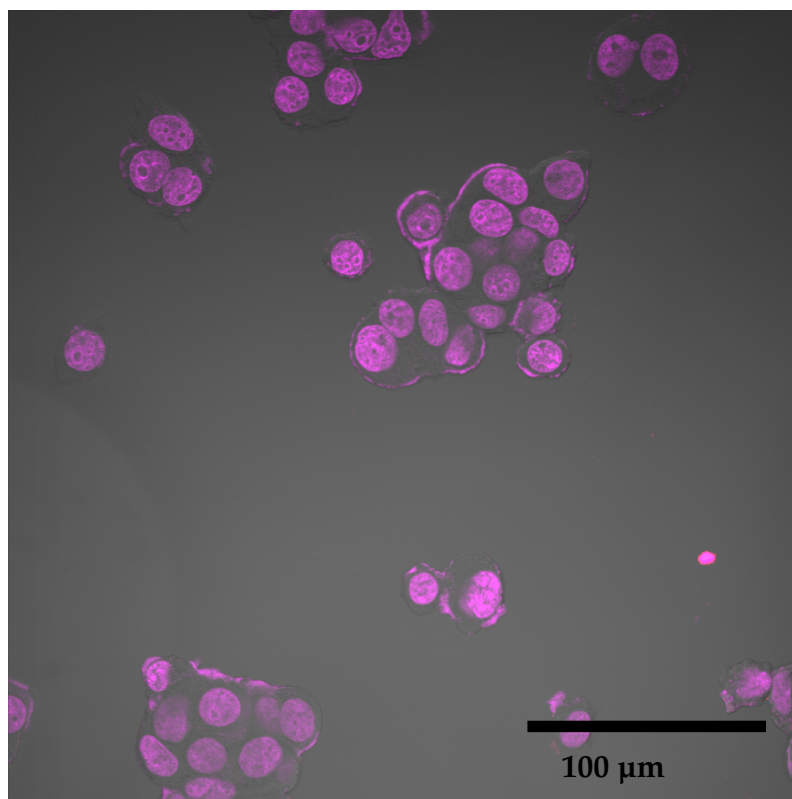
Figure 5.35: Typical confocal microscopy image of MFC-7 cells incubated with rabbit anti-EEA1 primary antibody followed by QD@Anti-Rabbit. Nuclei were stained with syto deep red, seen in purple. QD emission is depicted in red. The QDs prepared by azide coupling are shown in (a), whereas the QD prepared by EDC-NHS coupling are seen in (b). Clearly, both QD@Anti-Rabbit samples only showed an affinity for the cell membrane, but did not stain the early endosomes.

For the QD@Anti-Rabbit conjugates, two unexpected results were observed. Firstly, only the cell membrane could be stained with the QD@Anti-Rabbit, not the early endosomes. Secondly, contrary to prior results, the samples prepared by EDC-NHS coupling exhibit a stronger binding affinity to the cell membrane than the samples prepared by azide coupling. A stronger binding affinity of the azide coupled samples was expected, due to the higher number of antibodies per QD coupled via the azide coupling and the hypothesized higher binding affinity of the such prepared antibodies, as described above. It is unclear, why the contrary trend was observed. No unspecific binding of the QD@Anti-Rabbit was observed, as seen in Figure 8.7 (appendix). Therefore, the erroneous staining of the cell membrane can only arise due to binding of primary antibodies to the cell membrane.

The size of the QD@antibody conjugates is quite big, $\approx$ 80 - 100 nm, as described above. Therefore, they might not be able to diffuse into the cell, even if the cells have been permeabilized. However, parts of the outer ligand shell, including the antibodies, might be mobile enough to enter the cells. There they might be anchored by an early endosome, which diffused close enough to the cell membrane. This will lead to a staining of the cell membrane, as the fluorescent QD is unable to access the inner parts of the cell but bound via the ligand shell to

the early endosome.

Figure 5.36: Typical confocal microscopy image of MFC-7 cells incubated with mouse anti-tubulin primary antibody followed by QD@Anti-Mouse. The QDs were prepared by azide coupling. Nuclei were stained using syto deep red, visible in purple. No staining by QDs (red) could be observed.

A different result was obtained for the QD@Anti-Mouse samples. No staining of the cells was observed, regardless of coupling method. Again, this implies that the pores created in the cell membrane by the permeabilization were too small for the big QD@antibody conjugates to pass. The permeabilization has shown to be key process for the targeting of inner cell organelles. If the permeabilization is insufficient, as seen above, the correct target will not be stained by the QD@antibody conjugates. On the other hand, a too thorough permeabilization will destabilize the whole cell. Another approach to this problem would be the decrease of the PB-b-PEO ligand shell size. However, this will reduce the stability and bio-compatibility of the QDs significantly, which is why this approach was not pursued in this work.

5.9 Multiplexing with QDs in confocal microscopy

In the figures shown above, e.g. Figure 5.31, the good contrast of organic fluorophore and QD in FLIM was alreaedy clearly visible. Further experiments were performed, to ascertain mixtures of QDs. To this end, cells were sequentially incubated with four different batches of QDs. Figure 5.37 shows both, confocal microscopy image as well as FLIM of cells exposed to these mixtures of QDs.
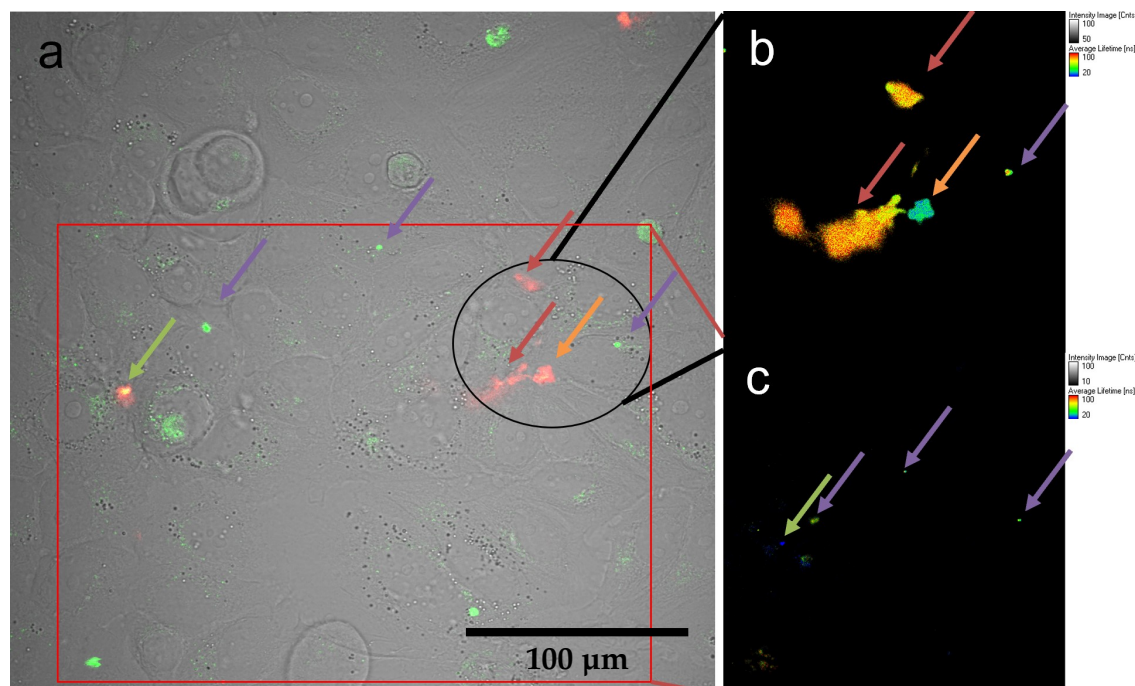
Figure 5.37: Confocal images of HeLa cells sequentially incubated with green and red fluorescent QDs. Each incubation lasted for 8 - 12 h, with a QD concentration of 10 nM. The order of incubation was short-lived red (orange arrows), long-lived red (red arrows), short-lived green (green arrows) and long-lived green QDs (purple arrows). The transmission image is shown in (a), the FLIM images of the black and red marked regions of interest (ROIs) are shown in respectively in (b) and (c). For (c), a 525 ± 50 nm optical bandpass filter was applied, to remove the colocalized signal of the red QDs at the leftmost green QD population.

As no specific binding motif was introduced into the QDs used for the experiments shown in 5.37, no particular staining of the cells was observed and a random distribution and position of the QDs was seen. Clearly, the QDs cannot be distinguished based on their emission colour alone. The emission spectra of the four QD batches are shown in Figure 8.5 (appendix). This is especially apparent in the ROI shown in 5.37 (b), as the lower two red QD appear to be the same QD batch. The distinction is easy utilizing the FLIM image, however. In case of over-

lapping emission in the same pixels, the above shown and discussed models can be used to further refine the knowledge about stained regions, allowing the use of QDs for complex multiplexing applications.

6 Conclusion

The use of GS-QDs as fluorescence lifetime based cell stains was investigated. It has beeen shown that up to trinary mixtures of QDs with similar emission colour can be used in conjunction as cell stains, allowing for a great improvement in number of analytes than can be simoultaneously used in fluorescence multiplexing applications such as confocal microscopy. For the analysis of these mixtures two different models were applied, linear fit of the mean lifetime and a superposition model. It was shown, that the latter allows for the extraction of mixture composition with a resolution of ≈ 2 % in case of binary and ≈ 5 % in case of trinary mixtures. On the other hand, the linear fit model has shown a resolution that is 2 - 6 times worse, while also not being applicable to more complex mixtures than binaries. Therefore, the superposition model was shown to be strictly superior in the analysis.

Furthermore, GS-QD were conjugated with various proteins to impart affinity for specific cell organelles. Two different conjugation methods were applied, azide click chemistry and EDC-NHS coupling. Both could be used for successful conjugation to the GS-QDs. The confocal microscopy images imply a stronger binding affinity for the GS-QDs prepared by azide coupling than for the EDC-NHS coupling. While staining of the two chosen intracellular organelles was not successful, the cell membrane could be stained by conjugation of both, WGA and anti-EpCAM IgG antibodies. Thus, the use of GS-QDs as useful fluorescence multiplexing agents in biomedical imaging applications has been shown theoretically and practically. They could improve the complexity of scientific questions that can be pursued using these applications and therefore push the boundaries of bioimaging a little bit further.

7 Safety

The table 7.1 lists all H- and P-statements of the used hazardous chemicals during this work.

Table 7.1: H- and P-statements of every used hazardous chemical. Safety information obtained from [90].

Chemical	GHS-Symbols	H-statement	P-statement	amount used
Acetone		225-319-336-EUH066	210-240-241-242-305+351+338	10 L
AIBN		242-302+332-412-EUH044	210-235-273-304+240+312-370+378-403	5 g
Cadmium acetate		301-312-330-340-350-372-410	202-260-273-280-302+352+312-304+340+310	50 g
Cadmium oxide		330-341-350-361fd-372-410	202-260-264-271-273-304+340+310	30 g
Chloroform		302-331-315-319-351-361d-336-372	261-281-305+351+338-311	500 mL
Ethanol		225-319	210-240-305+351+338-403+233	50 L
1-Ethyl-3-(3-dimethylamino-propyl)carbo-diimide		302-312+332-315-319-335	261-280-305-351-338	2 g

Hydrochloric acid (37%)		290-314-335	260-280-303+361+353-304+340+310-305+351+338	3 L
Isopropanol		225-319-336	210-233-240-241-242-305+351+338	20 L
Methanol		225-331-311-301-370	210-233-280-3102+352-304+340-308+310-403+235	5 L
n-Hexane		225-304-361f-373-315-336-411	210-240-273-301+310-331-302+352-403+235	15 L
Oleylamine		302-304-314-318-335-373-400-410	273-280-301+330+331-303+361+353-304+340+310-305+351+338	300 mL
Selenium (powder)		301+331-373-413	260-264-273-301+310-304+340+311-314	100 g
Toluene		225-304-315-336-361d-373-412	202-210-273-301+310-303+361+353-331	5 L
Tetrahydrofurane		225-302-319-335-351-EUH019	210-280-301+312+330-305+351+338-370+378-403+235	20 L
VA-044		317	280-261-272-363-302+352-333+313-501	1 g

8 Appendix

Table 8.1: Sample compositions of the triangle samples shown in figure 5.13

fraction short-lived QD [%]	fraction medium long-lived QD [%]	fraction long-lived QD [%]	mean lifetime [ns]
30	10	60	137
30	20	50	124
30	30	40	118
30	40	30	111
30	50	20	101

Table 8.2: Sample compositions of the sphere samples shown in figure 5.13

fraction short-lived QD [%]	fraction medium long-lived QD [%]	fraction long-lived QD [%]	mean lifetime [ns]
60	10	30	107
40	30	30	110
30	40	30	113
20	50	30	115

Table 8.3: Sample compositions of the rectangle samples shown in figure 5.13

fraction short-lived QD [%]	fraction medium long-lived QD [%]	fraction long-lived QD [%]	mean lifetime [ns]
30	40	30	113
25	50	25	111
20	60	20	107
15	70	15	105

Table 8.4: QD sizes and calculated corresponding Cd atom number per QD for
the samples used in 5.28 and 5.29

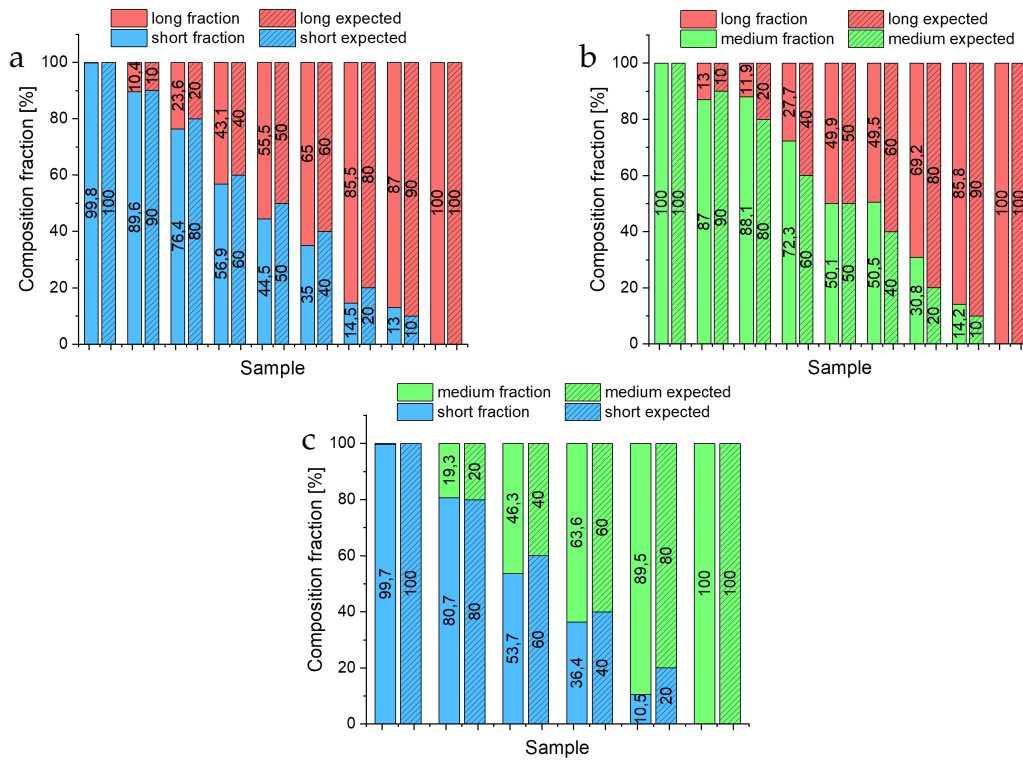| QD samples	diameter [nm]	Cd atoms/QD
QD 1	12	9089
QD 2	13.9	14125

Figure 8.1: Expected and calculated composition fractions of the samples shown
in 5.11 by applying a superposition model. Similar to the results ob-
tained by using a linear fit of the average lifetime, the results are in
very good agreement for the [s]+[l] mixture shown in (a). The calcu-
lated fractions for the [m]+[l] mixture (b) and the [s]+[m] (c) mixture
are both in good agreement as well, with the highest deviations be-
ing seen in the [m]+[l] mixture. In contrast, the linear model failed to
accurately describe the [s]+[m] mixture.

Table 8.5: Sizes of QDs before and after conjugation of antibodies.

Sample	Z-average [nm]	PDI
red1@N3	89.2	0.214
red2@N3	80.0	0.287
red1@anti-mouse (azide coupling)	114	0.224
red2@anti-rabbit (azide coupling)	245	0.320
red2@anti-rabbit (EDC-NHS coupling)	112	0.233
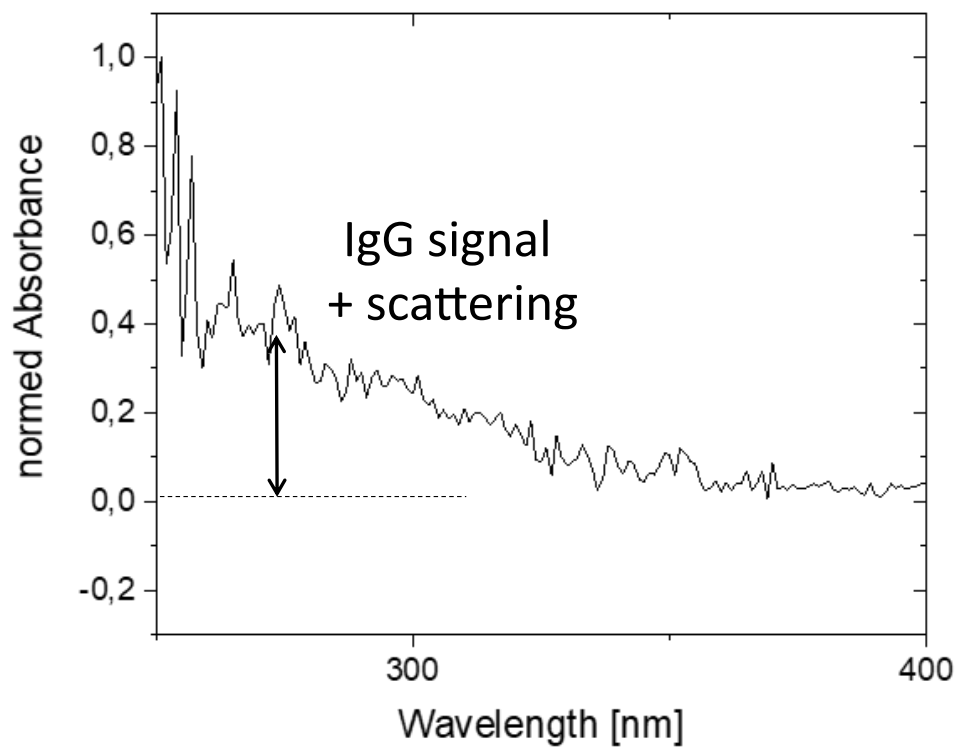
Figure 8.2: UV-Vis spectrum of an IgG signal, that could not be properly extracted due to the increased scattering background of the sample. This also indicates a small amount of aggregation of the QDs after AB conjugation.
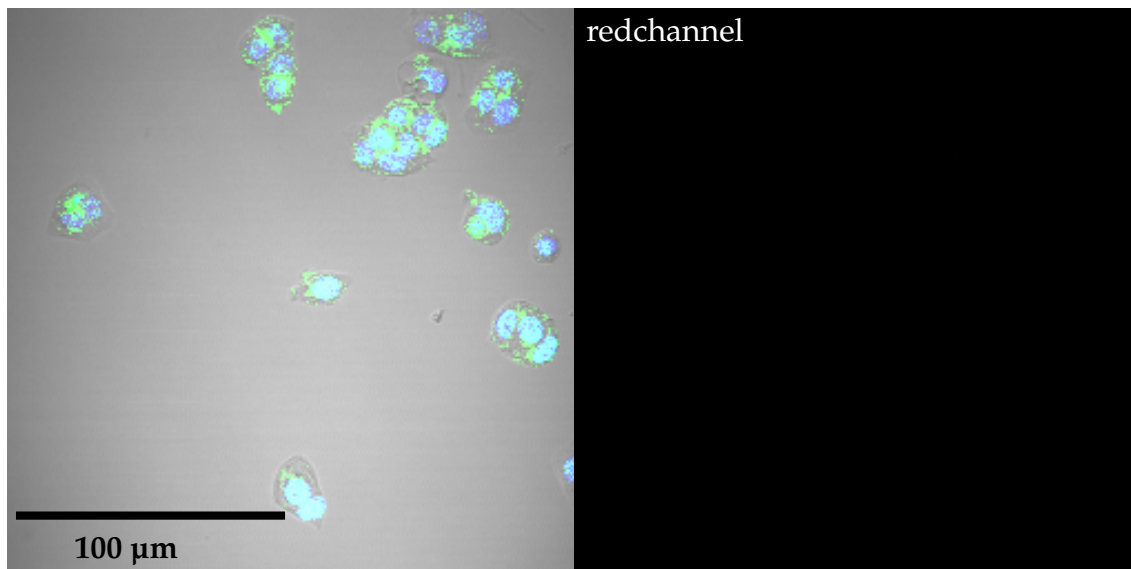
Figure 8.3: Typical image of MFC-7 cell uptake of QD@COOH after 24 hours. The nuclei have been stained with DAPI (blue), the lysosomes with FITC (green) and QDs are shown in red. The red channel is also shown on the right side. As can be seen, generally no or only a small amount of QD uptake was observed.
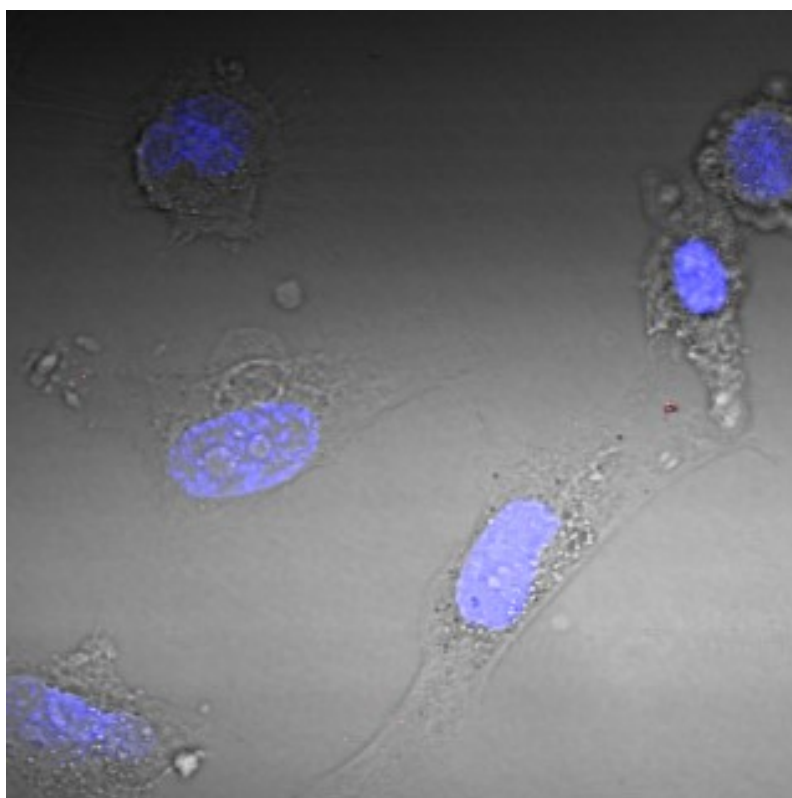
Figure 8.4: Typical image of MFC-7 cell uptake of QD@OMe after 24 hours. The nuclei have been stained with DAPI (blue) and QDs are shown in red. As can be seen, generally no or only a small amount of QD uptake was observed.
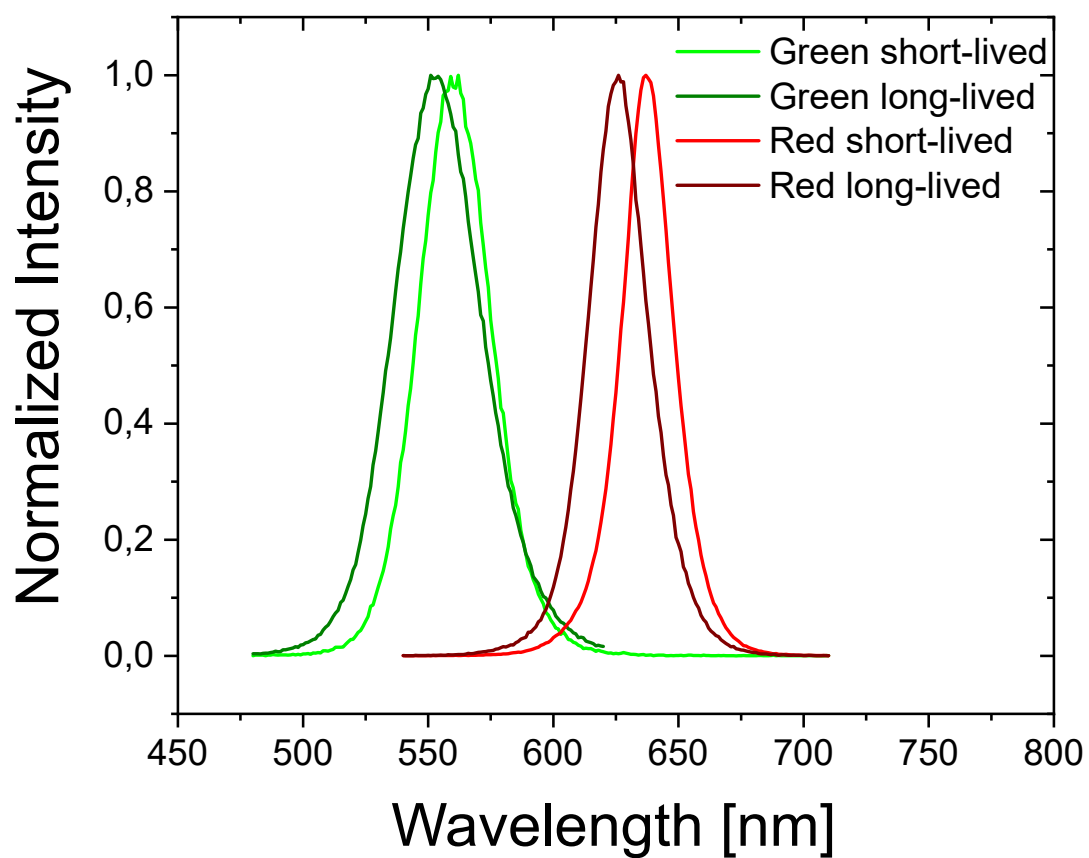
Figure 8.5: Emission spectra of the four QD batches used for figure 5.37. The emission spectra of the QDs are too similar to each other, to make a distinction within one colour easily feasible using the fluorescence emission alone.

Figure 8.6: Images of the dotblots performed to confirm the binding affinity of the QD conjugated with secondary antibodies. The regions marked with *m*, denote the primary mouse antibody, regions marked with *r*, those, where rabbit antibody was applied and regions marked with *I*, where the goat antibody was deposited. Membrane 1 was incubated with QD@anti-rabbit (azide coupling), membrane 2 with QD@anti-rabbit (EDC-NHS coupling) and membrane 3 was incubated with QD@anti-mouse (azide-coupling). Due to the strong background signal and the insufficient quality of the camera, the images do not show the observations described in the subsection "Targeting of specific cell organelles by primary/secondary antibody approach".

Figure 8.7: Typical confocal microscopy image of MFC-7 cells incubated with QD@Anti-Rabbit but without prior application of the primary antibody. No specific staining of the cells was observed, only the formation of a few small aggregates, which sedimented at random positions.
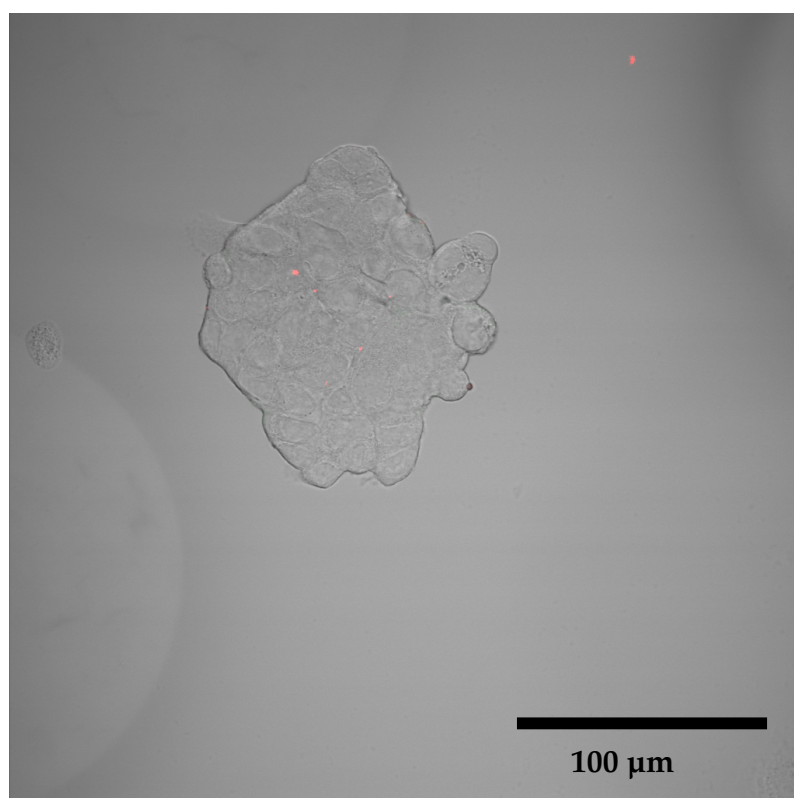
9 Acknowledgements

me to use a TEM and imaging a lot of samples for me.

Sonja and Öznur from the CAN for the synthesis of the GS-QDs as well as many helpful discussions about their properties. I hope, I wasn't too annoying.

My office colleagues, Julia, Sönke and Felix. Thanks for the good working atmosphere and making every day at work a treat. Naturally, also the other members of the Weller group, as well as the former members, such as Jana, Ahir, Lea, Elena, Nancy, Sophia, Rieke, Finn, Sebastian, Marius, Bendix, Lasse, Hauke, Marcus and many more. The place just wouldn't be the same without you.

My bachelor student Daniel. You did a good job and the data from your samples was highly useful.

Last but not least of course my family, my parents and sister, who always supported me in all of my endeavours and made my studies possible. And of course my wife, who kept me going through all the difficult times, patiently listened to all my complaints and helped me be a better person. Thank you, Merle!

References

[1] Michel Nasilowski, Benoit Mahler, Emmanuel Lhuillier, and Sandrine Ithurria. Two-Dimensional Colloidal Nanocrystals. *Chemical Reviews, American Chemical Society*, 18(116):10934/10982, 2016.

[2] R. Mastria and A. Rizzo. Mastering heterostructured colloidal nanocrystal properties for light-emitting diodes and solar cells. *Journal of Materials Chemistry C*, 4(27):6430–6446, 2016.

[3] Sandeep Kumar and Thomas Nann. Shape control of II-VI semiconductor nanomaterials. *Small*, 2(3):316–329, mar 2006.

[4] Victor K. LaMer and Robert H. Dinegar. Theory, Production and Mechanism of Formation of Monodispersed Hydrosols. *Journal of the American Chemical Society*, 72(11):4854, 1950.

[5] Howard Reiss. The growth of uniform colloidal dispersions. *The Journal of Chemical Physics*, 19(4):482–487, 1951.

[6] Jeffrey M. Pietryga, Young Shin Park, Jaehoon Lim, Andrew F. Fidler, Wan Ki Bae, Sergio Brovelli, and Victor I. Klimov. Spectroscopic and device aspects of nanocrystal quantum dots. *Chemical Reviews*, 116(18):10513–10622, 2016.

[7] Nguyen T.K. Thanh, N. Maclean, and S. Mahiddine. Mechanisms of nucleation and growth of nanoparticles in solution. *Chemical Reviews*, 114(15):7610–7630, 2014.

[8] Jianhai Zhou, Meiyi Zhu, Renyang Meng, Haiyan Qin, and Xiaogang Peng. Ideal CdSe/CdS Core/Shell Nanocrystals Enabled by Entropic Ligands and Their Core Size-, Shell Thickness-, and Ligand-Dependent Photoluminescence Properties. *Journal of the American Chemical Society*, 139(46):16556–16567, 2017.

[9] Luigi Carbone, Concetta Nobile, Milena De Giorgi, Fabio Della Sala, Giovanni Morello, Pierpaolo Pompa, Martin Hytch, Etienne Snoeck, Angela Fiore, Isabella R. Franchini, Monica Nadasan, Albert F. Silvestre, Letizia

Chiodo, Stefan Kudera, Roberto Cingolani, Roman Krahne, and Liberato Manna. Synthesis and micrometer-scale assembly of colloidal CdSe/CdS nanorods prepared by a seeded growth approach. *Nano Letters*, 7(10):2942–2950, oct 2007.

[10] Yusuf Kelestemur, Burak Guzelturk, Onur Erdem, Murat Olutas, Kivanc Gungor, and Hilmi Volkan Demir. Platelet-in-Box Colloidal Quantum Wells: CdSe/CdS@CdS Core/Crown@Shell Heteronanoplatelets. *Advanced Functional Materials*, 26(21):3570–3579, 2016.

[11] Andrea Castelli, Balaji Dhanabalan, Anatolii Polovitsyn, Vincenzo Caligiuri, Francesco Di Stasio, Alice Scarpellini, Rosaria Brescia, Milan Palei, Beatriz Martín-García, Mirko Prato, Liberato Manna, Iwan Moreels, Roman Krahne, and Milena P Arciniegas. Core/Shell CdSe/CdS Bone-Shaped Nanocrystals with a Thick and Anisotropic Shell as Optical Emitters. *Advanced Optical Materials*, 1901463:1–9, 2019.

[12] Luca De Trizio, Albert Figuerola, Liberato Manna, Alessandro Genovese, Chandramohan George, Rosaria Brescia, Zineb Saghi, Roberto Simonutti, Marijn Van Huis, and Andrea Falqui. Cu 3 P and Janus-like Cu À Cu 3 P Nanocrystals. *ACS nano*, 6(1):32–41, 2012.

[13] Grégory Guisbiers, Subarna Khanal, Francisco Ruiz-Zepeda, Jorge Roque De La Puente, and Miguel José-Yacaman. Cu-Ni nano-alloy: Mixed, core-shell or Janus nano-particle? *Nanoscale*, 6(24):14630–14635, 2014.

[14] Massimiliano Tomasulo, Ibrahim Yildiz, and M Raymo. pH-Sensitive Quantum Dots. *The Journal of Physical Chemistry B Letters*, 110:3853–3855, 2006.

[15] Melissa R. Dewi, Geoffry Laufersky, and Thomas Nann. A highly efficient ligand exchange reaction on gold nanoparticles: Preserving their size, shape and colloidal stability. *RSC Advances*, 4(64):34217–34220, 2014.

[16] Jun Zhang, Haibing Zhang, Weicheng Cao, Zhenfeng Pang, Jiongzhao Li, Yufei Shu, Chenqi Zhu, Xueqian Kong, Linjun Wang, and Xiaogang Peng. Identification of Facet-Dependent Coordination Structures of Carboxylate Ligands on CdSe Nanocrystals. *Journal of the American Chemical Society*, 141(39):15675–15683, 2019.

[17] Hui Min Gao, Hong Liu, Hu Jun Qian, Gui Sheng Jiao, and Zhong Yuan Lu. Multiscale simulations of ligand adsorption and exchange on gold nanoparticles. *Physical Chemistry Chemical Physics*, 20(3):1381–1394, 2018.

[18] M. L.H. Green. A new approach to the formal classification of covalent compounds of the elements. *Journal of Organometallic Chemistry*, 500(1-2):127–148, 1995.

[19] Nicholas Kirkwood, Julius O.V. Monchen, Ryan W. Crisp, Gianluca Grimaldi, Huub A.C. Bergstein, Indy Du Fossé, Ward Van Der Stam, Ivan Infante, and Arjan J. Houtepen. Finding and Fixing Traps in II-VI and III-V Colloidal Quantum Dots: The Importance of Z-Type Ligand Passivation. *Journal of the American Chemical Society*, 140(46):15712–15723, 2018.

[20] Luigi Carbone, Concetta Nobile, Milena De Giorgi, Fabio Della Sala, Giovanni Morello, Pierpaolo Pompa, Martin Hytch, Etienne Snoeck, Angela Fiore, Isabella R. Franchini, Monica Nadasan, Albert F. Silvestre, Letizia Chiodo, Stefan Kudera, Roberto Cingolani, Roman Krahne, and Liberato Manna. Synthesis and micrometer-scale assembly of colloidal CdSe/CdS nanorods prepared by a seeded growth approach. *Nano Letters*, 7(10):2942–2950, 2007.

[21] Jane Y. Rempel, Bernhardt L. Trout, Moungi G. Bawendi, and Klavs F. Jensen. Density functional theory study of ligand binding on CdSe (0001), (0001), and (1120) single crystal relaxed and reconstructed surfaces: Implications for nanocrystalline growth. *Journal of Physical Chemistry B*, 110(36):18007–18016, 2006.

[22] Jelena Dimitrijevic, Lisa Krapf, Christopher Wolter, Christian Schmidtke, Jan Philip Merkl, Tobias Jochum, Andreas Kornowski, Anna Schüth, Andreas Gebert, Gereon Hüttmann, Tobias Vossmeyer, and Horst Weller. CdSe/CdS-quantum rods: Fluorescent probes for in vivo two-photon laser scanning microscopy. *Nanoscale*, 6(17):10413–10422, 2014.

[23] Dmitri V. Talapin, Ivo Mekis, Stephan Götzinger, Andreas Kornowski, Oliver Benson, and Horst Weller. CdSe/CdS/ZnS and CdSe/ZnSe/ZnS core-shell-shell nanocrystals. *Journal of Physical Chemistry B*, 108(49):18826–18831, 2004.

[24] Anatolii Polovitsyn, Ali Hossain Khan, Ilaria Angeloni, Joel Q. Grim, Josep Planelles, Juan I. Climente, and Iwan Moreels. Synthesis of Anisotropic CdSe/CdS Dot-in-Giant-Rod Nanocrystals with Persistent Blue-Shifted Biexciton Emission. *ACS Photonics*, 5(11):4561–4568, 2018.

[25] Philip D. Howes, Rona Chandrawati, and Molly M. Stevens. Colloidal nanoparticles as advanced biological sensors. *Science*, 346(6205), oct 2014.

[26] Elmar Pöselt, Christian Schmidtke, Steffen Fischer, Kersten Peldschus, Johannes Salamon, Hauke Kloust, Huong Tran, Andrea Pietsch, Markus Heine, Gerhard Adam, Udo Schumacher, Christoph Wagener, Stephan Förster, and Horst Weller. Tailor-made quantum dot and iron oxide based contrast agents for in vitro and in vivo tumor imaging. *ACS Nano*, 6(4):3346–3355, 2012.

[27] Rahul P. Bagwe, Xiaojun Zhao, and Weihong Tan. Bioconjugated luminescent nanoparticles for biological applications. *Journal of Dispersion Science and Technology*, 24(3-4):453–464, may 2003.

[28] Ajay S. Karakoti, Soumen Das, Suntharampillai Thevuthasan, and Sudipta Seal. PEGylated inorganic nanoparticles. *Angewandte Chemie - International Edition*, 50(9):1980–1994, 2011.

[29] Eunkeu Oh, James B. Delehanty, Kim E. Sapsford, Kimihiro Susumu, Ramasis Goswami, Juan B. Blanco-Canosa, Philip E. Dawson, Jessica Granek, Megan Shoff, Qin Zhang, Peter L. Goering, Alan Huston, and Igor L. Medintz. Cellular uptake and fate of PEGylated gold nanoparticles is dependent on both cell-penetration peptides and particle size. *ACS Nano*, 5(8):6434–6448, 2011.

[30] Christian Schmidtke, Anna Marlena Kreuziger, Dirk Alpers, Anna Jacobsen, Yevgeniy Leshch, Robin Eggers, Hauke Kloust, Huong Tran, Johannes Ostermann, Theo Schotten, Joachim Thiem, Julian Thimm, and Horst Weller. Glycoconjugated amphiphilic polymers via click-chemistry for the encapsulation of quantum dots. *Langmuir*, 29(40):12593–12600, oct 2013.

[31] Hauke Kloust, Christian Schmidtke, Artur Feld, Theo Schotten, Robin Eggers, Ursula E.A. Fittschen, Florian Schulz, Elmar Pöselt, Johannes Ostermann, Neus G. Bastús, and Horst Weller. In situ functionalization and PEO coating of iron oxide nanocrystals using seeded emulsion polymerization. *Langmuir*, 29(15):4915–4921, apr 2013.

[32] Bryan Ronain Smith and Sanjiv Sam Gambhir. Nanomaterials for in Vivo Imaging. *Chemical Reviews*, 117(3):901–986, feb 2017.

[33] Horst Weller. Colloidal Semiconductor Q-Particles: Chemistry in the Transition Region Betweend Solid State and Molecules. *Angewandte Chemie - International Edition*, 32:41–53, 1993.

[34] Aurelio A. Rossinelli, Andreas Riedinger, Patricia Marqués-Gallego, Philippe N. Knüsel, Felipe V. Antolinez, and David J. Norris. High-temperature growth of thick-shell CdSe/CdS core/shell nanoplatelets. *Chemical Communications*, 53(71):9938–9941, 2017.

[35] Sushma Yadav, Ajeet Singh, and Sameer Sapra. Long-Lived Emission in Type-II CdS/ZnSe Core/Crown Nanoplatelet Heterostructures. *Journal of Physical Chemistry C*, 121(48):27241–27246, 2017.

[36] Kaifeng Wu, Qiuyang Li, Yongling Du, Zheyuan Chen, and Tianquan Lian. Ultrafast exciton quenching by energy and electron transfer in colloidal CdSe nanosheet-Pt heterostructures. *Chemical Science*, 6(2):1049–1054, 2015.

[37] Qiuyang Li and Tianquan Lian. Exciton dissociation dynamics and light-driven H2 generation in colloidal 2D cadmium chalcogenide nanoplatelet heterostructures. *Nano Research*, 11(6):3031–3049, 2018.

[38] Mikhail Y. Berezin and Samuel Achilefu. Fluorescence Lifetime Measurements and Biological Imaging. *Chemical Reviews*, 110(5):2641–2684, 2010.

[39] K David Wegner, Niko Hildebrandt, and Niko Hildebrandt. Quantum dots : bright and versatile in vitro and in vivo fluorescence imaging biosensors. *Chemical Society Reviews*, 44:4792–4834, 2015.

[40] Joseph R. Lakowicz. *Principles of Fluorescence Spectroscopy*, volume Third Edit. 2006.

[41] Ute Resch-Genger, Markus Grabolle, Sara Cavaliere-Jaricot, Roland Nitschke, and Thomas Nann. Quantum dots versus organic dyes as fluorescent labels. *Nature Methods*, 5(9):763–775, 2008.

[42] A. Cayuela, M. L. Soriano, C. Carrillo-Carrión, and M. Valcárcel. Semiconductor and carbon-based fluorescent nanodots: The need for consistency. *Chemical Communications*, 52(7):1311–1326, 2016.

[43] Benard Omogo, Feng Gao, Pooja Bajwa, Mizuho Kaneko, and Colin D. Heyes. Reducing Blinking in Small Core-Multishell Quantum Dots by Carefully Balancing Confinement Potential and Induced Lattice Strain: The "goldilocks" Effect. *ACS Nano*, 10(4):4072–4082, 2016.

[44] Yu Winston Wang, Nicholas P. Reder, Soyoung Kang, Adam K. Glaser, and Jonathan T.C. Liu. Multiplexed optical imaging of tumor-directed nanopar-

ticles: A review of imaging systems and approaches. *Nanotheranostics*, 1(4):369–388, 2017.

[45] Jian Liu, Stephen K. Lau, Vijay A. Varma, Richard A. Moffitt, Matthew Caldwell, Tao Liu, Andrew N. Young, John A. Petros, Adeboye O. Osunkoya, Tracey Krogstad, Brian Leyland-Jones, May D. Wang, and Shuming Nie. Molecular mapping of tumor heterogeneity on clinical tissue specimens with multiplexed quantum dots. *ACS Nano*, 4(5):2755–2765, 2010.

[46] Jian Liu, Stephen K. Lau, Vijay A. Varma, Brad A. Kairdolf, and Shuming Nie. Multiplexed Detection and Characterization of Rare Tumor Cells in Hodgkin's Lymphoma with Multicolor Quantum Dots. *Analytical Chemistry*, 82(14):6237–6243, 2010.

[47] Ellen R. Goldman, Aaron R. Clapp, George P. Anderson, H. Tetsuo Uyeda, J. Matthew Mauro, Igor L. Medintz, and Hedi Mattoussi. Multiplexed Toxin Analysis Using Four Colors of Quantum Dot Fluororeagents. *Analytical Chemistry*, 76(3):684–688, 2004.

[48] Azhar Zahoor Abbasi, Faheem Amin, Tobias Niebling, Sebastian Friede, Markus Ochs, Susana Carregal-Romero, Jose Maria Montenegro, Pilar Rivera Gil, Wolfram Heimbrodt, and Wolfgang J. Parak. How colloidal nanoparticles could facilitate multiplexed measurements of different analytes with analyte-sensitive organic fluorophores. *ACS Nano*, 5(1):21–25, 2011.

[49] Eric Lubeck and Long Cai. Single-cell systems biology by super-resolution imaging and combinatorial labeling. *Nature Methods*, 9(7):743–748, 2012.

[50] Jun Zhang, Xin Li, Sheng Li, Jun Cheng Zhang, Xu Yan, Gui Feng Yu, Da Peng Yang, and Yun Ze Long. Ultrasensitive Fluorescence Lifetime Tuning in Patterned Polymer Composite Nanofibers with Plasmonic Nanostructures for Multiplexing. *Macromolecular Rapid Communications*, 40(5):1–5, 2019.

[51] Eleonora Petryayeva, W. Russ Algar, and Igor L. Medintz. Quantum dots in bioanalysis: A review of applications across various platforms for fluorescence spectroscopy and imaging. *Applied Spectroscopy*, 67(3):215–252, 2013.

[52] Katrin Hoffmann, Thomas Behnke, Daniela Drescher, Janina Kneipp, and Ute Resch-Genger. Near-infrared-emitting nanoparticles for lifetime-based

multiplexed analysis and imaging of living cells. *ACS Nano*, 7(8):6674–6684, 2013.

[53] Katrin Hoffmann, Thomas Behnke, Markus Grabolle, and Ute Resch-Genger. Nanoparticle-encapsulated vis- and NIR-emissive fluorophores with different fluorescence decay kinetics for lifetime multiplexing Multiplex Platforms in Diagnostics and Bioanalytics. *Analytical and Bioanalytical Chemistry*, 406(14):3315–3322, 2014.

[54] William L. Rice and Anand T. N. Kumar. Preclinical whole body time domain fluorescence lifetime multiplexing of fluorescent proteins. *Journal of Biomedical Optics*, 19(4):046005, 2014.

[55] Teng Luo, Ting Zhou, and Junle Qu. Lifetime Division Multiplexing by Multilevel Encryption Algorithm. *ACS Nano*, 15(4):6257–6265, 2021.

[56] Andrew M. Smith, Hongwei Duan, Aaron M. Mohs, and Shuming Nie. Bioconjugated quantum dots for in vivo molecular and cellular imaging. *Advanced Drug Delivery Reviews*, 60(11):1226–1240, aug 2008.

[57] Yun Xing, Qaiser Chaudry, Christopher Shen, Koon Yin Kong, Haiyen E. Zhau, Leland W. Chung, John A. Petros, Ruth M. O'Regan, Maksym V. Yezhelyev, Jonathan W. Simons, May D. Wang, and Shuming Nie. Bioconjugated quantum dots for multiplexed and quantitative immunohistochemistry. *Nature Protocols*, 2(5):1152–1165, 2007.

[58] James B. Delehanty, Christopher E. Bradburne, Kimihiro Susumu, Kelly Boeneman, Bing C. Mei, Dorothy Farrell, Juan B. Blanco-Canosa, Philip E. Dawson, Hedi Mattoussi, and Igor L. Medintz. Spatiotemporal multicolor labeling of individual cells using peptide-functionalized quantum dots and mixed delivery techniques. *Journal of the American Chemical Society*, 133(27):10482–10489, 2011.

[59] Melissa Massey and W. Russ Algar. Nanoparticle Bioconjugates: Materials that Benefit from Chemoselective and Bioorthogonal Ligation Chemistries. *Chemoselective and Bioorthogonal Ligation Reactions*, pages 543–629, 2017.

[60] Philip D. Howes, Rona Chandrawati, and Molly M. Stevens. Colloidal nanoparticles as advanced biological sensors. *Science*, 346(6205), 2014.

[61] Cuie Wang, Qin Yan, Hong Bo Liu, Xiao Hui Zhou, and Shou Jun Xiao. Different EDC/NHS activation mechanisms between PAA and PMAA brushes and the following amidation reactions. *Langmuir*, 27(19):12058–12068, 2011.

[62] Sinyoung Jeong, Ji Yong Park, Myeong Geun Cha, Hyejin Chang, Yong il Kim, Hyung Mo Kim, Bong Hyun Jun, Dong Soo Lee, Yoon Sik Lee, Jae Min Jeong, Yun Sang Lee, and Dae Hong Jeong. Highly robust and optimized conjugation of antibodies to nanoparticles using quantitatively validated protocols. *Nanoscale*, 9(7):2548–2555, 2017.

[63] Christine Schieber, Alessandra Bestetti, Jet Phey Lim, Anneke D. Ryan, Tich Lam Nguyen, Robert Eldridge, Anthony R. White, Paul A. Gleeson, Paul S. Donnelly, Spencer J. Williams, and Paul Mulvaney. Conjugation of transferrin to azide-modified cdse/zns core-shell quantum dots using cyclooctyne click chemistry. *Angewandte Chemie - International Edition*, 51(42):10523–10527, 2012.

[64] Chelsea G Gordon and Carolyn R Bertozzi. *In Vivo Applications of Bioorthogonal Chemistries*. Wiley-VCH Verlag GmbH, 2017.

[65] Greg T. Hermanson. Antibody Modification and Conjugation. In *Bioconjugate Techniques*, pages 867–920. 2013.

[66] Yongfen Chen, Javier Vela, Han Htoon, Joanna L Casson, Donald J Werder, David A Bussian, Victor I Klimov, and Jennifer A Hollingsworth. " Giant " Multishell CdSe Nanocrystal Quantum Dots with Suppressed Blinking. pages 5026–5027, 2008.

[67] Dennis Steinigeweg, Max Schütz, Mohammad Salehi, and Sebastian Schlücker. Fast and cost-effective purification of gold nanoparticles in the 20-250 nm size range by continuous density gradient centrifugation. *Small*, 7(17):2443–2448, 2011.

[68] Matthew Newville and et al. Lmfit: Non-linear least-square minimization and curve-fitting for python., 2014. doi:10.5281/zenodo.11813.

[69] Jennifer A. Hollingsworth. Heterostructuring nanocrystal quantum dots toward intentional suppression of blinking and auger recombination. *Chemistry of Materials*, 25(8):1318–1331, 2013.

[70] Benoit Mahler, Piernicola Spinicelli, Stéphanie Buil, Xavier Quelin, Jean Pierre Hermier, and Benoit Dubertret. Towards non-blinking colloidal quantum dots. *Nature Materials*, 7(8):659–664, 2008.

[71] Olivier Labeau, Philippe Tamarat, and Brahim Lounis. Temperature Dependence of the Luminescence Lifetime of Single CdSe/ZnS Quantum Dots . *Physical Review Letters*, 90(25):25–28, 2003.

[72] Wennuan Nan, Yuan Niu, Haiyan Qin, Fan Cui, Yu Yang, Runchen Lai, Wanzhen Lin, and Xiaogang Peng. Crystal structure control of zinc-blende CdSe/CdS core/shell nanocrystals: Synthesis and structure-dependent optical properties. *Journal of the American Chemical Society*, 134(48):19685–19693, 2012.

[73] Luo Gu, David J. Hall, Zhengtao Qin, Emily Anglin, Jinmyoung Joo, David J. Mooney, Stephen B. Howell, and Michael J. Sailor. In vivo time-gated fluorescence imaging with biodegradable luminescent porous silicon nanoparticles. *Nature Communications*, 4:1–7, 2013.

[74] Hongxin Zhang, Yong Fan, Peng Pei, Caixia Sun, Lingfei Lu, and Fan Zhang. Tm3+-Sensitized NIR-II Fluorescent Nanocrystals for In Vivo Information Storage and Decoding. *Angewandte Chemie - International Edition*, 58(30):10153–10157, 2019.

[75] Roman V. Evstigneev, Peter S. Parfenov, Aliaksei Dubavik, Sergei A. Cherevkov, Anatoly V. Fedorov, Irina V. Martynenko, Ute Resch-Genger, Elena V. Ushakova, and Alexander V. Baranov. Time-resolved FRET in AgInS 2 /ZnS-CdSe/ZnS quantum dot systems. *Nanotechnology*, 30(19), 2019.

[76] Nalinikanth Kotagiri, Zhenyu Li, Xiaoxiao Xu, Suman Mondal, Arye Nehorai, and Samuel Achilefu. Antibody quantum dot conjugates developed via copper-free click chemistry for rapid analysis of biological samples using a microfluidic microsphere array system. *Bioconjugate Chemistry*, 25(7):1272–1281, 2014.

[77] Yih Horng Tan, Maozi Liu, Birte Nolting, Joan G Go, Jacquelyn Gervay-hague, and Gang-yu Liu. A Nanoengineering Approach for Immobilization. *ACS Nano*, 2(11):2374–2384, 2008.

[78] Azzah M. Bannunah, Driton Vllasaliu, Jennie Lord, and Snjezana Stolnik. Mechanisms of nanoparticle internalization and transport across an intestinal epithelial cell model: Effect of size and surface charge. *Molecular Pharmaceutics*, 11(12):4363–4373, 2014.

[79] Julien Nicolas, Simona Mura, Davide Brambilla, Nicolas Mackiewicz, and Patrick Couvreur. Design, functionalization strategies and biomedical applications of targeted biodegradable/biocompatible polymer-based nanocarriers for drug delivery. *Chemical Society Reviews*, 42(3):1147–1235, 2013.

[80] Sheng-Ce Tao, Yu Li, Jiangbing Zhou, Jiang Qian, Ronald L Schnaar, Ying Zhang, Irwin J Goldstein, Heng Zhu, and Jonathan P Schneck. Lectin microarrays identify cell-specific and functionally significant cell surface glycan markers. *Glycobiology*, 18(10):761–769, 2008.

[81] Anshika Kapur, Scott H. Medina, Wentao Wang, Goutam Palui, Xin Ji, Joel P. Schneider, and Hedi Mattoussi. Enhanced Uptake of Luminescent Quantum Dots by Live Cells Mediated by a Membrane-Active Peptide. *ACS Omega*, 3(12):17164–17172, 2018.

[82] Hongwei Duan and Shuming Nie. Cell-penetrating quantum dots based on multivalent and endosome-disrupting surface coatings. *Journal of the American Chemical Society*, 129(11):3333–3336, mar 2007.

[83] Kalyani Desale, Kaushik Kuche, and Sanyog Jain. Cell-penetrating peptides (CPPs): An overview of applications for improving the potential of nanotherapeutics. *Biomaterials Science*, 9(4):1153–1188, 2021.

[84] ThermoFisher Scientific. Introduction to Secondary Antibodies. https://www.thermofisher.com/de/de/home/life-science/antibodies/antibodies-learning-center/antibodies-resource-library/antibody-methods/introduction-secondary-antibodies.html, accessed 15. August 2023.

[85] Soumyananda Chakraborti, Kathiresan Natarajan, Julian Curiel, Carsten Janke, and Judy Liu. The emerging role of the tubulin code: From the tubulin molecule to neuronal function and disease. *Cytoskeleton*, 73(10):521–550, 2016.

[86] Abesh Bera and Mohan L. Gupta. Microtubules in Microorganisms: How Tubulin Isotypes Contribute to Diverse Cytoskeletal Functions. *Frontiers in Cell and Developmental Biology*, 10(July):1–16, 2022.

[87] F. T. Mu, J. M. Callaghan, O. Steele-Mortimer, H. Stenmark, R. G. Parton, P. L. Campbell, J. McCluskey, J. P. Yeo, E. P.C. Tock, and B. H. Toh. EEA1, an early endosome-associated protein. EEA1 is a conserved α- helical peripheral membrane protein flanked by cysteine 'fingers' and contains a calmodulin-binding IQ motif. *Journal of Biological Chemistry*, 270(22):13503–13511, 1995.

[88] J. M. Wilson, M. De Hoop, N. Zorzi, B. H. Toh, C. G. Dotti, and R. G. Parton. EEA1, a tethering protein of the early sorting endosome, shows a polarized

distribution in hippocampal neurons, epithelial cells, and fibroblasts. *Molecular Biology of the Cell*, 11(8):2657–2671, 2000.

[89] Sreeja C. Sekhar, Tomonari Kasai, Ayano Satoh, Tsukasa Shigehiro, Akifumi Mizutani, Hiroshi Murakami, Bishoy Ya El-Aarag, David S. Salomon, Anna Massaguer, Rafael de Llorens, and Masaharu Seno. Identification Of Caveolin-1 As A Potential Causative Factor In The Generation Of Trastuzumab Resistance In Breast Cancer Cells. *Journal of Cancer*, 4(5):391–401, 2013.

[90] Sigma Aldrich. Safety data sheets. https://www.sigmaaldrich.com, accessed 15. August 2023.

Eidesstattliche Versicherung

Hiermit versichere ich an Eides statt, die vorliegende Dissertation selbst verfasst und keine anderen als die ange- gebenen Hilfsmittel benutzt zu haben. Die eingereichte schriftliche Fassung entspricht der auf dem elektronischen Speichermedium. Ich versichere, dass diese Dissertation nicht in einem früheren Promotionsverfahren eingereicht wurde.

Hamburg, den _____   Unterschrift: _____